

INAUGURAL - DISSERTATION
zur
Erlangung der Doktorwürde
der
Naturwissenschaftlich - Mathematischen
Gesamtfakultät
der Ruprecht - Karls - Universität
Heidelberg

vorgelegt von
M. Sc. Ina Alber
aus Bonn-Duisdorf

Tag der mündlichen Prüfung: 14. November 2012

**Synthesis
and Plasmonic Properties
of Metallic
Nanowires and Nanowire Dimers**

Gutachter:

Prof. Dr. Reinhard Neumann

Prof. Dr. Annemarie Pucci

Zusammenfassung

In durch Aufätzung von Schwerionenspuren erzeugten Nanokanälen in Polymermembranen wurden zylindrische, metallische Nanodrähte elektrochemisch abgeschieden. Diese Nanodrähte bestanden aus Gold oder Gold-Silber-Legierungen, wobei das Elementverhältnis variiert wurde. Außerdem wurden durch gepulste Abscheidung segmentierte Nanodrähte hergestellt, wobei ein silberreiches Segment zwei Segmente mit großem Goldgehalt trennt. Die Länge eines Pulse kontrolliert die Segmentlänge. Durch anschließendes chemisches Auflösen der silberreichen Segmente entstanden Nanodrähte getrennt durch eine Lücke von bis zu 5 nm, sogenannte Nanodrahtdimere. Unvollständiges Auflösen der silberreichen Segmente führte zu Dimeren zusammengeslossen durch eine leitende Verbindung. Bei Anregung von Oberflächenplasmonen treten bei Dimeren mit Lücken kleiner 20 nm sehr hohe Feldverstärkungen in der Lücke auf. Die Plasmonenresonanzen der Nanostrukturen wurden in einem Transmissions-Elektronen-Mikroskop mittels Elektronen-Energieverlust-Spektroskopie analysiert. Diese Methode erlaubt es, gleichzeitig sowohl die Morphologie der Nanostrukturen zu untersuchen als auch die Plasmonenresonanzen zu messen. Die Analyse von Einzeldrähten und kapazitiv und leitend gekoppelten Dimeren zeigte, dass zahlreiche Parameter, wie Länge und Durchmesser, Größe der Lücke, sowie Zusammensetzung und Morphologie des Drahtes die Resonanzenergien empfindlich beeinflussen. Detaillierte Kenntnis der plasmonischen Eigenschaften ist wichtig für zukünftige Anwendung der Nanostrukturen als Substrate für Oberflächen-verstärkte Infrarot- und Raman-Spektroskopie.

Abstract

Cylindrical, metallic nanowires were electrochemically grown in nanochannels created in polymer membranes by etching of ion tracks. These nanowires consisted of Au or AuAg alloy with varying element ratio. In addition, segmented Au-rich/Ag-rich/Au-rich nanowires were synthesized by applying pulsed deposition. The duration of the pulses controls the length of the segments. By subsequent chemical dissolution nanowires separated by nanogaps with dimensions as small as 5 nm were also created, so-called nanowire dimers. Incomplete dissolution of the gap resulted in dimers connected by a conductive junction. Upon the excitation of surface plasmons in dimers separated by nanogaps smaller than 20 nm, high field enhancement is generated in the nanogap. We analysed the plasmonic properties of the synthesized structures by electron energy loss spectroscopy in a transmission electron microscope. This method enables the simultaneous investigation of the nanostructure morphology and the surface plasmon resonance energies. The analysis of single nanowires, and capacitively and conductively coupled nanowire dimers revealed that the resonance energies depend sensitively on many parameters, as length, diameter, gap size, as well as composition and morphology. Precise knowledge of the plasmonic properties of the synthesized structures are important for the future applications as substrates for surface enhanced infrared and Raman spectroscopy.

The thesis is based on the following publications.

I. Alber, W. Sigle, S. Müller, R. Neumann, O. Picht, M. Rauber, P. A. van Aken, and M. E. Toimil-Molares, "Visualization of Multipolar Longitudinal and Transversal Surface Plasmon Modes in Nanowire Dimers", ACS Nano 2011, 5 (12), 9845–9853.

<http://dx.doi.org/10.1021/nm2035044>

The article is reproduced in this thesis in part with permission. Copyright [2011] American Chemical Society.

I. Alber, W. Sigle, F. Demming-Janssen, R. Neumann, C. Trautmann, P. A. van Aken, and M. E. Toimil-Molares, "Multipole Surface Plasmon Resonances in Conductively Coupled Metal Nanowire Dimers", submitted to ACS Nano.

The article is reproduced in this thesis in part with permission. Copyright [2012] American Chemical Society.

I. Alber, S. Müller, M. Rauber, O. Picht, C. Trautmann, R. Neumann and M. E. Toimil-Molares

"Synthesis of segmented AuAg nanowires and nanogaps"

in preparation

Further publications

- I. Alber, J. Krieg, C. Müller, M. E. Toimil-Molares, C. Trautmann, P. Serbun, A. Navitski, G. Müller, "Freestanding copper nanocones for field emission by ion-track technology and electrodeposition", Techn. Digest of the 24th Int. Vacuum Nanoelectronics Conf. Wuppertal 2011, IEEE Cat. No. CFP11VAC-PRT, 9106–9107.
- M. Rauber, I. Alber, S. Müller, R. Neumann, O. Picht, C. Roth, A. Schoökel, M. E. Toimil-Molares, W. Ensinger, "Highly-Ordered Supportless Three-Dimensional Nanowire Networks with Tunable Complexity and Interwire Connectivity for Device Integration", Nano Lett. 2011, 11 (6), 2304–2310.
- S. Müller, C. Schötz, O. Picht, W. Sigle, P. Kopold, M. Rauber, I. Alber, R. Neumann, and M. E. Toimil-Molares, "Electrochemical Synthesis of $\text{Bi}_{1-x}\text{Sb}_x$ Nanowires with Simultaneous Control on Size, Composition, and Surface Roughness", Cryst. Growth Des., 2012, 12 (2), 615–621.
- O. Picht, S. Müller, I. Alber, M. Rauber, J. Lensch-Falk, D.L. Medlin, R. Neumann, and M. E. Toimil-Molares, "Tuning the Geometrical and Crystallographic Characteristics of Bi_2Te_3 Nanowires by Electrodeposition in Ion-Track Membranes", J. Phys. Chem. C, 2012, 116 (9), 5367–5375.
- P. Serbun, F. Jordan, A. Navitski, G. Müller, I. Alber, M.E. Toimil-Molares, and C. Trautmann, "Copper nanocones grown in polymer ion-track membranes as field emitters", Eur. Phys. J. Appl. Phys., 2012, 58 (1), 10402-1–5.

Gedichte sind gemalte Fensterscheiben

Gedichte sind gemalte Fensterscheiben.
Sieht man vom Markt in die Kirche hinein,
Da ist alles dunkel und düster;
Und so sieht's auch der Herr Philister.
Der mag denn wohl verdrießlich sein
Und lebenslang verdrießlich bleiben.

Kommt aber nur einmal herein!
Begrüßt die heilige Kapelle;
Da ist's auf einmal farbig helle,
Geschicht und Zierat glänzt in Schnelle,
Bedeutend wirkt ein edler Schein,
Dies wird euch Kindern Gottes taugen,
Erbaut euch und ergetzt die Augen!

Johann Wolfgang von Goethe

Contents

1	Introduction	1
I	Synthesis of metallic nanowires and nanogaps	7
2	Ion track technology and electrodeposition of nanowires	8
2.1	Heavy ion irradiation	9
2.2	Chemical etching	11
2.3	Electrodeposition of nanostructures	12
2.3.1	Basics of electrodeposition	12
2.3.2	Electrodeposition in ion-track etched membranes	14
2.3.3	Synthesis of porous nanowires by dealloying	16
2.3.4	Synthesis of nanogaps by on-wire lithography	17
3	Experimental	19
3.1	Fabrication of ion-track etched membranes	19
3.2	Electrodeposition of nanowires	19
3.3	Characterization methods	20
4	Synthesis and characterization of nanowires separated by nanogaps	22
4.1	AuAg alloy nanowires	22
4.1.1	Composition analysis	22
4.1.2	Nanowire morphology before and after dealloying	25
4.2	Segmented nanowires and nanogaps	29
4.2.1	Control on segment length	29
4.2.2	Formation of nanogaps by dealloying	35
4.2.3	Influence of annealing	39
5	Conclusions	41
II	Surface plasmons in individual nanowires and dimers	43
6	Surface plasmons in individual nanostructures	44
6.1	Optical properties of Au and Ag	44
6.2	Plasmonic properties of nanospheres	46
6.3	Plasmonic properties of single nanowires	47
6.4	Plasmonic properties of coupled systems	53

7	Methods	58
7.1	Electron energy loss spectroscopy	58
7.2	Finite integration simulation	61
8	Multipole surface plasmons in nanowires analysed by EELS-STEM	62
8.1	Influence of nanowire dimensions	63
8.2	Influence of composition and morphology	69
8.3	Dispersion relation of single nanowires	75
9	Multipole surface plasmons in nanowire dimers analysed by EELS-STEM	79
9.1	Capacitively coupled nanowire dimers	80
9.2	Capacitively coupled nanowire heterodimers	88
9.3	Conductively coupled nanowire dimers	96
10	Conclusions and Outlook	107

Chapter 1

Introduction

Metallic nanoparticles exhibit fascinating color effects, which differ strongly from those of metallic bulk material. They are based on the potential to excite localized surface plasmon (SP) resonances, which are collective resonant electronic oscillations on the nanoparticle surface. A SP resonance is characterized by the generation of a large field enhancement close to the nanoparticle surface, and high absorption and scattering cross sections.

Consequences of these plasmonic effects were already observed at the time of the Romans and in the Middle Ages. An example are the stained glass windows in many Gothic cathedrales. These windows feature a variety of different colors when regarding a window from inside the church (in transmission mode). The same colors can not be viewed from the outside (in reflection mode). These colors are caused by SP resonances in metallic nanoparticles of varying sizes and compositions in the glass. Since these parameters determine the resonance frequency, specific particles in the glass sustain a particular resonance frequency and consequentially enhanced scattering and absorption cross sections at that frequency. Therefore, the resonance frequency is strongly reflected but not transmitted through the window.

Nowadays, SP resonances in gold (Au) and silver (Ag) nanostructures are intensively investigated due to their potential for applications such as surface enhanced Raman spectroscopy (SERS),¹⁻³ surface enhanced infrared spectroscopy (SEIRS),^{4,5} sensorics,⁶⁻¹⁰ solar cells,¹¹⁻¹³ and waveguiding below the diffraction limit of light.^{14,15} A variety of nanostructures have been tested for these applications as, for example, single nanoparticles,^{3,9} nanoshells,¹⁶ and nanowires,^{4,5,15,17} as well as ordered arrays¹⁸⁻²¹ and self-assemblies of these structures.²²⁻²⁴ In the case of nanowires, resonances of several frequencies are excitable. Due to the two different axis lengths of the wires the resonances split into two branches, longitudinal resonances due to SP waves in

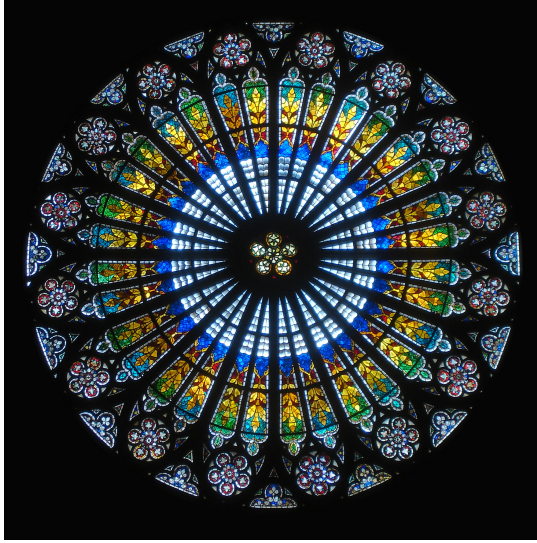


Figure 1.1: Rose window of the cathedral of Strasbourg. The different colors in the window are due to SP resonances in the nanoparticles of different composition inserted in the glass (Source: Wikipedia).

the direction of the wire axis, as well as transversal resonances corresponding to oscillations in the direction perpendicular to it. In particular, the longitudinal resonance frequencies are tunable to a high degree by adjusting wire length and diameter.^{25–27} Additionally, multipolar modes can be excited efficiently in such elongated structures. So far, several authors have evidenced that multipolar longitudinal SP resonances in nanowires give rise to same or higher SERS efficiencies than the respective dipolar resonances.^{20,21} Among all modes, only those having an even number of charge maxima along the wire (bright modes) can couple efficiently to incident far-field radiation. Nevertheless, investigation of modes having an odd number of maxima along the wire (dark modes) is crucial, since coupling to dark modes allows for waveguiding of light, avoiding radiative losses and can therefore be efficiently employed in nanophotonic devices.²⁸

Particular interest was most recently focused on the excitation of SP resonances in two nanostructures separated by a small gap, so-called nanostructure dimers. In such structures, coupling between the SP modes of the individual structures leads to the formation of new modes.^{29–34} It is known that the excitation of specific modes in dimer-systems with very small gap sizes (few nm) results in the generation of extremely high field enhancements, strongly localized at the position of the gap. For such a configuration, the enhancement factor and resonance frequency depend not only on wire aspect ratio and material, but as well on the gap size.³⁰ As an example, at 1 nm distance from one end of a single Au nanowire in vacuum with μm -length and

100 nm diameter the field is enhanced by a factor of about 18. In a gap of 10 nm, separating two wires with the identical dimensions as the single one and at the same distance from the surface, the field is enhanced by a factor of about 180.

Besides the possibility to excite SP resonances with an electromagnetic wave, the resonances can be generated by the electric field of fast electrons in a transmission electron microscope (TEM).^{35,36} The resonances are either analysed by measuring the cathodoluminescence,³⁷⁻⁴⁰ or by electron energy loss spectroscopy (EELS).^{32,33,41-48} Recently, EELS was developed strongly. Up to the year 2006, plasmon resonances were only detectable at energies higher than 2 eV, which excludes the possibility of detecting the regime of the longitudinal SP resonances of Au and Ag nanowires. These resonances were, due to their low energies, hidden by the intense zero-loss peak that results from the elastically scattered electrons. Very recently, strong effort in instrumental development and methodology has led to progress in the feasibility to detect SPs at energies well below 2 eV. This is obtained by monochromatisation of the initial electron beam and improvement of the zero-loss peak subtraction methods.⁴¹

These new developments have stimulated strong research effort in analysing the optical properties of metallic nanostructures by excitation with fast electrons. In contrast to many other methods, the benefit of EELS in a TEM is the possibility to measure high-resolution images of single nanostructures and simultaneously its SP resonances with a spatial resolution of few nanometers, corresponding to the spot size of the electron beam. This yields information not only on how nanostructure geometry and dimension influence the resonance energies, but also on the effect of curvature radius, facets, or surface roughness. For the dimer structures, the gap region is resolvable. Additionally, the electron beam allows the excitation of bright as well as dark modes and the measurement of longitudinal and transversal resonances at energies as low as about 0.3 eV in one single spectrum.

Though the near-field multipolar resonances of single Ag nanowires using EELS in a TEM have been discussed recently,^{46,47} measurements of multipolar resonances on smooth and porous AuAg alloy wires and nanowire dimers have not been reported so far. In addition, measurements employing gaps smaller than 15 nm are rare due to the challenging preparation process.

Several methods to synthesize such small nanogaps are currently under investigation. It has been demonstrated that, using a focused ion beam, gaps with sizes down to 20 nm can be milled in nanostructures of height about 100 nm. The shape and gap size are well controlled and reproducible.⁴⁹ Even smaller gaps down to about 5 nm are being prepared by electron beam lithography separating structures with thickness

of about 15 nm.⁵⁰ This method lacks the possibility to control the quality of the nanostructures by varying its crystallinity. The method, termed on-wire lithography (OWL), leads to nanogaps with sizes down to 1 nm.⁵¹ OWL is based on the idea to electrochemically deposit segmented nanowires and subsequently dissolve chemically the middle segment to create a nanogap. This is done by treating the segmented wires with an etchant that chemically reacts only with the material of the middle segment.⁵² The method combines the advantages of electrochemical deposition in templates, *i.e.* the controllability of the dimensions, the crystallinity and morphology^{53–56} in combination with the potential to synthesize nanogaps smaller than 20 nm in a controlled manner.

In this work, Au and AuAg alloy nanowires, segmented Au-rich/Ag-rich/Au-rich nanowires, and AuAg nanowire dimers with small gaps have been fabricated by electrodeposition in the pores of ion-track etched polymer templates. The elements Au and Ag were chosen due to their potential for plasmonic applications. A systematic study has been conducted to explore the influence of the synthesis parameters, such as electrolyte and voltage parameters on the composition of AuAg alloy nanowires. Furthermore, segmented wires and nanogaps have been created applying OWL. The segmented wires were prepared by pulsed deposition. The influence of fabrication parameters such as deposition pulse length, duration of the nitric acid treatment, as well as time of post-annealing was investigated, to achieve nanostructures with tailored dimensions and morphology, and in particular controlled gap sizes.

The plasmonic properties of the synthesized nanostructures have been systematically investigated by EELS in a TEM. This analysis is divided in two parts. In the first part, the multipole SP resonances of Au and smooth and porous AuAg alloy wires are discussed. This delivers crucial information on how the resonance energies depend on a variety of parameters, such as *e.g.* nanowire dimensions, morphology, and composition, which are controlled via the electrodeposition method. The resonance energy of a wire has to be known precisely for applications. In particular, calculations usually do not take into account how factors such as morphology or surface roughness affect the resonance energies. The high resolution provided by EELS in a TEM allows gaining valuable information on their influence.

In the second part, the SP resonances of nanowire dimers have been investigated. Using light microscopy techniques, it is in most of the cases impossible to measure the gap size of a dimer, or distinguish 'perfect' nanowire dimers from two wires that are conductively connected by a small junction. It is described in the synthesis chapter of this work that when creating nanogaps by dissolving the middle part of the seg-

mented nanowires several of the Au-rich segments remain connected by small metallic junctions. The SP analysis, depending on parameters as gap width, dimer symmetry, or junction size, delivers thus further essential information for their applications and enables one to identify capacitively or conductively connected structures.

Part I

Synthesis of metallic nanowires and nanogaps

Chapter 2

Ion track technology and electrodeposition of nanowires

The electrodeposition of nanowires in ion-track etched polymer membranes is a powerful method to synthesize nanowires with well-controlled dimensions and composition.^{54,56–58} Nanowires consisting of metals, semimetals, or semiconductors with lengths between 1 and 100 μm and diameters as small as 15 nm⁵⁸ have been obtained. Furthermore, the method allows the adjustment of surface roughness, crystallinity, and geometry of the nanowires.^{53,55,56,59–64}

The method consists of four steps, which are presented in Figure 2.1.

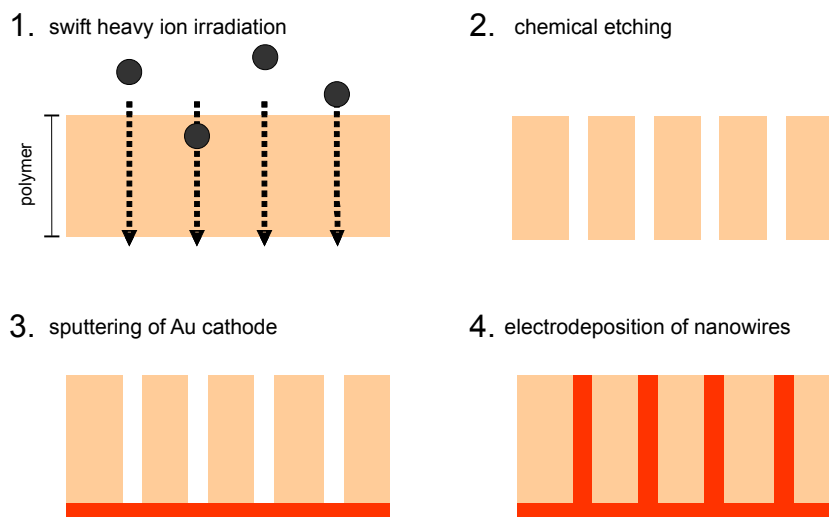


Figure 2.1: Four-step process to synthesize nanowires by electrodeposition in ion track-etched polymer templates. Each step is discussed in more detail in the following sections.

In brief, the process works as follows: Polymer templates with thickness in between

10 and 100 μm are irradiated with heavy ions (initial energy $\sim 11.1 \text{ MeV/u}$) (Section 2.1). A swift heavy ion penetrating through the foil creates a cylindrical ion track. Subsequent chemical etching of the polymer removes selectively the damaged material, resulting in cylindrical nanopores in the polymer exclusively at the positions of the ion-tracks. (Section 2.2). After sputtering of an Au cathode on one side of the membrane, the membrane is employed as template for the growth of nanowires (Section 2.3.2). Each of these steps is discussed in more detail in one of the following sections, focusing on the nanowire parameters that are controlled via the specific step.

2.1 Heavy ion irradiation

Swift heavy ions penetrating into a solid target transfer their energy stepwise to the target material and create cylindrical damage zones, called latent tracks. The characteristics of the collision processes depend on the ion energy: At high energies (above 0.1 MeV/u) the projectile transfers its kinetic energy mainly to the target electrons. This process is therefore called electronic energy loss. For electronic energy loss, the amount of transferred energy during a collision is low and the collisions occur frequently, leading to a regular path of the projectile. In contrast, at energies below 0.1 MeV/u, a large amount of energy is transferred from the ion to the target nuclei. This process is thus called nuclear energy loss. The path of the ion is irregular, containing many kinks.

The regular, straight path of the swift heavy ions in matter in the electronic energy loss regime motivates thus the application of the homogeneous ion tracks in polymer foils for the nanowire template preparation. This process is thus discussed here in more detail.

The track formation by electronic energy loss starts with the transfer of energy from the projectile to target electrons, initiating in this way electron collision cascades. These so-called delta electrons carry away projectile energy and negative charge from the initial path. Positively charged ions remaining in the track zone create by coulomb repulsion an atomic collision cascade. The damage, caused by this atomic cascade, has a lateral extension of only about 10 nm and is called the core of the latent track. The outer zone of damage, created by the delta electrons, is called its halo. The radius of the halo can amount up to 1 μm , being much bigger than that of the core.

Quantitatively, the energy loss per unit length of an ion penetrating through matter is described by the Bethe-Bloch formula:

$$\left(\frac{dE}{dx}\right)_e = \frac{4\pi e^2 \cdot Z_{eff}^2 \cdot Z_t \cdot N}{m_e \cdot v^2} \left(\ln \left(\frac{2m_e c^2 \cdot \beta^2}{I} \right) - \beta^2 - \delta - U \right), \quad (2.1)$$

with e being the elementary charge, m_e the electron mass, v the ion velocity, N the density of target atoms, I the ionization energy of the target atoms, Z_{eff} the equilibrium effective charge of the projectile, Z_t the nuclear charge number of the target atoms and β the velocity in units of the speed of light. The parameters δ and U are correction factors for relativistic effects and for the contribution of electrons from inner atomic shells, respectively. For a specific target material the Bethe-Bloch formula shows that the electronic energy loss depends on the projectile velocity v and on its effective charge Z_{eff} . The effective charge Z_{eff} varies inside the material since ions capture or lose electrons on their way. At high velocities, Z_{eff} is approximately equal to the charge number. Consequentially, at high velocity, projectiles of higher charge number lead to higher electronic energy losses than those with lower charge number, but with the same velocity.

It has been shown previously that for the generation of homogeneous tracks in polymer a certain energy loss threshold has to be exceeded. High Z projectiles are thus preferential. As an example, for Kapton foils homogeneous etching with small pore size distribution is possible if the energy loss exceeds $450 \text{ eV}/\text{\AA}$. Below $180 \text{ eV}/\text{\AA}$, no pores are created, while in the range between these two values etching is possible but a broad pore size distribution is found.⁶⁵

Commonly, polycarbonate membranes are employed for the preparation of nanowire templates. The range of homogeneous energy loss of Au ions accelerated to an energy of 11.1 MeV/n in polycarbonate is about $110 \mu\text{m}$. This length determines the maximum possible thickness of the template and limits thus the nanowire length. The density of tracks is controlled by the fluence of the ion beam (ions/cm^2). Single-pore membranes are created by strong defocusing of the beam and employing a shadow mask during the irradiation equipped with a pin hole of $200 \mu\text{m}$ diameter.^{66–69} Structured ion irradiation with spatial precision better than $1 \mu\text{m}$ is performable with an ion beam microprobe.⁷⁰

Figure 2.2 visualizes the energy loss versus the specific projectile energy for Au ions in polycarbonate. The curves are calculated with the SRIM code.⁷¹ In Figure 2.2a, it is visible that at energies higher than 0.1 MeV/u the nuclear energy loss is negligible, while below 0.02 MeV/u (Figure 2.2b) the energy loss is dominated by the nuclear loss.

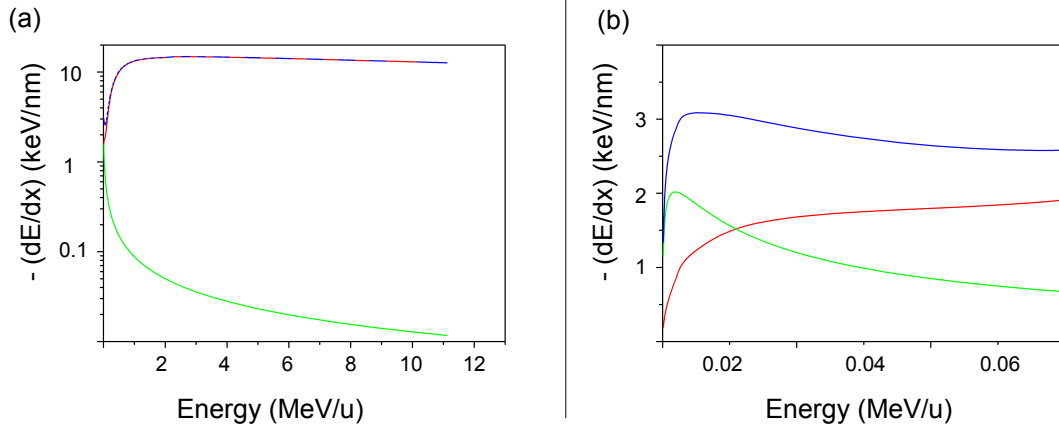


Figure 2.2: Stopping power of Au ions in polycarbonate as a function of specific energy. The red line shows the electronic energy loss, while the green line depicts the nuclear energy loss. The blue line represents the sum of electronic and nuclear energy loss. (a) In the region of high ion energy the electronic energy loss dominates. (b) Only at low energies ($\lesssim 0.02$ MeV/u) the energy transfer is dominated by interaction between projectile and target nuclei.

2.2 Chemical etching

The dissolution of ion tracks in polymer to create nanopores is performed via chemical etching. Fragmented polymer in the ion track leads to increased etching velocities along the tracks compared to those in undamaged material. The etching process is characterized by the ratio between track etching velocity v_T and bulk etching velocity v_B as schematically illustrated in Figure 2.3a. This ratio is sensitive to many parameters, namely etchant content, its concentration, etching temperature, and template material. Control over these parameters provides the possibility to tailor the pore dimensions and geometry. Cylindrical pores are created if $v_T \gg v_B$. The pore diameter is adjustable via variation of the etching time. By increasing the bulk etching velocity, conical and biconical nanowires are developed.^{60,66,67,72,73} The pore size distribution depends on the storage time and condition of the membrane. It has been shown that UV irradiation leads to a narrowing of the pore size distribution.⁷⁴ Finally, the roughness of the pores depends on the template material. In contrast to polycarbonate foils that have smooth pores, polyethylene terephthalate (PET) develops rough pores. This roughness is ascribed to the partially crystalline and amorphous character of this material. It has been shown that amorphous domains etch faster than crystalline ones.⁷⁵ Since the nanowires adopt the shape of the pores, the etching process allows the adjustment of the nanowire geometry and surface roughness.

More details on the etching process of nuclear tracks in solids can be found for

example in Ref. 76.

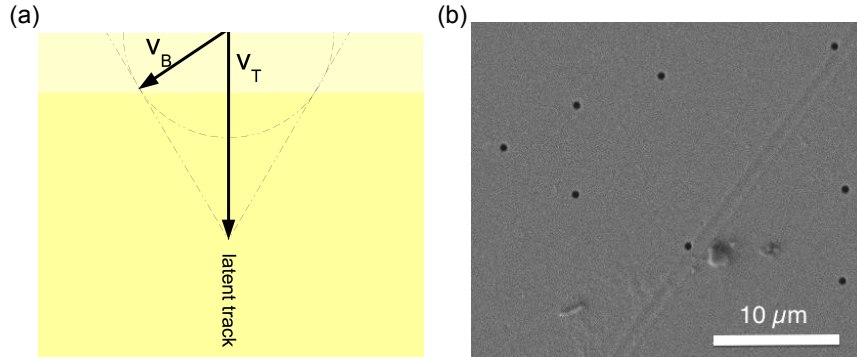


Figure 2.3: (a) Schematical representation of the pore shape dependency on the ratio between bulk etching and track etching rates. (b) Scanning electron microscopy (SEM) image of a polycarbonate foil with randomly distributed pores. The foil is covered with a thin Au layer for SEM characterization.

2.3 Electrodeposition of nanostructures

2.3.1 Basics of electrodeposition

Electrochemical deposition is based on the application of a potential difference between two electrodes immersed in an electrolyte. The potential difference is chosen in such a way that at the cathode ions are reduced and form a deposit. Since the process of electrodeposition is discussed in detail in many textbooks, here the basics of the process are summarized only very briefly.

The equilibrium deposition potential E_{eq} of an electrochemical half-cell is determined versus a reference electrode, which establishes its potential fast and reproducible. E_{eq} can not be directly measured, because it is not possible to make an electrical connection to the solution phase without setting up another electrode with its potential. The potential E_{eq} is given by the Nernst equation:

$$E_{eq} = E^\circ + \frac{RT}{zF} \ln \left(\frac{a_{ox}}{a_{red}} \right), \quad (2.2)$$

where E° denotes the standard potential of the half-cell which is defined versus standard hydrogen electrode, R is the thermal constant, T the temperature, z the number of electrons taking place in the reaction, F Faraday's constant, and a_{ox} and a_{red} are the activities of the ions being reduced and oxidised during the reaction. The activities are proportional to the ion concentrations in the electrolyte.

When applying an external potential, different from the equilibrium potential, to the cathode the concentration of ions in the electrolyte changes by reduction of ions or oxidation of atoms at the electrodes, resulting in a current flow in the electrochemical cell. The overpotential η defines the potential change of the electrochemical cell:

$$\eta = E(I) - E_{eq,cell}, \quad (2.3)$$

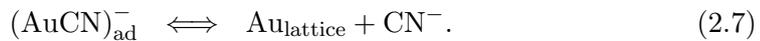
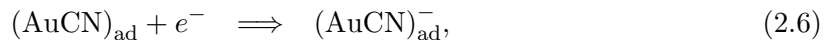
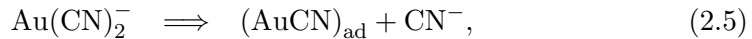
where $E(I)$ is the applied external potential difference between two electrodes, and $E_{eq,cell}$ the equilibrium potential of the cell. The relationship between current density i and overpotential is given by the Butler-Volmer Equation:

$$i = i_0 \left(e^{\frac{-\alpha z F \eta}{RT}} - e^{\frac{(1-\alpha) z F \eta}{RT}} \right), \quad (2.4)$$

where i_0 is the exchange current density and α the transfer coefficient. The exchange current density is the intrinsic rate of electron transfer at the cathode and the anode, occurring at zero overpotential. The current and thus the rate of reactions can be controlled by varying the overpotential of the cell. For low overpotentials, the current increases almost linearly with the overpotential. In this region the charge transfer is the slowest step in the electrodeposition process and determines the growth velocity. In contrast, for high overpotentials the transport of ions is the slowest step and the Butler-Volmer Equation is not valid. The surroundings of the cathode are depleted from the ions and each ion that reaches the cathode is immediately reduced. In this region, the current remains constant with increasing overpotential.

The electrodeposition of gold (Au) and silver (Ag) has been intensively studied, due to their high electrical conductance, and resistance to corrosion of these metals. This highlights their potential for many applications in electronics, medicine and optics. The combination of Au and Ag is also interesting for the investigation of the electrodeposition of alloy micro- and nanostructures. Both grow as face-centered cubic crystals with very similar lattice constants, being 4.08 Å (Au) and 4.09 Å (Ag), and thus form a solid solution over the whole composition range.

For the electrodeposition of Au from the $\text{Au}(\text{CN})_2^-$ complex, two mechanisms have to be distinguished. During reduction at low overpotentials, chemical adsorbates are first created which are reduced in a second step:



At high overpotentials, the $\text{Au}(\text{CN})_2^-$ - ions are directly reduced.



The equation for the deposition of Ag from cyanidic complexes is given by:



During the deposition of alloys, codeposition takes place if both ion species have the same deposition potential and are both present in the electrolyte. The deposition potentials are controlled by varying the concentration of the ions. For the ion species with the lower standard potential, the concentration in the electrolyte has to be increased compared to the one with the higher potential to adjust their deposition potentials. The standard potential of $\text{Ag}(\text{CN})_2^-/\text{Ag}$ versus Ag/AgCl reference electrode is -0.53 V, and for $\text{Au}(\text{CN})_2^-/\text{Au}$ it is -0.82 V.⁷⁷

Furthermore, it is as well possible to deposit multilayer structures. In this case, pulsed deposition is applied. At the lower deposition potential, only ions with lower standard potential are reduced, while both ion species are reduced at the second potential. The content of the segments is tailored by varying the ion concentrations in the electrolyte.

2.3.2 Electrodeposition in ion-track etched membranes

During potentiostatic nanowire deposition, the growth process can be monitored by recording the current-vs-time curve. Figure 2.4a shows a typical curve. It reveals three different zones that are highlighted in the figure with different colors. A strong decrease of the absolute current value starts at the moment when a potential is applied (I). It is due to the reduction of ions in the vicinity of the cathode and the formation of a depletion zone close to the electrode, called diffusion layer, that grows into the bulk solution. During the growth of cylindrical nanowires, the current density remains almost constant (II). If the nanowire length equals the template thickness, caps start to grow on top of the wires on the template surface. This is indicated by an increase of the absolute current value which is due to the enlarged surface area (III). Figure 2.4b shows exemplarily a SEM image of Au nanowires with diameter of about 200 nm, created by potentiostatic electrodeposition.

According to Faraday's law, the weight of a product of electrochemical reaction at an electrode is proportional to the electric charge Q , passing through the electrochemical cell. If the growth is homogeneous the experimental charge, being the integral of the I-t curve, is thus equivalent to the theoretical value calculated applying Faraday's law:

$$Q_{theo} = \frac{zF}{A_{wt}} L\pi(D/2)^2\rho \times N_{\text{pores}}, \quad (2.10)$$

where A_{wt} is the atomic weight of the deposit, z the number of electrons involved in the deposition, F Faraday's constant, D and L the nanowire diameter and length, ρ the density, and N_{pores} the number of pores in the membrane. For homogeneous nanowire growth, this enables to control the nanowire length. The deposition process is therefore stopped after the amount of charges, necessary to obtain a specific length, has been reached. In the case that the theoretically calculated length is smaller than the length obtained experimentally, it can be concluded that the nanowires did not grow homogeneously, *i.e.* not all pores in the membrane have been filled.

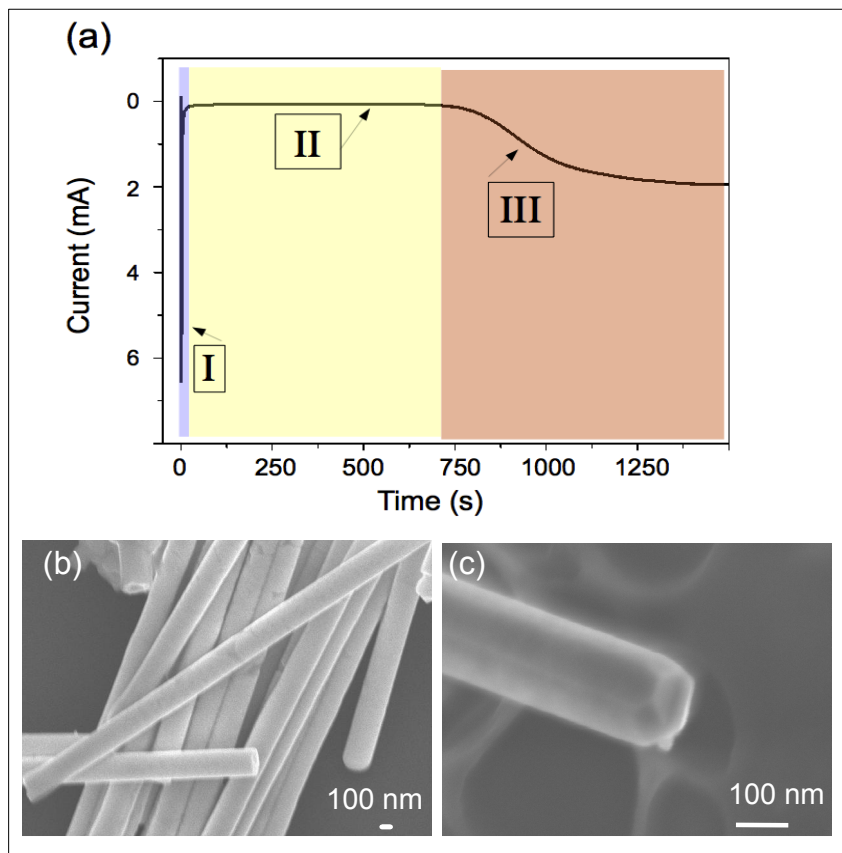


Figure 2.4: (a) Current-versus-time curve recorded during the deposition of Au nanowires with a cyanide based electrolyte. The three characteristic zones of nanowire growth are highlighted by the different colors. (b) Group of Au nanowires on a silicon substrate and (c) faceted AuAg alloy nanowire deposited at -0.5 V vs Ag/AgCl at 60 °C.

In particular, the electrodeposition of Au wires in ion-track etched polymer templates has been studied in detail.^{55,62} The authors demonstrated that single-crystalline and polycrystalline nanowires can be created by varying the deposition parameters. High temperature, high ion concentration in the electrolyte, and low overpotentials feature single-crystalline growth. Exemplarily, Figure 2.4c shows a faceted AuAg

alloy nanowire deposited in a three-electrode arrangement at a voltage of -0.5 V vs Ag/AgCl at $60\text{ }^\circ\text{C}$. The facettes at the nanowire end indicate the growth of very big crystals or even single-crystalline growth.

2.3.3 Synthesis of porous nanowires by dealloying

Binary or multicomponent alloy materials open up the possibility to dissolve in a selective manner chemically less noble components, while atoms of nobler metals are less dissolved. The process is called dealloying and is intensively studied for metal composites, leading to nanoporous Au, Ag, Cu, Pt or Pd.^{78–80} The porosity of the structures can be tuned via the initial material composition and the dealloying parameters such as etching concentration and time. Thus, for example, it has been shown that with increasing diffusion coefficient of the nobler element in a complex the length scale of ligaments/channels in a nanoporous metal increases.⁸¹

Most attention is paid to the AuAg complex, due to the broad range of applications, such as catalysis, sensing and SP excitations.^{82–85} In this complex, Ag is dissolved using nitric acid. The different steps of the dealloying process are shown in Figure 2.5.^{86,87} The dealloying is initiated by layer-by-layer dissolving of Ag atoms on the

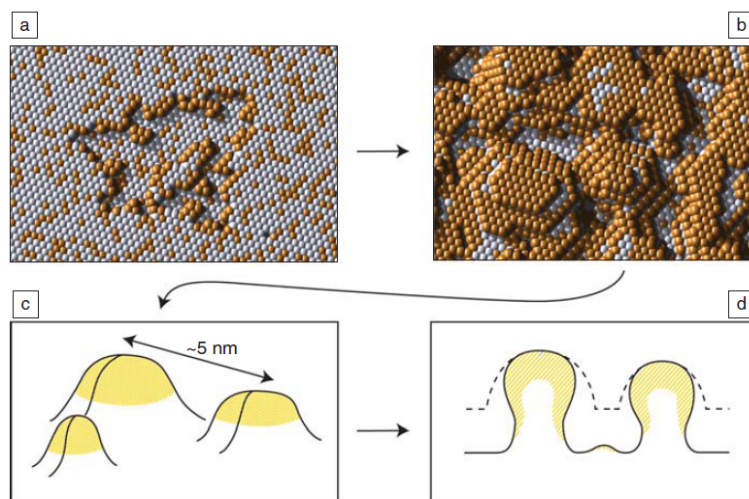
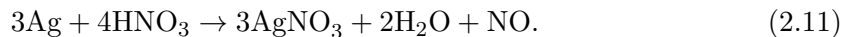


Figure 2.5: Process of the evolution of porosity by dealloying of a AuAg film. The different steps leading to the formation of a porous network are: (a) Layer-by-layer dissolving of Ag atoms (grey), (b) diffusion of Au atoms (orange) on the surface of the material to form Au islands, and (c, d) undercutting of islands. The figure is adapted from Ref. 87 (DOI).

surface of the material (Figure 2.5a). If the resulting Au adatom concentration is larger than the equilibrium adatom concentration, the Au atoms move by diffusion on

the surface of the material and form Au islands. (Figure 2.5b). The process continues until the surface is covered mainly by Au atoms. During this time, islands can be undercut, increasing the surface area (Figures 2.5c and 2.5d). An intrinsic porous network is formed consisting of a AuAg alloy core enclosed by a passivating shell of the Au atoms. That the finally resulting porous structures consist mainly of Au is due to a secondary coarsening process of the structure below the dissolution front, leading to an enrichment of Au in the alloy. Surface diffusion of the Au atoms can occur already at room temperature due to the small curvature radii of nanoparticles compared to bulk material. During the dissolution of Ag in AuAg alloy nanowires, porous nanowires with surface areas higher than porous bulk and smooth nanowires are achieved.^{28,88–91}

The chemical equation describing the dissolution of Ag atoms by treatment with nitric acid is given by:



2.3.4 Synthesis of nanogaps by on-wire lithography

The realization of nanoparticles separated by nanogaps with well-controlled dimensions and high reproducibility is a challenge. Such structures are interesting devices to design, for example, single-electron transistors or SERS and SEIRS active substrates.^{92–94} Recently, Qin *et al.* demonstrated the synthesis of such structures employing a process named on-wire lithography.⁵² The process is schematically depicted in Figure 2.6. In a first step segmented Au/Ag/Au nanowires of different materials are electrodeposited (Step 1). The length of the segments is controlled via recording the charge consumed during wire growth, and is thus adjusted by the pulse length. Secondly, the template is dissolved and the nanowires are drop cast onto a substrate (Step 2). A thin layer of silicon (Si) of about 50 nm is deposited onto the nanowires (Step 3). The authors reported that the Si layer on one side of the wires was necessary to ensure the stability of the nanostructures after dissolution of the middle segment. Sonification releases the Si coated wires from the substrate (Step 4). Finally, the middle segment is etched away by nitric acid (Step 5).

Different metals have been tested so far, including Pt, Ni, Ag, and Au.^{51,52} The smallest gap that has been reported applying this technique is 1.6 nm, separating Au segments with diameter of 35 ± 5 nm.⁵¹

In Ref. 95, synthesis of segmented AuAgAu nanowires applying this process was reported. The segmented wires were prepared by exchanging the electrolyte after the

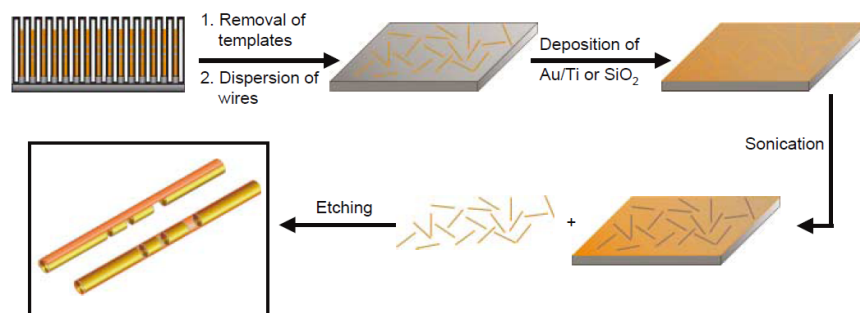


Figure 2.6: Scheme of the process called on-wire lithography to create nanogaps separating nanowire segments. Figure adopted from Ref. 52 (DOI). Reprinted with permission from AAAS.

deposition of each segment. Instead of depositing Si or SiO₂ on the nanostructures the wires were fixed on their substrate with saturated 11-mercaptoundecanoic acid to ensure stability. In the work presented here (compare Section 4.2.2), it is demonstrated that the nanostructures appeared stable without the need of special layers or linkers.

Chapter 3

Experimental

3.1 Fabrication of ion-track etched membranes

For the preparation of ion-track etched membranes, polycarbonate foils (Makrofol N by Bayer, thickness 30 μm) were irradiated with heavy ions at the linear accelerator UNILAC at GSI Helmholtzzentrum für Schwerionenforschung. The projectiles were Au and U ions of charge state 25^+ and 28^+ , respectively, which were accelerated to an energy of about 11.1 MeV/n before hitting the foils. The fluence of the ion beam was set to 10^9 ions/cm².

The latent tracks were chemically etched in 6 M NaOH solution at 50 °C to create cylindrical nanochannels. These parameters lead to an etching rate of the tracks in polycarbonate of about 23 nm/min. The resulting nanochannel diameter increases linearly with etching time. Thus, the time was chosen accordingly to obtain the diameter of interest.

3.2 Electrodeposition of nanowires

After sputtering a thin Au layer on one side, the foil was inserted into a two-compartment electrodeposition cell (Figure 3.1). The Au layer served as the cathode for the electrodeposition process. It was reinforced by electrodeposition of a copper (Cu) layer on the backside of the foil. This Cu layer ensured the stability of the cathode when dissolving the polymer and completely covered the pore openings.

Electrodeposition of the nanowires was performed in a three-electrode arrangement, using a Ag/AgCl (sat. KCl) electrode as reference electrode and a platinum coil as counter electrode. All potentials indicated in the following sections are given versus the reference electrode potential. For the deposition of AuAg alloy nanowires

and segmented AuAg nanowires, two different electrolytes and different deposition voltages were used, as discussed in the following sections in more detail. The two different electrolytes that were studied contained $\text{KAu}(\text{CN})_2$ and $\text{KAg}(\text{CN})_2$ in the ratio 1:1 and 2.5:1. In addition, an amount of 0.25 M Na_2CO_3 ensured an alkaline electrolyte (pH 13). This avoids release of toxic HCN. All depositions were performed at 60 °C.

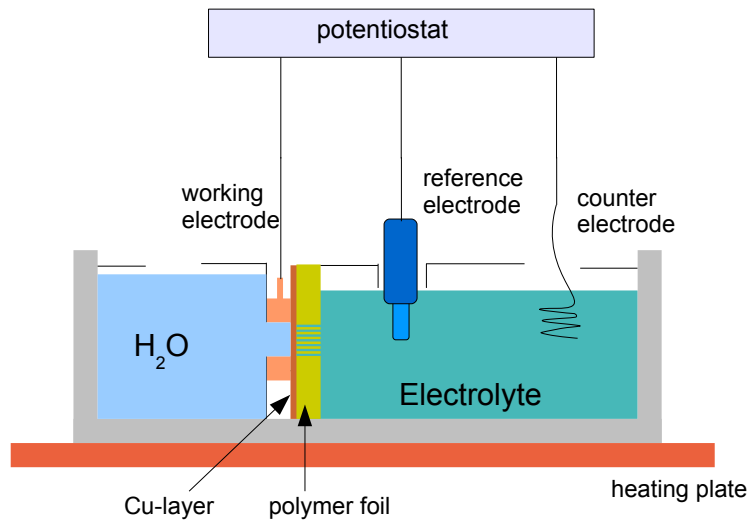


Figure 3.1: Experimental set-up for the electrodeposition of nanowires in the pores of a heavy ion irradiated polycarbonate foil.

3.3 Characterization methods

For the characterization of the deposited nanowires, the polycarbonate foil was dissolved using dichloromethane. The dichloromethane was exchanged at least five times to dissolve the polymer completely. The nanowire array was finally dipped into isopropanol, and the nanowires were released from the backlayer by ultrasonication over about 10s. For characterization, the isopropanol solution containing the nanowires was dropped on a substrate. After evaporation of the isopropanol, nanowires remained randomly distributed on the substrate. The choice of the employed substrate depended on the analysis technique, as presented below.

Field-emission scanning electron microscopy (FESEM) was performed using a JSM-7401 microscope (JEOL) operating at 1-30 kV. The microscope is equipped with a secondary emission (SE) detector, employed to analyse the surface morphology and nanowire dimensions. Different segments of the AuAg nanowires were visualized in the backscattering (BS) mode. Since the backscattering cross section of an element

depends on the atom number Z , a segment consisting of Au appears brighter in the SEM image than a segment consisting of Ag. For the SE and BS measurements, boron doped silicon (Si) wafers served as substrates. Gap sizes were measured in the SE mode and in some cases in scanning transmission mode (STEM), employing 30 nm thick silicon nitride (Si_3N_4) membranes (Plano GmbH) as substrate. The Si wafers and the Si_3N_4 membranes are both stable against the treatment with nitric acid, which is the crucial step for the nanogap preparation. Both types of substrate are hydrophobic.

The SEM is equipped with an EDX-detector (Bruker). The spectra were measured applying an acceleration voltage in the SEM of 20 kV. The quantitative composition analysis was performed using the Bruker Software Quantax. For the energy dispersive x-ray spectroscopy (EDX), Cu grids with thin carbon films (Plano GmbH) were used as substrates. These thin carbon films avoid intense peak in the spectra originating from the background material that lead to sophisticated analysis.

Chapter 4

Synthesis and characterization of nanowires separated by nanogaps

The following chapter describes the synthesis of AuAg nanostructures by electrodeposition in ion-track etched polymer templates and the characterization of the structures.

In Section 4.1 the synthesis of AuAg alloy nanowires of different composition is presented. AuAg alloy nanowires are of large interest for plasmonic application because the wavelength of the transversal SP resonance can be tuned in the visible range by varying the composition. First, we studied systematically the influence of voltage and electrolyte concentration on the nanowires. Secondly, the morphology and composition of the AuAg nanowires before and after the dealloying process was investigated. A good understanding of both steps is essential for the synthesis of segmented nanowires and nanogaps, as presented in Section 4.2. In this second part, different aspects of the synthesis of segmented wires by pulsed deposition and the subsequent dissolution of the middle segment to create nanogaps are discussed. These aspects are: influence of the length of the applied pulses, nitric acid treatment, and post-annealing of the structures.

4.1 AuAg alloy nanowires

4.1.1 Composition analysis

To electrodeposit segmented AuAg nanowires consisting of Au and Ag segments as pure as possible, it is essential to explore the influence of deposition conditions, in particular electrolyte composition and applied voltage, on the composition and morphology of the nanowires.

Figure 4.1 shows two cyclic voltammograms, measured using two different electrolytes. The first line corresponds to a voltammogram using an electrolyte containing 20 mM $\text{KAu}(\text{CN})_2$ (blue line), while the second one corresponds to an electrolyte containing 20 mM $\text{KAg}(\text{CN})_2$ (red line). Further parameters that were used are presented in Section 3.2. A scan rate of 30 mV/s and a step size of 5 mV were chosen. A gold wire served as electrode. The voltage was ramped from -0.4 to -1.4 V, and the current flowing in the cell was measured. When approaching -1.4 V, the ramping was inverted and the current flowing in the cell was measured again for the backward scan.

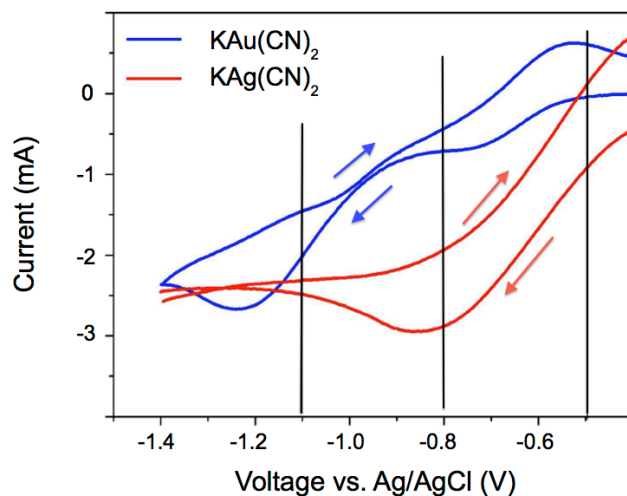


Figure 4.1: Current-vs-voltage curves measured in a three-electrode set-up with an electrolyte containing 20 mM $\text{KAu}(\text{CN})_2$ (blue line) and a second electrolyte containing 20 mM $\text{KAg}(\text{CN})_2$ (red line). The vertical black lines mark the voltages (-0.5, -0.8, and -1.1 V) that were chosen for further investigation of the synthesis process.

Comparing the two voltammograms reveals that the current onset for the reduction of $\text{Ag}(\text{CN})_2^-$ -ions starts at lower negative potentials than for $\text{Au}(\text{CN})_2^-$ -ions. At a voltage of -0.5 V the current flowing in the cell with the Au-electrolyte is only 40 μA , while with the Ag-electrolyte the current is 1 mA. We found the diffusion limited minima at the given conditions for the Ag-electrolyte at -0.85 V and for the Au-electrolyte at -1.25 V.

AuAg nanowires were electrodeposited using two different electrolytes. One containing 50 mM $\text{KAu}(\text{CN})_2$ and 20 mM $\text{KAg}(\text{CN})_2$ (Au:Ag ratio 2.5:1), and another one containing 50 mM $\text{KAu}(\text{CN})_2$ and 50 mM $\text{KAg}(\text{CN})_2$ (Au:Ag ratio 1:1). For each of the two electrolytes, nanowires were deposited at three different voltages: At -0.5 V it was intended that almost only $\text{Ag}(\text{CN})_2^-$ -ions are reduced, but with very slow deposition rate. At -0.8 V both $\text{Au}(\text{CN})_2^-$ - and $\text{Ag}(\text{CN})_2^-$ ions are reduced. For an identical concentration of $\text{Au}(\text{CN})_2^-$ - and $\text{Ag}(\text{CN})_2^-$ ions in the electrolyte, a higher

deposition rate of Ag was expected. Finally, at -1.1 V both ion species are deposited at high rate.

Figures 4.2a and 4.2b show current-vs-time curves recorded during the deposition of six AuAg nanowire arrays under these conditions. In Figure 4.2a, the electrolyte with Au:Ag ratio of 2.5:1 was used, whereas in Figure 4.2b the Au:Ag ratio was 1:1. By integration of the current-vs-time curves, the amount of consumed charges was calculated, and in all cases the process was stopped after a transfer of 100 mC at the electrode. All current-vs-time curves show similar characteristics that were

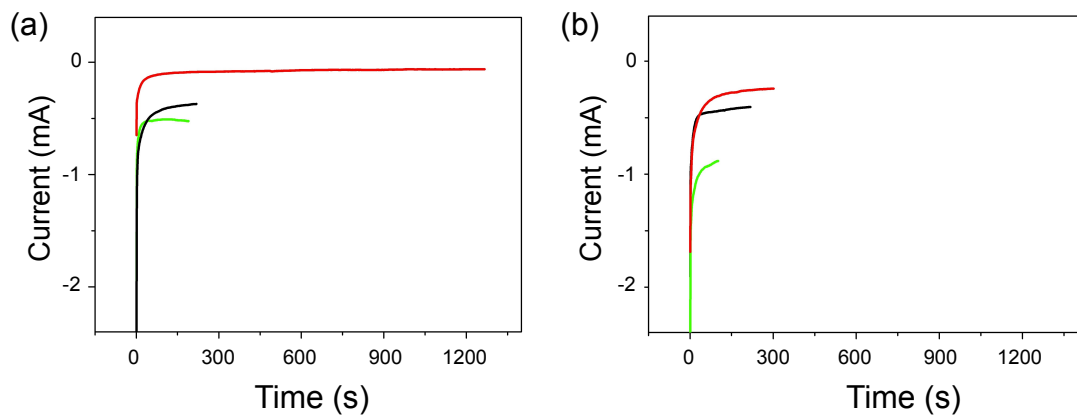


Figure 4.2: Current-vs-time curves recorded during the electrodeposition of AuAg alloy nanowires, using an electrolyte with Au:Ag ratio of (a) 2.5:1 and (b) 1:1. The applied potentials versus Ag/AgCl reference electrode are in both figures -0.5 V (red line), -0.8 V (black line) and -1.1 V (green line).

observed previously for nanowire deposition (see Section 2.3.2): A strong current decrease, starting at the moment when the deposition potential is applied, and an almost constant current during the nanowire deposition. With increasing $\text{KAg}(\text{CN})_2$ amount in the electrolyte and increasing potential, the recorded current increases. SEM images of typical nanowires obtained from these depositions are presented in the following section.

Bundles of nanowires have been analysed by EDX in SEM to estimate the Au:Ag ratio of the wires depending on the electrolyte content and the deposition voltage. For this analysis, the wires, suspended in isopropanol, were drop-cast on carbon-coated Cu TEM-grids (Plano GmbH). Figure 4.3 shows details from EDX spectra, each of them corresponding to one of the six different samples. The details show an energy interval from 1.5 to 4.0 keV, which includes the L_{α} - and L_{β} -peaks of Ag and the M_{α} -peak of Au. The spectra have been normalized to the peak height of the M_{α} Au peak for clarity.

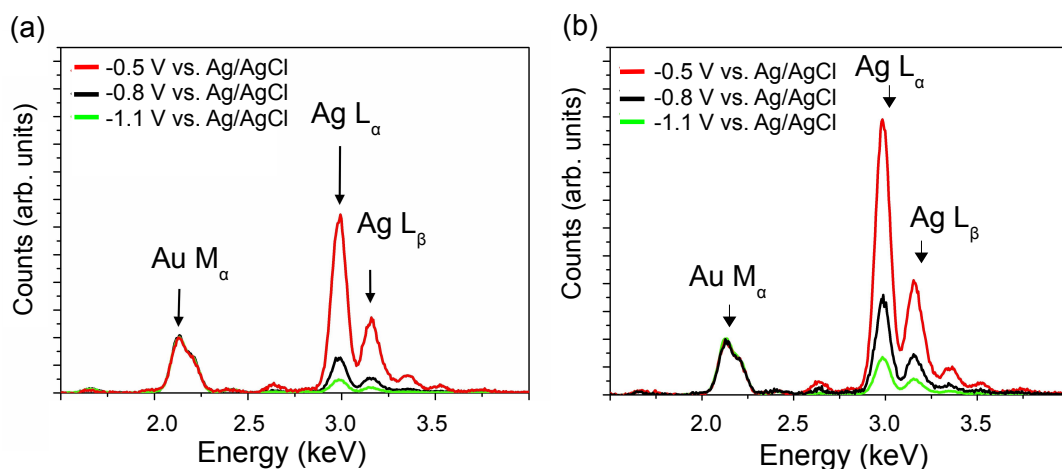


Figure 4.3: EDX spectra of AuAg alloy nanowires. In (a) the nanowires were deposited with an electrolyte of Au:Ag ratio 2.5:1 and in (b) with an electrolyte of Au:Ag ratio 1:1. The deposition voltages were in (a) and (b) -0.5 V (red line), -0.8 V (black line) and -1.1 V (green line).

Potential	Electrolyte Au:Ag ratio	Nanowire Au:Ag atomic percent
-0.5 V	2.5:1	15:85
-0.8 V	2.5:1	40:60
-1.1 V	2.5:1	60:40
-0.5 V	1:1	10:90
-0.8 V	1:1	20:80
-1.1 V	1:1	40:60

Table 4.1: Au:Ag ratio in the nanowire bundles for different electrolyte contents and deposition potentials.

For both electrolytes, a similar trend was confirmed: With increasing negative potential the Au:Ag ratio of the wires increases. The quantitative values for the Au:Ag ratio of the six different samples are summarized in Table 4.1. For each sample, four to six bundles of nanowires have been analysed. The ratio for one sample determined for the different bundles varies by ± 4 %. With increasing potential, the Au:Ag ratio of the wires approaches the Au:Ag ratio of the electrolyte since the diffusion limited region is approached for both ion species with increasing overpotential.

4.1.2 Nanowire morphology before and after dealloying

For the synthesis of nanogaps, the segmented nanowires have to be treated with

nitric acid to dissolve the Ag segments.

As explained above for the chosen electrolytes, AuAg alloy nanowires were deposited, whose composition varies between 40 and 90 % Ag with applied voltage and electrolyte content. During the dissolution in nitric acid, thus, dealloying plays an essential role for both Au-rich and Ag-rich segments. To understand the dealloying process and optimize the experimental conditions for nanogap creation, we have analysed the morphology and the composition of the nanowires before and after nitric acid exposure. Figures 4.4a and 4.4c depict nanowires on a Si substrate. They were deposited with an electrolyte containing $\text{Au}(\text{CN})_2^-$ and $\text{Ag}(\text{CN})_2^-$ ions in the ratio 2.5:1. The potentials (a) -1.1 V, and (c) -0.5 V were applied, respectively. Under these deposition conditions, the average Au:Ag composition of the nanowires is 60:40 (a) and 15:85 (b) (see Table 4.1). After imaging and EDX analysis the samples were dipped for 3 h into concentrated nitric acid. Subsequently, the samples were rinsed several times with deionized water, and placed for one hour in dichloromethane. Figures 4.4b and 4.4d show wires corresponding to the identical samples as in (a) and (c). The insets of the figures depict parts of the wires with higher magnification.

Comparing the SEM image in Figures 4.4a and 4.4c, one can see that the changes in the wire morphology are minor. This is reasonable since the nanowires contained initially a high Au concentration of 60 %. Hence, a Au passivation layer on the surface is formed quickly, preventing morphology changes as discussed in Section 2.3.3. This agrees with results in Ref. 88, where evolution of porosity for nitric acid treated $\text{Au}_x\text{Ag}_{1-x}$ films was only found for $x \leq 0.4$. No diameter change of the wires could be measured in the SEM images. It is thus concluded that if diameter changes occur, they are smaller than the SEM measurement uncertainty, which is about 10 nm. In contrast, in Figure 4.4b the nanowires had initially a Ag content of about 85 %, leading to strong morphology modifications by the nitric acid treatment (Figure 4.4d). SEM analysis depicts two types of wires. On the one hand, very porous wires were formed whose diameter is reduced by a factor of about 2.5. These nanowires have been separated into segments of varying length. On the other hand, parts were found that have lost the wire shape. Instead, particles with various shapes were formed (see inset of Figure 4.4d). From the positions of several of the particles the initial shape of the wire can be identified.

Figures 4.5a and 4.5c depict high-resolution SEM (HRSEM) images of the nanowires deposited with the same electrolyte as in the figures above (Au:Ag 2.5:1). The applied voltage was -1.1 V. A low SEM acceleration voltage of 1.5 kV was used, to analyse the surface morphology of the wires in detail. The HRSEM images reveal the surface

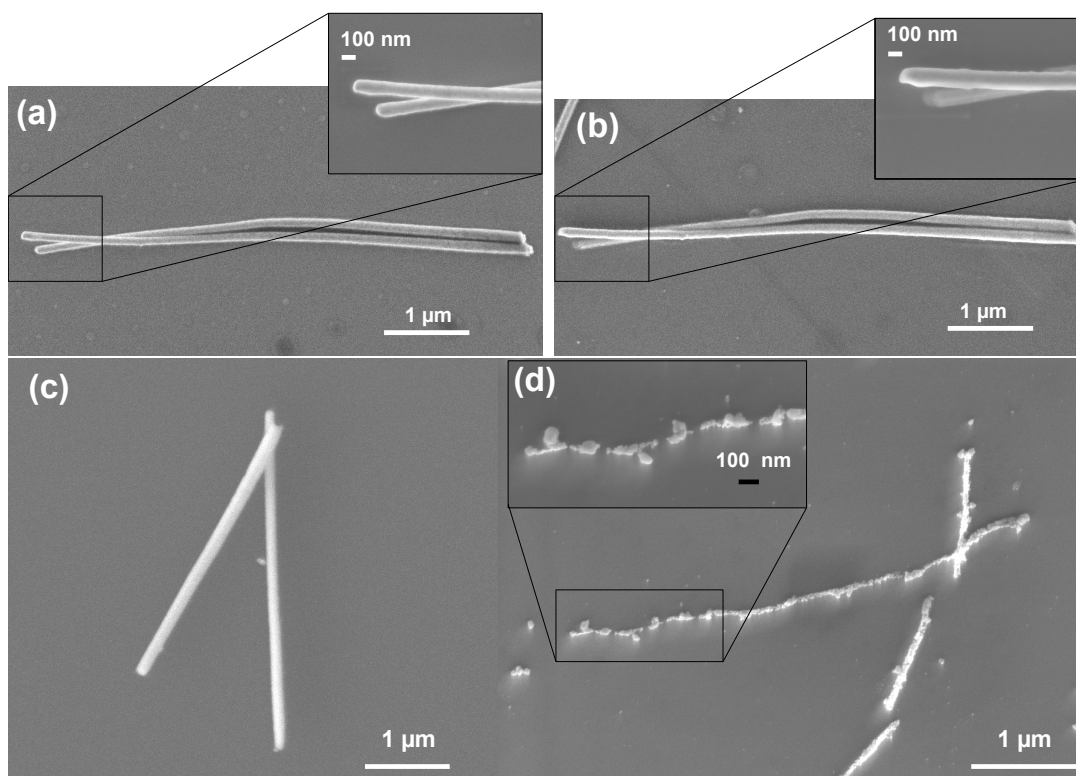


Figure 4.4: Left: SEM images of AuAg alloy nanowires grown with an electrolyte of Au:Ag ratio 2.5:1. The applied voltage was -1.1 V in (a) and -0.5 V in (c). Right: SEM images of wires after treatment with concentrated nitric acid for three hours. The insets depict parts of the wires with higher magnification. In (a) and (b) exactly the same wires are shown before and after nitric acid treatment, while in (c) and (d) different but typical wires of the same sample are depicted.

before (a, b) and after (c, d) nitric acid treatment. Obviously, in both cases the wire surface exhibits a certain roughness, especially at the nanowire ends, it is not possible to judge if the roughness has been changed by the nitric acid treatment. It is important to notice that all wires exhibit a certain roughness in the context of Section 8.1, where the origin of deviations between measured and calculated SP resonance energies is discussed.

Figures 4.6a and 4.6c depict nanowires deposited with an electrolyte of Au:Ag ratio 1:1, applying the potentials (a) -1.1 V, and (c) -0.5 V. Under these deposition conditions, the average composition of the nanowires is 40:60 (a) and 10:90 (b) (see Table 4.1), *i.e.* they contain a higher Ag content, compared to the wires in Figure 4.4 deposited at the same potentials. Figures 4.6a and 4.6c depict the wires before the nitric acid treatment. In (b) and (d) the same nanowires after the nitric acid

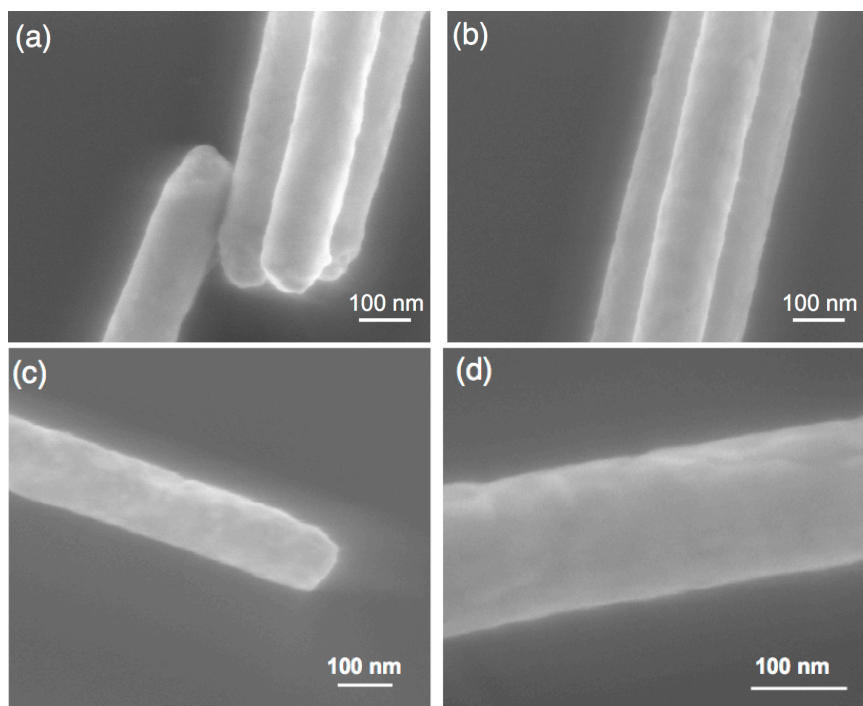


Figure 4.5: SEM images showing the surface morphology of nanowires (Au:Ag \sim 60:40) before ((a) and (b)), and after nitric acid treatment for 3h ((c) and (d)).

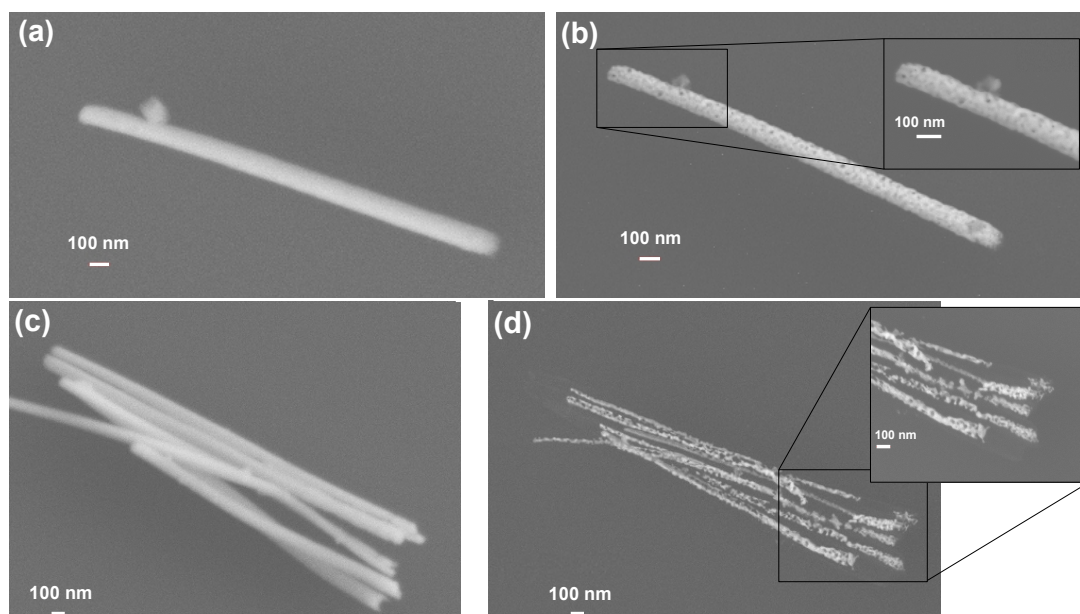


Figure 4.6: Left: SEM images of AuAg alloy nanowires (Au:Ag ratio in electrolyte 1:1), applying the voltages (a) -1.1 V and (c) -0.5 V. Right: SEM images of the identical wires as on the left after treatment with concentrated nitric acid for three hours. The insets depict parts of the porous wires with higher magnification.

treatment are shown. Porous structures were obtained in this case for both samples. In Figure 4.6b, the nanowire maintained its overall shape and diameter, but reveals almost homogeneously distributed pores. This result highlights the potential of porous wires as interesting platforms for SP investigation, due to the increased surface, and the formation of voids, being promising as Raman Hotspots.^{80,96,97} It was found that not all nanowires in one sample have similar porosity. In fact, wires with varying porosity along their surface were created. Investigation of these wires, using EDX in SEM, revealed that all wires possess a certain amount of Ag atoms, varying dependent on the porosity. For bigger pores, the Ag content was decreased, while, for small pores, the Ag content was close to the initial one of 60 %. We assume that this is linked to the hydrophobicity of the Si substrate, leading to an irregular dissolution of Ag atoms in the wires. Finally, similar results as for the sample shown in Figure 4.4d were found also for the nanowires deposited at -0.5 V. These wires are very porous structures, with diameter changes of a factor of about 3 and partly separation into segments.

4.2 Segmented nanowires and nanogaps

4.2.1 Control on segment length

Segmented nanowires were synthesized by pulsed deposition. Considering the results of the previous sections, the electrolyte containing a Au:Ag ratio of 2.5:1 was chosen. The pulsed deposition using this electrolyte resulted after nitric acid treatment in smooth Au-rich segments (deposition potential -1.1 V), while parts with high Ag content were created when switching the potential to -0.5 V.

Figure 4.7a shows two representative pulse sequences that were applied for the deposition of segmented nanowires with the same duration of the first and the third pulse, which was 25 s. The duration of the second pulse amounted to 5 s (red line) and 20 s (black line), respectively.

The corresponding current-vs-time curves are depicted in Figure 4.7b. The pore density in the template was 10^9 ions/cm² and the pore diameter amounted to about 100 nm. Both curves reveal a strong decrease in the absolute value of the current during the first 20 s after applying the voltage, which is characteristic of the nanowire growth. During the growth of cylindrical wires a constant current is typical, which could here only be measured during about the last 5 s of the first pulse. Immediately when the voltage was switched to the lower negative voltage, a current jump to a positive current was recorded. We assume that the positive current was due to a

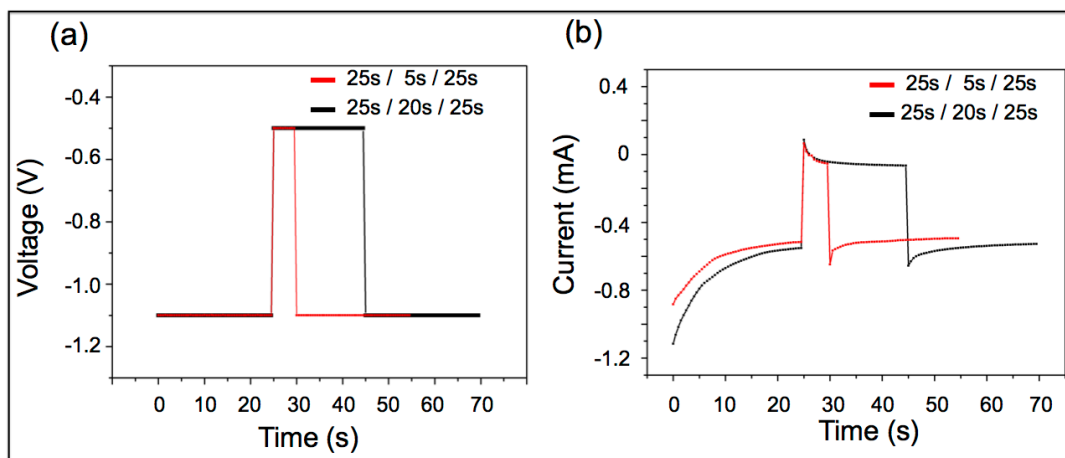


Figure 4.7: (a) Two pulse sequences applied for the electrodeposition of two arrays of segmented nanowires. The duration of the first and the third pulse was kept constant at 25 s, while the duration of the middle pulse was in the black curve 20 s and in the red curve 5 s. The corresponding current-versus-times curves recorded during the deposition of the nanowires are shown in (b). Pore density in the template was $\sim 10^9$ ions/cm² and pore diameter amounted to about 100 nm.

competition between dissolution of Au atoms and reduction of $\text{Ag}(\text{CN})_2^-$ -ions. After few seconds, the current decreased to an almost constant negative value due to the reduction mainly of $\text{Ag}(\text{CN})_2^-$ ions. When the voltage was switched back, the current jumped again to a larger negative value, and approached after few seconds an almost identical current value compared to the one during the first pulse. The slightly different current values comparing the black and the red line can be explained by slightly different fluences in the samples, varying pore filling rates and a random distribution of the pores.

The SEM images in Figure 4.8 show segmented nanowires resulting from the deposition process in Figure 4.7a. In (a) the length of the middle pulse was 20 s, while in (b) it was reduced to 5 s.

It is obvious from Figure 4.8 that with decreasing duration of the lower negative pulse the length of the corresponding middle segment decreases. However, it was found that not all segments in one array have identical size and shape. The latter is assigned to varying crystalline growth directions.

In Figure 4.9, a similar series of nanowire bundles corresponding to three different arrays is shown. Compared to Figure 4.8 the length of the pulse at -1.1 V was increased to 37 s. Figure 4.9 visualizes an increased length of the Au-rich segments compared to the one in Figure 4.8. The length of the middle pulse was varied from (a) 25 s to (b) 18 s and (c) 10 s. In Figure 4.8d, an EDX in SEM scan was performed along one of

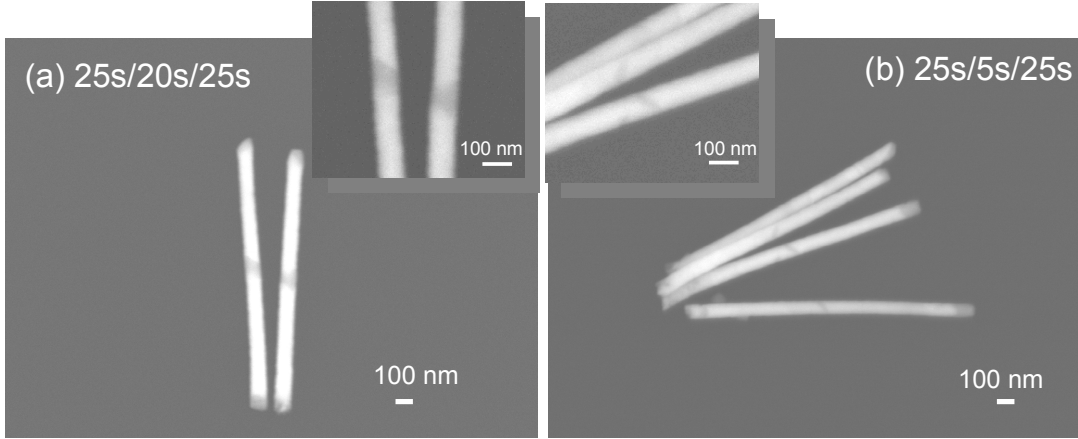


Figure 4.8: SEM images showing segmented $\text{Au}_{60}\text{Ag}_{40}/\text{Au}_{15}\text{Ag}_{85}/\text{Au}_{60}\text{Ag}_{40}$ nanowires originating from two different arrays. They were synthesized applying the two different pulse sequences in Figure 4.7. The duration of the pulse to create the middle Ag-rich segment was decreased from 20 s in (a) to 5 s in (b). The time for the deposition of Au-rich segments was constant (25 s), leading to an average length of about 730 ± 25 nm. The insets depict the darker Ag segments with higher resolution.

the nanowires, revealing the increased count rates corresponding to the Ag L_{α} peak at the position of the dark segment in the middle of the wire.

We have analysed in Figure 4.10 the length distribution of the different segments. For the short Ag-rich segments, the varying crystal orientations of the segments complicated this analysis. In spite of the resulting big measurement errors, the measured Ag-rich segment lengths versus the duration of the corresponding pulse are shown for six different samples in Figure 4.10. For each sample, 15 to 30 segments have been measured. The length of each Ag-rich segment was defined here as the shortest distance between two Au-rich segments.

Comparatively, it has been analysed only a small sample of the $\sim 10^9$ segmented nanowires that were deposited at the same time. From Figure 4.10 we conclude that with decreasing pulse duration the probability for the synthesis of a small segment increases. In addition, Figure 4.10 reveals an increasing variation in segment length with pulse duration for the given spot sample.

Regarding the Au-rich segments, Figures 4.8 and 4.9 demonstrate that although the first and the third pulse had the same duration, usually the length of the two resulting Au-rich segments was not identical. The histogram in Figure 4.11 shows for 59 nanowires the number of wires versus the ratio between the two lengths L_1 and L_2 of the two Au-rich segments corresponding to one wire. L_1 is defined as the longer segment in a specific wire, while due to the random distribution of nanowires on the

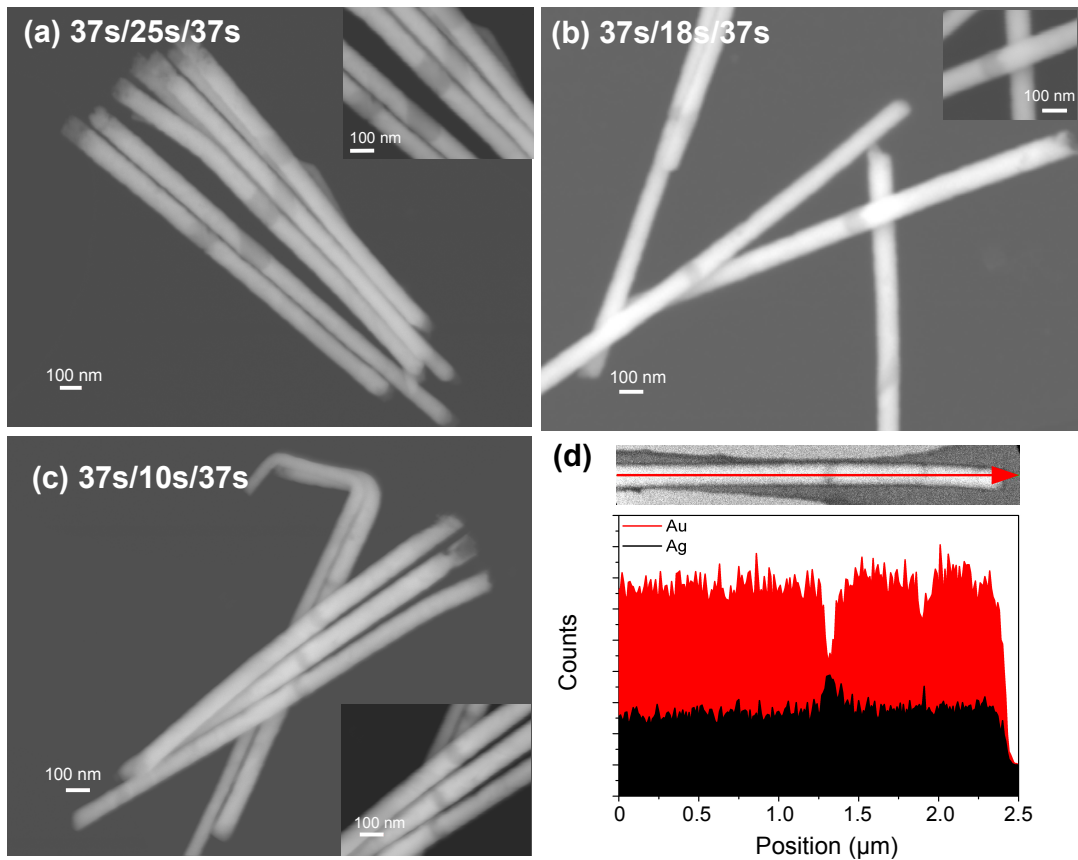


Figure 4.9: SEM images of $\text{Au}_{60}\text{Ag}_{40}/\text{Au}_{15}\text{Ag}_{85}/\text{Au}_{60}\text{Ag}_{40}$ nanowires similar to Figure 4.8. This time, the average length of the Au-rich segments is increased to about 1050 ± 25 nm by applying a pulse of 37 s. The length of the middle pulse is decreased from 25 s (a) to 18 s (b) and 10 s (c). The inset depicts the Ag-rich segments with higher resolution. In (d) an EDX scan along the length of one of the nanowires is shown. The red line depicts the count numbers measured for the Au M_{α} -peak, while the black line indicates the count numbers along the wire for the Ag L_{α} -peak.

Si substrate it was not possible to determine whether the longer segment corresponds to the segment deposited at first or third place. The pulse duration was 25 s.

Obviously, the majority of wires in the spot sample of 32% corresponds to a length ratio between 1.1 – 1.2. Two segments with almost identical length, belonging to the interval 1.0 – 1.1, were found with a smaller probability of 24%. Furthermore, Figure 4.11 shows that creating nanowires with ratio higher than 1.4 is very unlikely for two pulses with same duration.

In addition, pulse deposition enables also the growth of Au-rich segments with different preselected lengths separated by the Ag-rich segment. Exemplarily, Figure 4.12a shows a pulse sequence consisting of three different pulses. A first pulse at -1.1 V

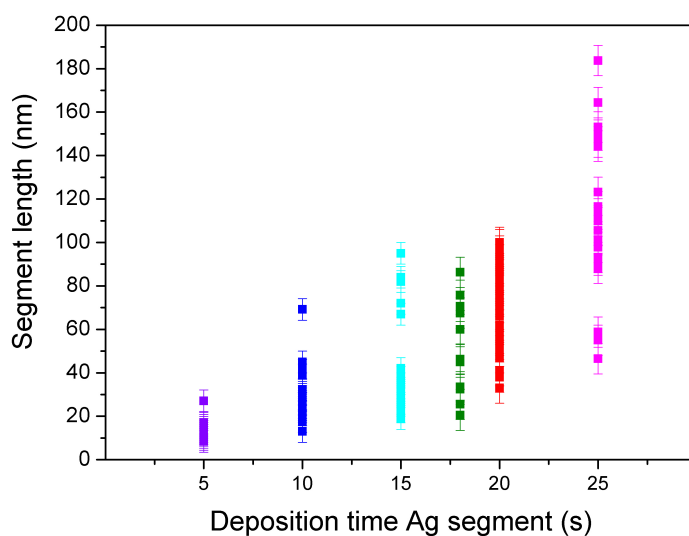


Figure 4.10: Lengths of Ag-rich segments in $\text{Au}_{60}\text{Ag}_{40}/\text{Au}_{15}\text{Ag}_{85}/\text{Au}_{60}\text{Ag}_{40}$ nanowires as a function of duration of the middle pulse. Each data point represents the length of a different segment in the sample.

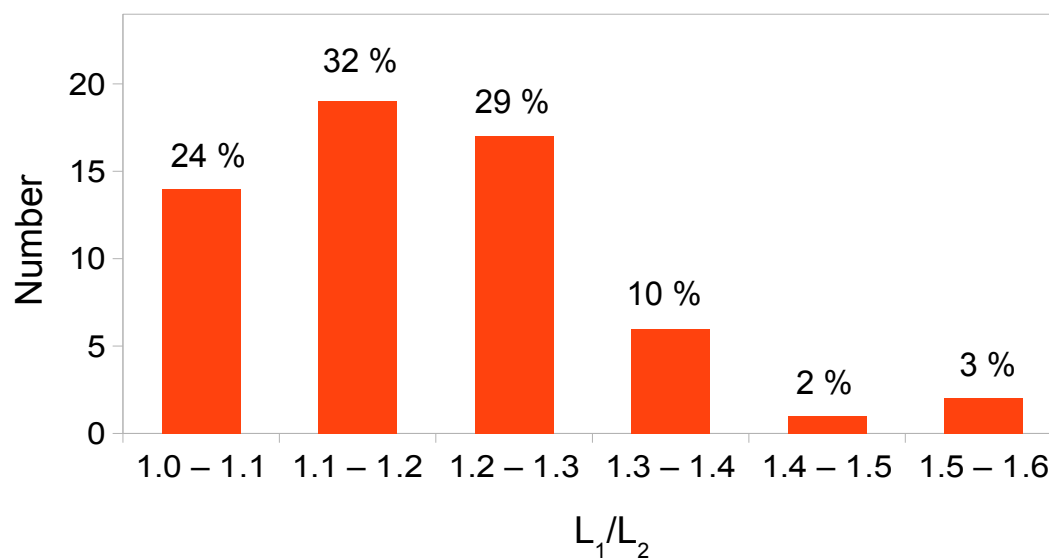


Figure 4.11: Number of segmented nanowires versus the ratio between L_1 and L_2 , being the length of the two Au-rich segments for a sample of 59 nanowires. The ratio L_1/L_2 is separated into 6 different intervals.

of 30 s, a middle pulse at -0.5 V of 15 s, and a final pulse at -1.1 V of 60 s. A SEM image of a nanowire created with this sequence is shown in Figure 4.12b. The two different pulse durations of the first and third pulse lead to two different segment lengths of

about 870 and 1500 nm, resulting in a length ratio of 1.72. The Ag-rich segment was already etched away, as described in the following section, and a nanogap was created.

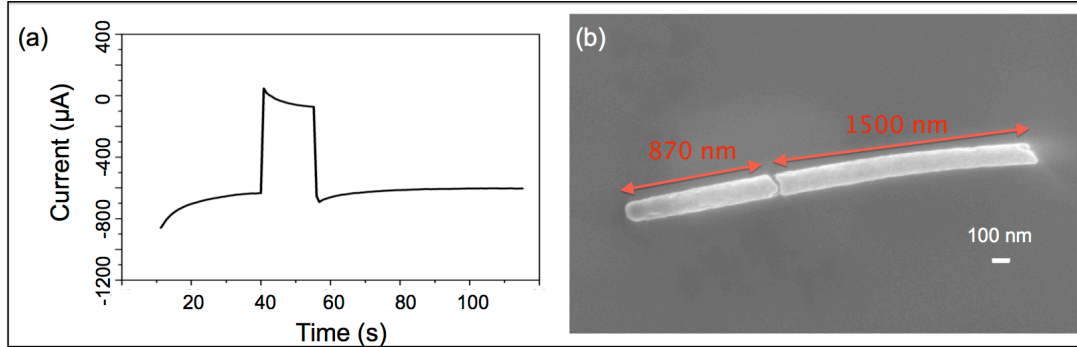


Figure 4.12: (a) Pulse sequence consisting of a pulse at -1.1 V of 30 s, a middle pulse at -0.5 V of 15 s, and a final pulse at -1.1 V of 60 s. The wire is depicted after etching the middle Ag-rich segment using nitric acid in (b).

Similar to the investigation of the Ag-rich segments, we have analysed for the Au-rich segments the dependency between pulse duration and segment length. The two histograms in Figure 4.13 demonstrate for the different pulse lengths ((a) 25 s and (b) 37 s) the distribution of the resulting segment lengths. It presents the number of segments versus their length. The segment length was divided into intervals. Each interval includes segments with a length given by the value indicated on the x-axis ± 25 nm. For all wires, the lengths of the shorter and the longer segments corresponding to a wire are treated separately. The distribution of the shorter Au-rich wires is depicted by red bars, while the one of the longer segments is given by the blue bars.

In spite of the broad distribution, the shift to longer segments is obvious for the pulse duration of 37 s compared to the pulse duration of 25 s. Considering all the segments measured in the array with pulse duration 37 s an average segment length of 1050 ± 25 nm was found, while when applying a pulse of only 25 s an average segment length of only 730 ± 25 nm was obtained.

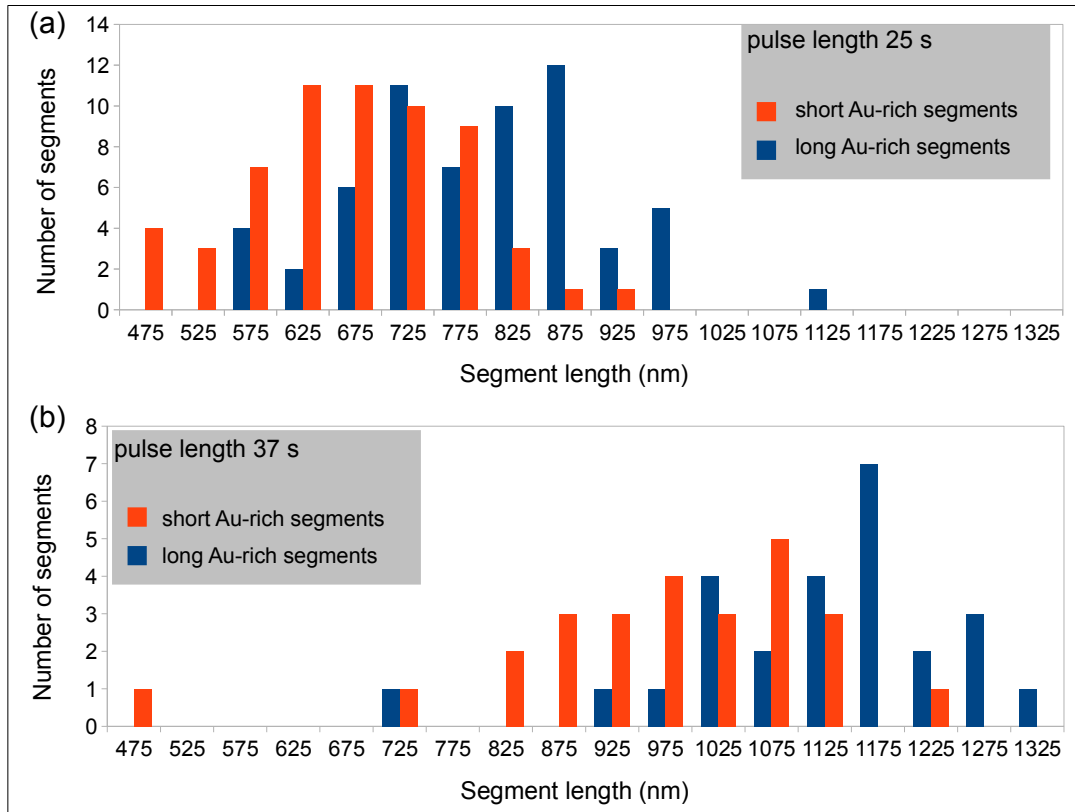


Figure 4.13: Number of segments versus segment length measured in an array. Each bar corresponds to an interval including segments with length of the value on the x -axis ± 25 nm. In (a) the pulse duration for the Au-rich segments was 25 s, while in (b) the pulse duration was 37 s. Each segmented wire consists of two Au-rich segments slightly deviating in their length. The red bars depict the length distribution of the shorter segments, and the blue bar the one of the longer segments.

4.2.2 Formation of nanogaps by dealloying

Nanogaps, separating two nanowires, were prepared by dissolving the Ag-rich segments in the nanowires by treatment with concentrated nitric acid. The obtained structures are so-called capacitively coupled nanowire dimers. The substrate with the segmented nanowires was dipped for three hours into the acid, following the same protocol as described in Section 4.1.2. Figure 4.14 displays SEM images of the same two wires (a) before and (b) after the nitric acid treatment. The wires consist of chains of six Au-rich and six Ag-rich segments deposited by switching the voltage between -1.1 V for 25 s and -0.5 V for 15 s. The insets show segments of the wires with higher resolution.

Comparing Figures 4.14a and 4.14b reveals that exactly at the position of the Ag-rich parts the material is dissolved, as expected. However, only two of the ten

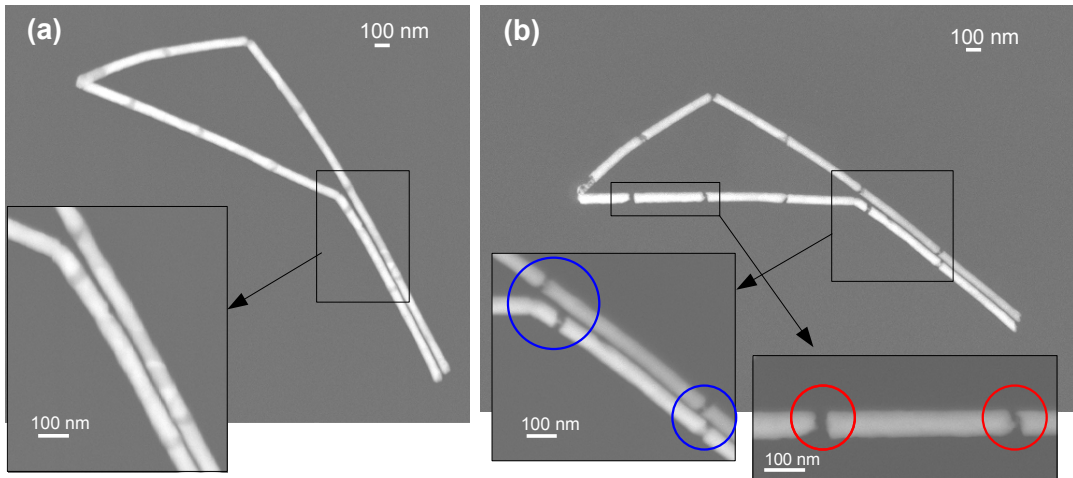


Figure 4.14: (a) Nanowires consisting of six Au-rich and six Ag-rich segments deposited by switching the voltage between -1.1 V for 25 s and -0.5 V for 15 s. (b) The same segmented nanowires as shown in (a) but after treatment with nitric acid for 3 h. The insets depict parts of the wires with higher magnification. In the insets in (b) red circles mark gaps and blue circles mark small connections between segments.

Ag-rich segments were completely dissolved and form a nanogap (marked by red circles in inset). For the others, small metal junctions connect the adjacent segments (marked by blue circles in inset). In many cases, it is difficult to decide if a gap is created, or if a metal bridge exists. This is due to a limited resolution of the microscope and small residuals of polymer in the surroundings of a wire. The analysis in Section 4.1.1 revealed that the deposition conditions, applied for the Ag-rich segment, lead to a Au:Ag ratio of about 15:85. The presence of the small connections is thus attributed to the 15 % Au atoms in the segments. These small metal connections enable charge transfer between the two wires upon the excitation of SP resonances and thus modify the plasmonic properties. As will be discussed in Section 9.3, such structures are referred to as conductively coupled nanowire dimers. However, due to the big amount of nanowires that can be synthesized at the same time with the electrodeposition method, numerous gaps were created in one sample. Striking is the fact that the nanowires were not washed away and even did not move during the nitric acid treatment. Any step fixing the wires on the substrate is avoided in this process. The method presented here enables thus the synthesis of nanowires perfectly in a row aligned and separated by small gaps.

Exemplary, Figure 4.15 shows two of the smallest created gaps with sizes between ~ 5 and 10 nm. The gap in Figure 4.15a was monitored by TEM, while the one in Figure 4.15b was imaged by STEM in SEM. Both nanogaps have been created when

applying a pulse sequence with middle pulse of 10 s.

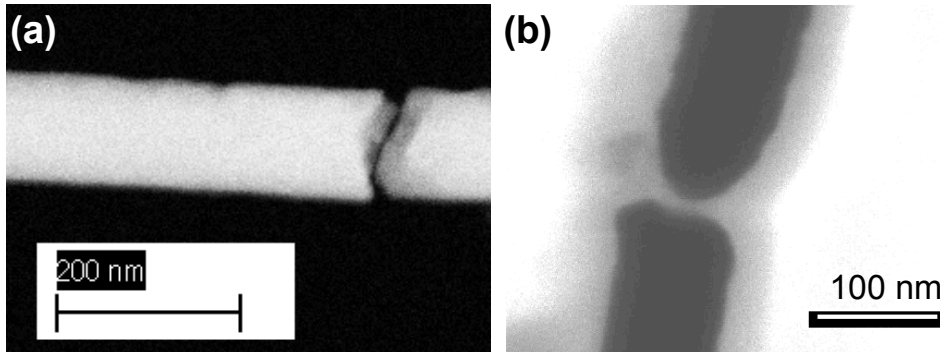


Figure 4.15: Exemplarily, images of nanowires separated by very small gaps with sizes between 5 and 10 nm. The length of the corresponding pulse in the applied sequence was 10 s.

EDX in SEM measurements of Au-rich segments were performed before and after nitric acid treatment to estimate if the Ag content changes. The measurement took place on a Si_3N_4 membrane in the STEM mode of the SEM. Figure 4.16 shows a detail of two typical spectra. The black line corresponds to a spectrum of a Au-rich segment before nitric acid treatment, while the green line depicts a spectrum of a wire after nitric acid treatment for 3 h. The background was subtracted and the spectra were normalized to the height of the Au M_{α} -peak. Both spectra reveal the same height of the peaks within their experimental errors. A ratio of Au and Ag atoms of about 60:40 was determined for both cases. If there is a difference in Ag-concentration of the wire before and after nitric acid treatment, it is too small to be measured with EDX in SEM.

Finally, we have analysed how the etching time influences the morphology of the Au-rich segments and nanogaps. A Si substrate with segmented nanowires was dipped in nitric acid for three different time periods. After each time period the same bundle of nanowires was monitored by SEM.

Figure 4.17a shows a SEM overview obtained after 1.5 hours in nitric acid. After SEM investigation, the sample was dipped again in the acid for 1.5 hours. Figure 4.17b displays the same area afterwards, *i.e.* after 3 hours in nitric acid. It is obvious that the wires did not move, exactly the identical structures could be imaged. The Figures 4.17c-e visualize the area marked in Figures 4.17a and 4.17b after 1.5 h, 3 h and 6 h, respectively. For the group of nanowire segments, no influence with increasing etching time on nanowire shape, morphology and gap size is visible. We conclude thus that for time periods from 1.5 to 6 h the time seems not to be a crucial parameter.

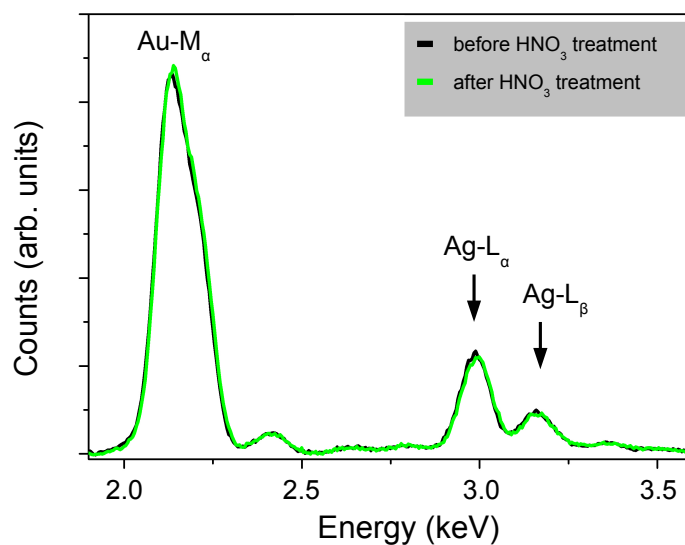


Figure 4.16: EDX in SEM of Au-rich segments before nitric acid treatment (black line) and after etching of the Ag-segments (green line). The spectra were normalized to the height of the Au M_{α} -peak.

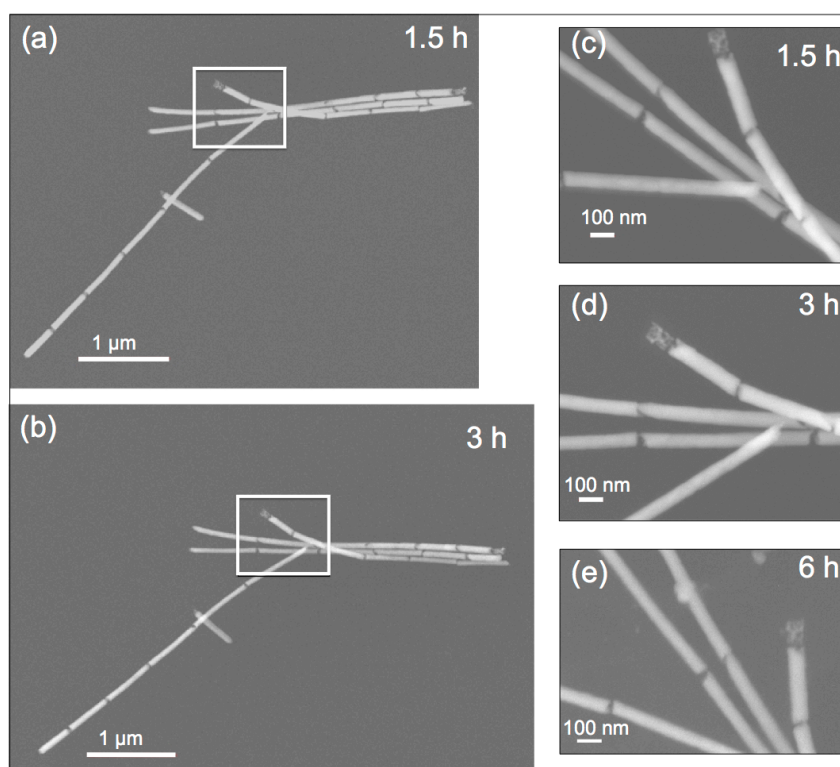


Figure 4.17: SEM images presenting segmented nanowires after etching periods of (a) 1.5 h and (b) 3 h. In (c)-(e) the marked area in (a) and (b) is visualized with higher resolution after (c) 1.5 h, (d) 3 h, and (e) 6 h etching.

4.2.3 Influence of annealing

It has been investigated how the formation of nanogaps and their morphology are affected by annealing. For this, segmented nanowires were placed on Si substrates and dipped for 3 hours in nitric acid. Then the sample was annealed at 300 °C for 30 min with a heating rate of 9 °C/min. After cooling down of the oven the nanowires were imaged again by SEM.

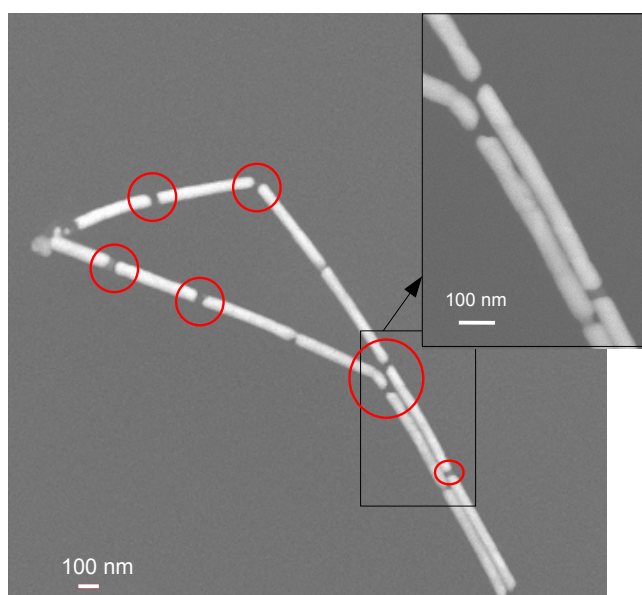


Figure 4.18: The same nanowires, as shown in Figures 4.14, but this time the wires were annealed at 300 °C for 30 min after the nitric acid treatment. The inset shows a detail with higher magnification.

Figure 4.18 depicts the same nanowires as in Figure 4.14 but this time after the annealing process. It is visible that in this case seven of the ten middle segments were completely removed and nanogaps have been created (marked by red circles). The image reveals that the shapes of the gaps compared to the ones of the initial silver segments have been modified. The ends of the Au-rich segments have been rounded compared to the unheated segments and the size of the gaps has been increased. The rounding of the nanowire ends and removal of small bridges can be explained by enhanced surface diffusion, as previously shown during the decay of Cu and Au nanowires.^{98,99} It has been demonstrated that Cu and Au nanowires start to transform from cylindrical nanowires into spheres while annealing them at temperatures far below their melting temperatures. The enhanced surface diffusion is caused by a lower surface energy of a perfect sphere compared to a cylindrical nanowire with the same volume. The diffusion process, in the case of the continuous nanowires, starts

with the formation of waist-like diameter reductions, followed by a decay into smaller segments. Further annealing finally leads to the transformation of each segment into a sphere. It has been additionally shown that the transformation temperature decreases with decreasing nanowire diameter. These results suggest that in the case of the nanogaps, removal of the small bridges and rounding of the nanowires ends are due to the same process. The low temperature of 300 °C and the short annealing time of 30 min were chosen to avoid a complete transformation of the short Au-rich segments into nanospheres.

Finally, EDX analysis was performed for these nanowires in the SEM and compared to the spectra obtained before the annealing process. We found that after the annealing process the Ag concentration was decreased by about 5%. This surprising observation was confirmed for different samples and nanowires. It is most probably due to the differences in the intrinsic diffusion coefficients of Au and Ag. Future investigations will be devoted to study this effect.

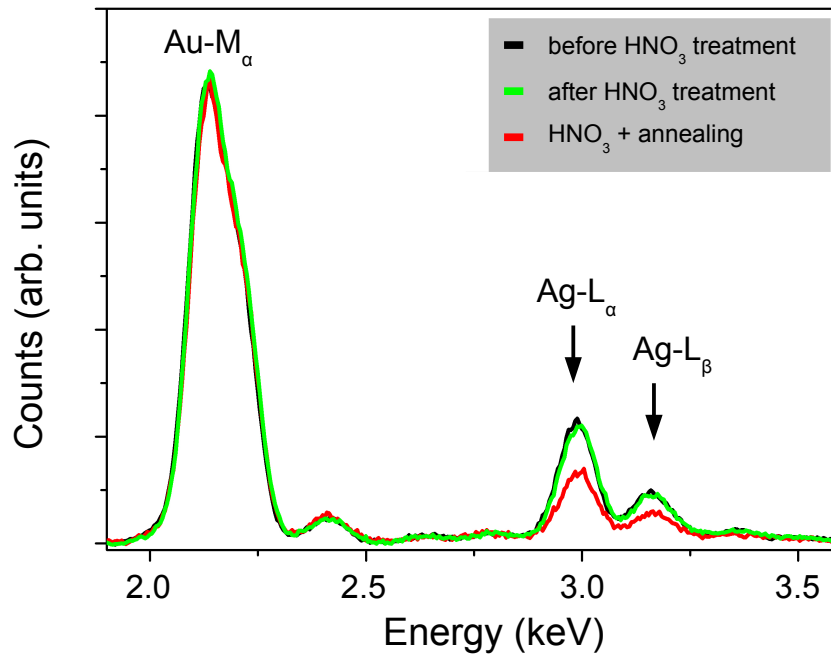


Figure 4.19: Details from EDX spectra of segmented nanowires before dissolving the Ag-rich segment (black), after nitric acid treatment (green), and after nitric acid treatment and annealing at 300 °C for 30 min (red).

Chapter 5

Conclusions

The experiments described in Chapter 4 demonstrate that nanogaps as small as 5 nm can be prepared by electrodeposition of segmented Au-rich/Ag-rich/Au-rich nanowires combined with subsequent etching of the middle segment.

The segmented wires were prepared by pulsed deposition using an electrolyte containing $\text{Au}(\text{CN})_2^-$ - and $\text{Ag}(\text{CN})_2^-$ -ions. The length of the segments was controlled by varying the length of the corresponding pulses. We observed that not all segments in one sample have identical shape and length. However, a clear trend for the preparation of shorter segments by applying pulses with shorter durations was found. Ag-rich segments with lengths between 5 and 185 nm were obtained by varying the pulse length between 5 and 25 s. It was furthermore found that the obtained segments are not pure but contain a certain amount of the second metal. This Au:Ag ratio was tuned by varying the electrolyte concentrations and the deposition potentials.

For the preparation of the nanogaps, we used $\text{Au}_{60}\text{Ag}_{40}/\text{Au}_{15}\text{Ag}_{85}/\text{Au}_{60}\text{Ag}_{40}$ nanowires. Our investigation of the synthesis process has revealed that treatment of these wires with nitric acid leads to the formation of gaps and at the same time unporous Au-rich segments. EDX in SEM analysis demonstrated that the Au:Ag content in the Au-rich segments remains unchanged after the nitric acid treatment. The nanogaps perfectly adopt the shape and size of the Ag-rich segments in the wires. However, not all Ag-rich segments were completely dissolved. Some of them form small metallic connections between two wires. This has been attributed to the 15% percent Au atoms in the Ag-rich parts.

Finally, we have analysed how annealing influences the morphology of the Au-rich segments and the gaps. Annealing increased the probability that a gap without a conducting connection was formed, but also modified the gap shape. A rounding of the nanowire edges and an increase in the size of the gaps have been assigned to

enhanced surface diffusion.

Since electrodeposition is a synthesis method with a high-throughput and of extremely low-cost these results demonstrate that pulsed deposition of segmented nanowires combined with etching of the middle segment is efficient for the fabrication of nanowires separated by small gaps with controlled dimensions. Especially the very small gaps of about 5 nm are promising for applications since it is known that by excitation of SPs an extremely high field enhancement is generated at the position of the gap for such small gaps. It is of tremendous advantage to be able to control the parameters of the dimer, such as the dimensions and the gap size. This allows the adjustment of the SP resonance frequency (see Section 9.1). It was additionally shown here that no special preparation step is necessary in order to attach the nanowires to the substrate. Such a step may lead to a decreased field enhancement when exciting SPs. Since Au and Ag feature similar plasmonic properties, having their plasma frequencies in the visible range, residuals of Ag in the Au-rich segments modify the plasmonic properties only slightly (see Section 8.2).

Part II

Surface plasmons in individual nanowires and dimers

Chapter 6

Surface plasmons in individual nanostructures

Over the past few decades, SP resonances in nanostructures have been intensively studied, the main reason being the high field enhancement generated at their surface and the enhanced scattering and absorption cross sections. The following chapter introduces the basic concepts of SP excitation in nanostructures. In Section 6.1, we present the optical properties of Au and Ag determined from their dielectric functions. The dielectric function describes the response upon the influence of an incoming electric field depending on its frequency. For spherical particles, the plasmonic properties can be derived from the quasi-static approximation presented in Section 6.2. The plasmonic properties of single nanowires and coupled systems are summarized in Sections 6.3 and 6.4, respectively. In these cases the quasi-static approximation cannot be applied for the determination of the resonance energy, due to retardation effects.

6.1 Optical properties of Au and Ag

The response of a metal exposed to electromagnetic radiation depends strongly on the excitation frequency and is characterized by the complex dielectric function $\varepsilon(\omega) = \varepsilon_1(\omega) + i\varepsilon_2(\omega)$, relating the incoming electric field $E(\omega)$ and the material polarization $P(\omega)$. More detailed analysis can be found in many electrodynamics textbooks (*e.g.* Ref. 100). Here, we focus on aspects that are crucial for the analysis of the optical properties of metallic nanostructures.

At low frequencies, noble metals can be regarded as nearly perfect conductors and their response is described applying the Drude-Sommerfeld theory. Drude assumed that the electrons oscillate in the metal driven by the applied electromagnetic field, and their motion is damped via collisions. The movement of the electrons can be thus

described via a harmonic oscillator. The resulting dielectric function is

$$\varepsilon(\omega) = 1 - \frac{\omega_p^2}{\omega^2 + i\gamma\omega}, \quad (6.1)$$

ω_p being the plasma frequency of the free electron gas and γ the collision frequency. Typical parameters for Au are $\omega_p \simeq 13.8 \times 10^{15} \text{ s}^{-1}$ and $\gamma \simeq 1.07 \times 10^{14} \text{ s}^{-1}$.¹⁰¹

Important conclusions from the Drude-Sommerfeld model are a negative dielectric real part and a significant imaginary part, resulting in an out-of-phase oscillation of the electronic motion and the external field.

This model describes the response of a metal to an external electric field very well up to frequencies where interband transitions become possible for the electrons. Interband transitions strongly alter the dielectric function obtained from the Drude-Sommerfeld model and lead to an increase of its imaginary part and thus increased damping at these frequencies. Figure 6.1 shows the real and imaginary part of the dielectric functions of Au and Ag.¹⁰² While, for the real part of ε , Au and Ag reveal a good agreement, their imaginary parts deviate especially at energies higher than 2.1 eV, where the intraband transitions in Au become possible. For Ag, intraband transitions lead to an increase of the imaginary part starting at 3.8 eV. This difference between Au and Ag is caused by relativistic effects. While the non-relativistic band structures of Au and Ag are very similar, relativistic effects, being much higher in the higher Z material Au than in Ag, shift the band structure and thus the energy necessary for interband transitions. This is also the reason for the yellowish appearance of Au bulk material, compared to the greyish brilliance of Ag.¹⁰³

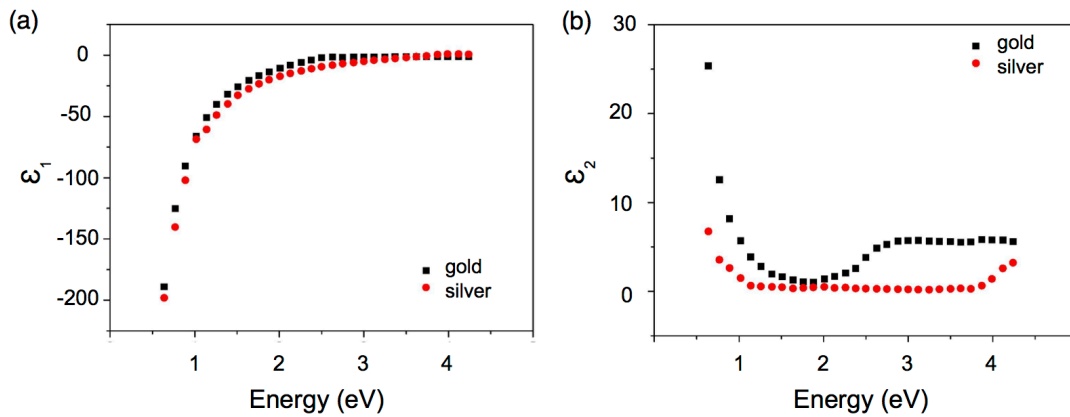


Figure 6.1: (a) Real part ε_1 and (b) imaginary part ε_2 of the dielectric function of Au (black squares) and Ag (red dots). The data are taken from Ref. 102.

Most of the optical properties of noble metallic nanostructures of sizes as small as $\sim 10 \text{ nm}$ can be well described within classical electrodynamics. The high density of

free charge carriers leads to minute spacing of energy levels, being smaller than the thermal excitation energy $k_B T$ at room temperature.

6.2 Plasmonic properties of nanospheres

SPs are resonant collective oscillations of the conduction electrons at the surface of a metallic-dielectric interface. In the case of nanoparticles, these oscillations are bound to the particle surface and are termed localized SP resonances. In contrast to SP polaritons that travel on a planar metal-dielectric interface, localized SP resonances arise from the interference of back and forward travelling electronic waves at the surface of the particle, in analogy to a standing wave in a resonator.

The source of the oscillation is an electromagnetic wave with the specific resonance frequency, while the restoring force is given by the ionic background. The plasmonic properties of the particle at the resonance are characterized by an increased electric field in the near-field of the particle, and enhanced absorption and scattering cross-sections in the far-field.

For small particles, that have a diameter $d \ll \lambda$, the SP resonances can be derived using the quasi-static approximation. In this case, the phase of the electric field is approximately constant along the surface of a nanoparticle. The electric field surrounding the small particle can in this approach be derived from the solution of the Laplace equation for the potential $\nabla^2 \Phi = 0$, where $E = -\nabla \Phi$. A complete discussion of this problem can be found in electrodynamic textbooks. The derivation leads to a polarizability of the particle that is given by

$$\alpha = 4\pi a^3 \frac{\varepsilon - \varepsilon_m}{\varepsilon + 2\varepsilon_m}, \quad (6.2)$$

where ε_m is the dielectric constant of the surrounding medium, and a denotes the radius of the particle. The resonance condition is found if the denominator has a minimum, which means that

$$\text{Re}[\varepsilon(\omega)] = -2\varepsilon_m. \quad (6.3)$$

This shows that the resonance frequency of the particle is not only determined by the dielectric function of the material but also by the dielectric function of the surrounding medium. If the diameter of the particle increases, the quasi-static approximation cannot be applied and retardation effects have to be taken into account, since the phase of the external electric field varies along the surface of the particle. The onset of retardation effects is the reason for changes in the spectral position of the resonance,

of its width, its near-field intensity and extinction cross-section, as will be discussed in more detail in the following.

Very recently, some authors started the challenge of exploring nanoparticles even smaller than 10 nm. Experimentally and theoretically, the authors report a blueshift of the SP resonances of these structures that can not be explained classically. Taking into account quantum mechanics, SPs can no longer be associated with collective electronic oscillations, but must be described with quantum electron transitions between occupied and unoccupied energy levels. The authors attribute the blue shift of a resonance with decreasing particle size to the increasing separation of the discrete energy levels with decreasing particle diameter.^{104,105}

6.3 Plasmonic properties of single nanowires

If the relation between the dimensions of a nanoparticle and the wavelength increases, the plasmonic properties of the particle cannot be derived using the quasi-static approximation. A derivation of the excited electric fields in this case was published by Mie in 1908,¹⁰⁶ and is known as the Mie-Theory.

Altering the nanoparticle geometry from a sphere to an elongated nanorod or wire introduces an additional degree of freedom, when determining the SP resonance frequency: Due to the two different axis lengths of the wire, the resonance splits into two branches, a longitudinal mode representing an oscillation along the length of the wire, and a transverse mode corresponding to an oscillation in the direction perpendicular to it.¹⁰⁷ In particular, the longitudinal SP resonance is of interest for many applications, since it is adjustable over a wide frequency range (visible to middle infrared) by varying the nanowire dimensions and generates high electric fields localized at the nanowire ends.

To give an overview of the plasmonic properties of nanowires, important results of recent publications are summarized here. For more detailed overviews, the reader is referred to review articles on SP resonances in nanowires.^{108–110} Figure 6.2 shows the far-field and near-field spectra of nanorods of varying length between 200 and 500 nm, the rod diameter is 80 nm. The spectra were calculated with the boundary element method (BEM),^{111,112} assuming a nanorod with hemispherical shaped ends. The nanorod is exposed to electromagnetic radiation with polarisation in longitudinal direction. Figure 6.2 reveals a redshift of the longitudinal resonance for both the far-field and the near-field with increasing nanowire length L . The length increase leads to charge separations over larger distances than for smaller particles, reducing the restoring force and hence resulting in a lower resonance frequency, equivalent to

a longer resonance wavelength.³⁰ In addition, the intensity of the peak increases with L , due to the growing dipole strength. In the insets the far- and near-fields of a sphere with varying diameter are shown.

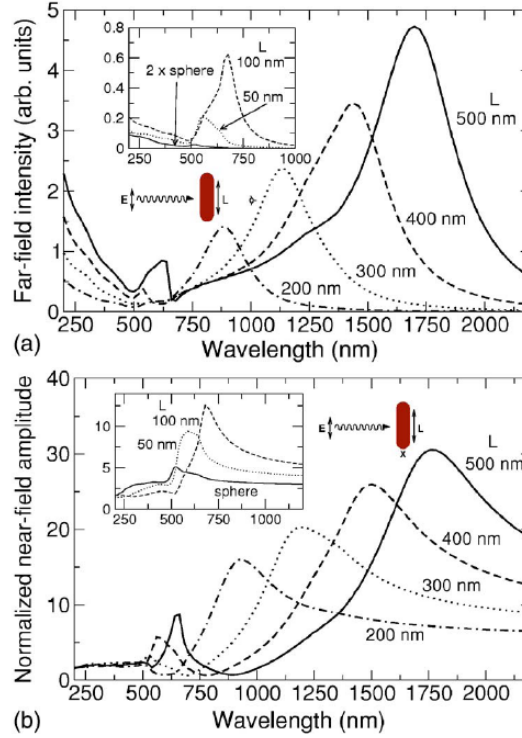


Figure 6.2: (a) Far-field intensity as a function of excitation wavelength measured for Au nanorods with varying length between 200 nm and 500 nm. The polarisation of the electric field of the incoming wave is in the longitudinal direction. (b) Near-field intensity for the same nanorods as in (a). The near-field intensity is calculated for the position marked with the small x. Reprinted with permission from Ref. 30 (DOI). Copyright 2005 by the American Physical Society.

As indicated in Figure 6.2, the near-field response is shifted to the red compared to the far-field response. This is characteristic of the onset of retardation effects that originate from varying phases of the external electric field along the nanowire surface. This shift between near- and far-fields can be understood in analogy to a damped harmonic oscillator, where the driving frequency, leading to the highest amplitude, is shifted to the red with respect to the eigenfrequency of the oscillator by an amount that depends on the damping of the oscillation.¹¹³

Due to the nonzero penetration depth of electromagnetic radiation into the metal at optical frequencies, the rod diameter also influences the SP resonance energies. While for rod diameters below the skin depth of the metal, the resonance frequency

is only determined by the length of the nanowire, in the case of bigger diameters the resonance shifts to the blue with increasing diameter for a fixed length. In Figure 6.3 the influence of the diameter is depicted. The figure shows the far-field resonance wavelength of Au wires versus the aspect ratio for different nanowire diameters R , resulting from BEM calculations.

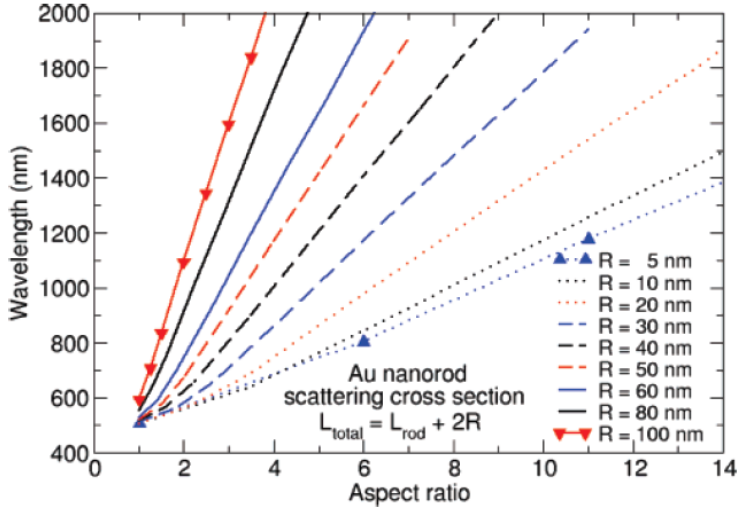


Figure 6.3: Far-field wavelength of the longitudinal dipole resonance as a function of the nanowire aspect ratio. The different curves correspond to different nanowire radii R . Reprinted with permission from Ref. 27 (DOI). Copyright 2008 American Chemical Society.

Figure 6.2 reveals additional peaks for the long nanowires at short wavelengths. These peaks are attributed to multipole SP resonances. For a given external excitation, the induced surface charge σ is expressed as a summation of the SP modes. Thus, σ is given by

$$\sigma = \sum_{l,m} A_{l,m} \sigma_m^l e^{im\phi}, \quad (6.4)$$

l being the mode order and m the azimuthal index. A_{lm} is the weight of the multipole order modes σ_m^l depending on the characteristics of the incoming beam, the material and the geometry. Figure 6.4 presents the lowest-order SP modes for $m = 0$, which are the longitudinal oscillations. Only antisymmetrical modes that possess a net dipole moment are efficiently excitable by incoming light, and are thus denoted as bright modes. These modes are characterized by an even number of maxima along the wire. In Figure 6.4, these modes are indicated by the numbers 1, 3, 5, 9 and 19. The symmetrical modes without net dipole moment are known as dark modes. They have an odd number of maxima and are denoted by the numbers 0, 2 and 4 in Figure 6.4. The mode labelled with the number 1 (σ_0^1) is the dipole longitudinal SP resonance. It

is, due to its high dipole moment, most easily resolvable in a spectrum and interesting for many applications.

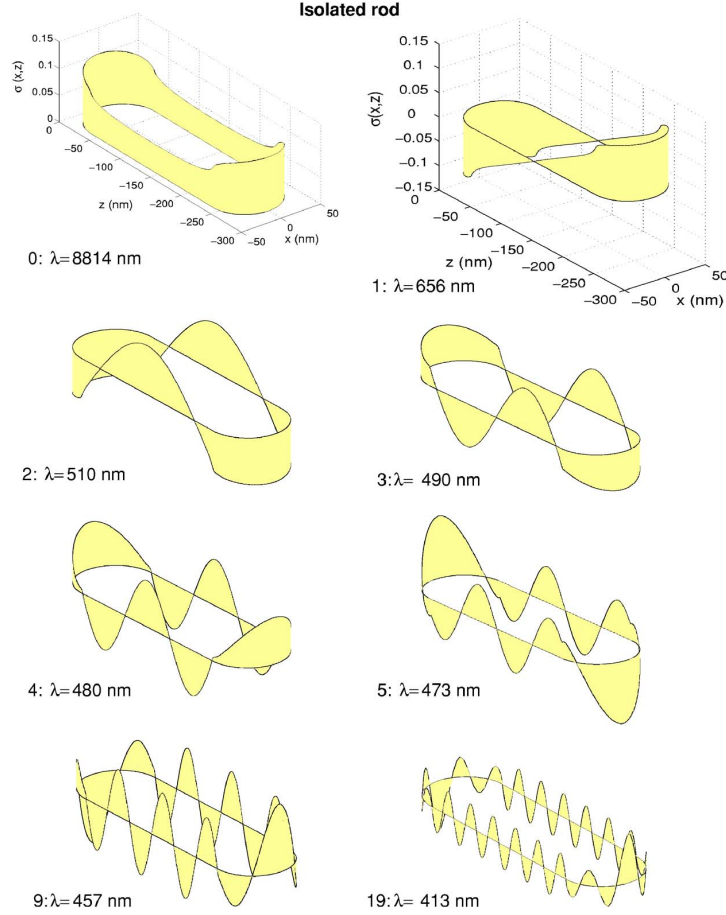


Figure 6.4: Surface charge distribution for several of the low-order longitudinal ($m = 0$) SP modes. The wire shown here has a length $L = 200$ nm and a diameter $D = 40$ nm. Reprinted with permission from Ref. 30 (DOI). Copyright 2005 by the American Physical Society.

Theoretical analysis of the excitation of multipole order resonances revealed that the multipole resonance wavelengths depend also on the nanowire shape and dimensions.^{25,26} As for the dipole mode, the resonance wavelengths of the multipole modes are shifted to longer wavelengths with increasing nanowire length. This can be explained by similar arguments as for the dipole mode. If the nanowire length increases, the distance between two electric field maxima increases, resulting in a lower restoring force.

In addition to the shifts of the resonance wavelength depending on geometry and dimensions of the nanowire, the polarizability of the surrounding medium also influences the resonance wavelength. This dependency suggests that the plasmonic

properties of nanowires can be used in sensorics. Figure 6.5 shows theoretical results on elliptical nanowires embedded in different media. The resonance wavelength shifts for several multipole modes (l) with increasing refractive index of the medium (n_m) to longer wavelengths are depicted.

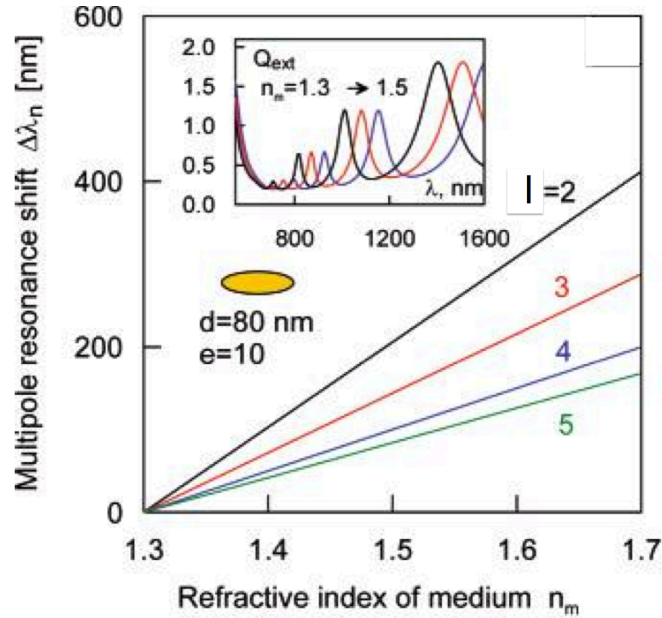


Figure 6.5: Resonance shift of different multipole modes l versus the refractive index of the medium n_m for an elliptical particle. The inset shows the far-field spectra for three different refractive indices of the medium. Adapted with permission from Ref. 25 (DOI). Copyright 2007 American Chemical Society.

Experimentally, the higher-order multipole modes are, due to their lower intensity, difficult to access and thus much less studied than the dipolar longitudinal mode. Especially in the far-field, these modes are difficult to resolve due to the rising background caused by interband damping. Investigations of these modes in more detail, applying near-field techniques, have begun only recently. Figures 6.6a and 6.6b show experimental results of multipole modes using scanning near-field optical microscopy (SNOM)¹¹⁴ and EELS-STEM.⁴⁶ In Figure 6.6a, Dorfmueller et al. demonstrated the excitation of the bright and dark modes in nanowires using SNOM. The nanowires were excited at a constant wavelength of 942 nm. With varying nanowire length different multipole modes were excited using this wavelength. The figure reveals for $l = 1, 3,$ and 5 the calculated field magnitude, and the measured magnitude and phase. The authors showed also that symmetry-forbidden modes without net dipole moment can be excited by changing the angle between the incoming beam and the wire. The near-field maxima along the nanowire are interpreted as standing-wave patterns of the SP

wave. In analogy to a one-dimensional Fabry-Pérot resonator the SP wavelength is given by

$$\lambda_{SP} = \frac{2}{l - \frac{\delta\Phi}{\pi}} \cdot L. \quad (6.5)$$

L is the length of the nanowire, l the multipole order and $\delta\Phi$ represents a phase jump upon reflection at the nanowire ends.¹¹⁵ Similar results with even higher spatial resolution of few nanometres can be obtained using EELS in a TEM. In Figure 6.6b, the SP resonances were excited by the fast travelling electron beam in a TEM. The energy loss of the electrons was analysed in an electron spectrometer to resolve the energies of high loss probability, being the resonance energies (*cf.* Section 7.1). In Figure 6.6b, the electron beam was scanned along a single Ag nanowire, each vertical line in the map represents one spectrum, the color indicates the loss probability, as indicated by the scale bar. Instead of the resonance wavelength, here the resonance energies of the excitation source are given. The intensity maxima along the nanowire at specific energies can be as well interpreted as the standing-wave patterns of the SP wave, as it will be discussed in Section 7.1.

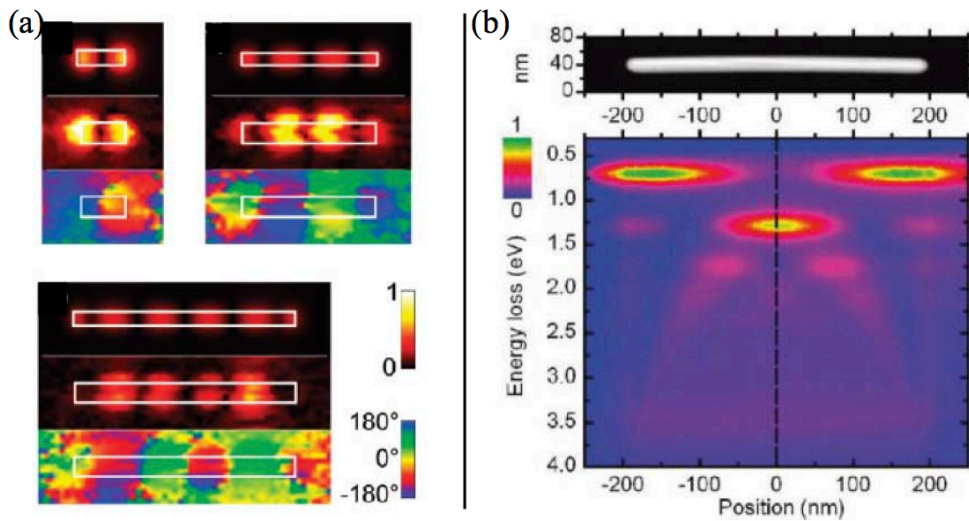


Figure 6.6: a) SNOM measurements and calculations of the $l = 1, 3,$ and 5 multipole order modes excited in nanowires with different lengths for a fixed excitation wavelength. The images show from top to bottom the calculated near-field magnitude, the measured magnitude and the phase. Reprinted with permission from Ref. 114 (DOI). Copyright 2009 American Chemical Society. b) EELS map along a single Ag nanowire. Each vertical line corresponds to one spectrum measured at a specific point along the nanowire. The color indicates the loss probability. Reprinted with permission from Ref. 46 (DOI). Copyright 2011 American Chemical Society.

6.4 Plasmonic properties of coupled systems

Recently, coupling of SP resonances in structures consisting of several nanoparticles has attracted strong interest. Such structures have the potential to provide even higher electric field enhancement than the corresponding single structures. In analogy to the formation of molecular orbitals by mutual interaction of atoms, Nordlander et al. introduced a theory to describe the coupling of SP resonances of such closely spaced particles, called hybridization theory.^{116,117} It is well-established to call such structures, in the case of two particles, nanoparticle dimers, again in analogy to molecular orbitals. The structures are divided into homodimers, consisting of equal particles separated by a gap, and heterodimers, consisting of two particles differing in material or dimensions.¹¹⁷

The hybridisation theory considers the electrons as an incompressible liquid, while the ions are represented as positive charge n_0 , uniformly distributed within the particle. The interaction potential between the SP modes is calculated using a Coulomb potential, and retardation effects are neglected. The SPs are then modelled as deformations of the incompressible electron liquid, resulting in the formation of surface charges σ :

$$\sigma(\Omega, t) = n_0 e \sum_{l,m} \sqrt{\frac{l}{R^3}} S_{lm} Y_{l,m}(\Omega), \quad (6.6)$$

$Y_{l,m}(\Omega)$ being the spherical harmonics of the solid angle Ω , S_{lm} the deformation amplitudes, and R is the radius of the particle. The SP resonance energies are then found by solving the Euler-Lagrange equation. Detailed derivations of this theory can be found in Refs. 116, 117.

Figure 6.7 demonstrates schematically the hybridisation of the SP modes in a nanowire homodimer for the lowest-order mode. The intrinsic SP modes of two individual nanowires interact, resulting in a degeneracy of the modes. For small gap sizes, the modes do not only interact with modes of the same multipole order l , but also with modes of different order. This leads to further red shifts of the resonance energies. Modes that have positive and negative surface charge maxima at opposite sides of the gap are denoted as bonding modes. The antibonding modes are characterized by surface charge maxima of the same sign at both gap ends.

Figure 6.8 shows the result of the hybridisation theory for two nanowires separated by a small gap. The rods are aligned in axially symmetric configuration (*cf.* Figure 6.7). In the figure, D is the gap width for (a) $m = 0$ (longitudinal modes) and (b) $m = 1$ (transversal modes). For $m = 0$, the bonding modes reveal a red-shift with

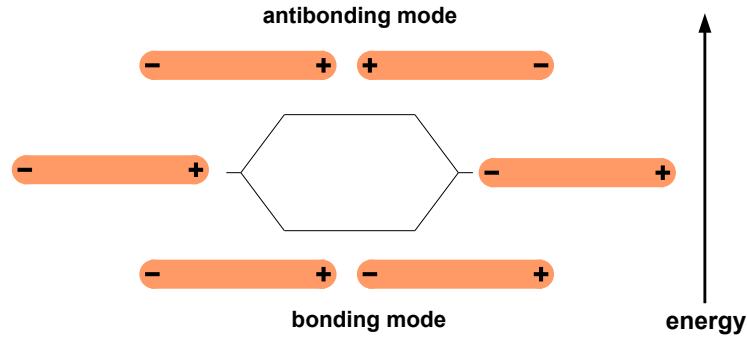


Figure 6.7: Schematic illustration of the hybridisation of the SP modes of two closely spaced nanowires. The SP modes of the two individual nanowires couple, resulting in the splitting into bonding and antibonding dimer modes.

decreasing gap size, while the antibonding modes are slightly shifted to the blue, resulting in an increasing energy difference between bonding and antibonding modes for each multipole order with decreasing gap size. The redshift of the bonding modes is due to the attraction between positive and negative surface charges across the gap, and thus a lowering of the restoring force. In contrast, in the antibonding modes, repulsion of surface charges across the gap increases the restoring force, leading to the blueshift. Bonding and antibonding dimer modes for $m = 1$ resulting from the coupling of the transverse modes of the two individual structures are shown schematically in Figure 6.8b.

The resonances of single nanostructures (dimensions ≥ 10 nm) as mentioned in Section 6.1 can be calculated classically. In the case of the nanogaps, the dimensions become even smaller, raising the question if coupling of nanostructures can be as well treated classically. For nanospheres, quantum-mechanical calculations have shown that three different regimes of interaction can be identified.¹¹⁸ In the classical regime, separation distances are bigger than about 1 nm. These distances are large enough that electron tunnelling between the two spheres can be neglected. The interaction can be well described by the above presented hybridisation theory, resulting in an increasing redshift of the bonding mode with decreasing gap size. Gap sizes between 1 and 0.5 nm are denoted as the crossover regime. These distances are small enough that electrons tunnel with significant probability between the two spheres. The charge transfer between the two particles reduces the coupling strength and the bonding modes are less shifted to the red. This regime can no longer be treated classically. Finally, distances smaller than 0.5 nm belong to the conductance regime. Here conductance between the two particles is large. A charge transfer mode appears at long wavelengths

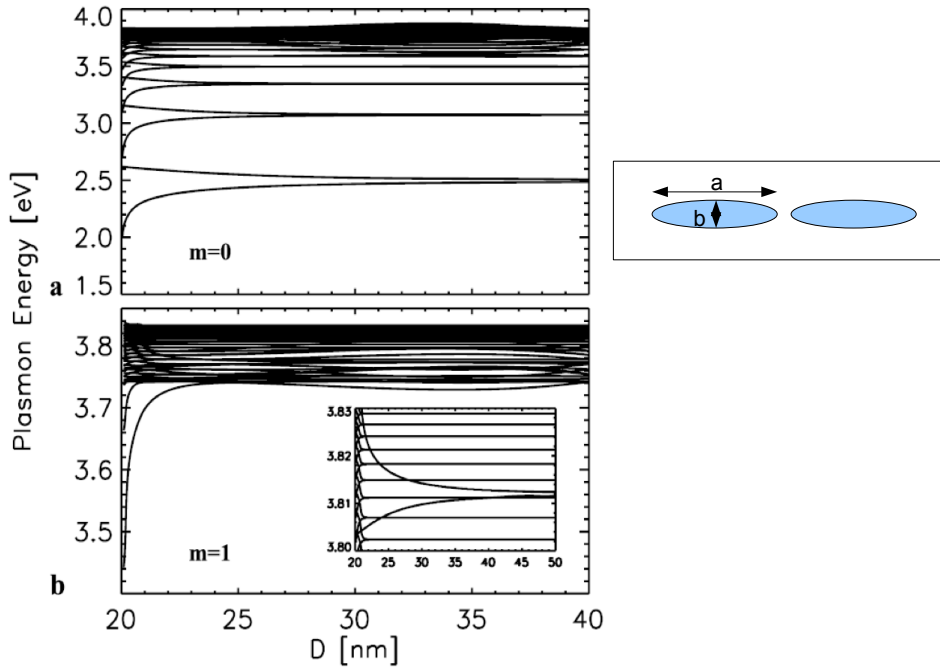


Figure 6.8: Calculated longitudinal ($m = 0$) and transverse ($m = 1$) resonance energies as a function of gap width D between two prolate Ag nanorods with major radius $a = 10$ nm and minor radius $b = 3$ nm. The rods are aligned in axially symmetric configuration as shown schematically on the right of the figure. Reprinted with kind permission from Springer Science and Business Media³¹ (DOI).

and the bonding mode shifts further to the blue. Figure 6.9 illustrates the situation in the three cases. The curve shows the potential barrier that the electrons have to overcome when crossing the gap between the two spheres. The red line marks the Fermi level. From left to right the gap size decreases, decreasing the potential barrier compared to the Fermi level. Below, the electron density along the dimer is presented.

In the conductance regime, gap sizes can be reduced until the particles overlap. Theoretically, it has been shown that with increasing overlap the charge transfer mode and the dipole bonding mode shift further to the blue.^{119,120}

Turning back to the classical regime, Figure 6.10 shows experimentally obtained results on dimer structures, revealing splitting into bonding and antibonding modes for the lowest multipole order. Since for the dipole modes the antibonding mode is a dark mode and thus not efficiently accessible using light microscopy techniques, the splitting into bonding and antibonding modes is studied using EELS in a TEM. The figure shows results from very recent publications.^{32,33} In Figure 6.10a, two silver nanoparticles are separated by a dielectric shell. EEL spectra are measured at the positions of the red circles in the TEM image. In Figure 6.10b, the dimer consists

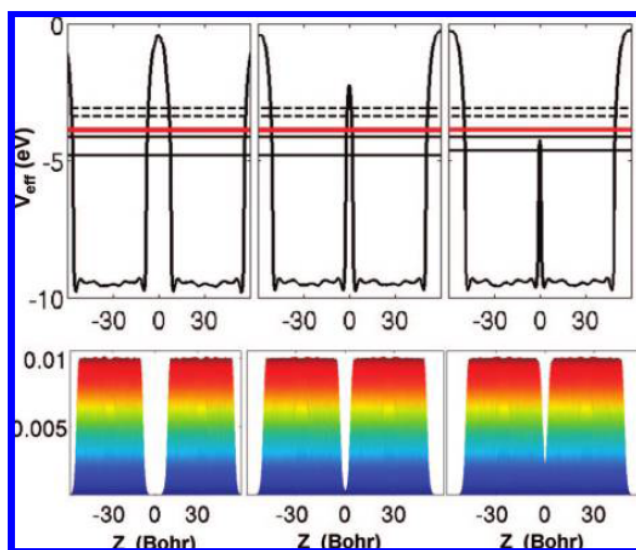


Figure 6.9: Top: Potential barrier along a dimer that the electrons have to overcome in the three different regimes (classical, crossover and conductance regime) discussed in the text. The red line depicts the Fermi level. Bottom: Electron density along the structure. Reprinted with permission from Ref. 118 (DOI). Copyright 2009 American Chemical Society.

of two Au nanorods separated by a gap of about 8 nm, and two EEL spectra are measured at one end of the dimer structure (red line) and at the position of the gap (blue line). The spectra of both structures reveal the splitting into a bonding and an antibonding mode, where the bonding mode is the lower energy mode. It is visible that the bonding mode is not excitable at the position of the gap, due to symmetry reasons. In Figure 6.10a, the bonding mode is present at about 2.2 eV while the antibonding mode is visible at about 3.3 eV. In Figure 6.10b, the bonding mode is excited at 1.55 eV and the antibonding mode at 1.82 eV. At 2.38 eV additionally the transversal mode is resolvable. In the spectra of both publications, the two modes are very difficult to distinguish due to their low intensity, their proximity and broad FWHM. Multipole modes are not visible.

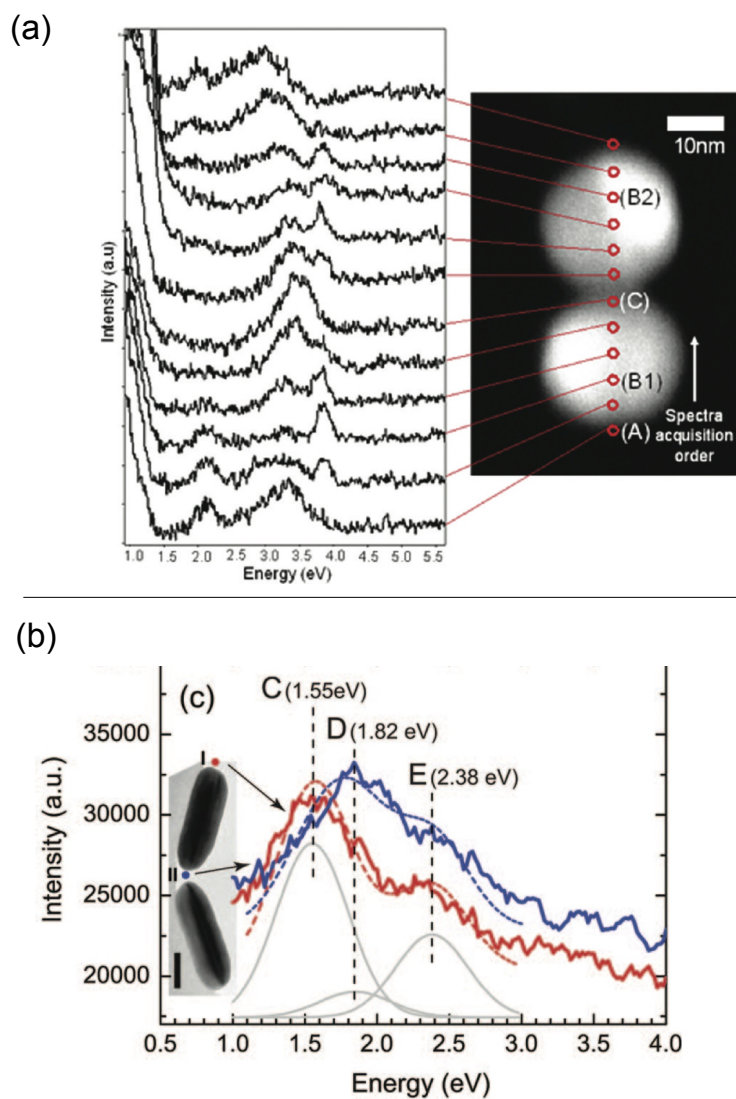


Figure 6.10: (a) EEL spectra measured along two Ag nanoparticles separated by a dielectric shell. Reprinted with permission from Ref. 32 (DOI). Copyright 2009 American Chemical Society. (b) EEL spectra of a nanorod dimer, measured at one end of the dimer (red line) and at the position of the gap (blue line). Adapted with permission from Ref. 33 (DOI). Copyright 2008 American Chemical Society.

Chapter 7

Methods

7.1 Electron energy loss spectroscopy

EELS in a TEM is a commonly applied method for material characterization of very thin samples. The principle can be described in brief as follows: Electrons transmitted through a sample in the microscope enter an electron spectrometer where they are deflected by magnetic lenses depending on their remaining energy. The resulting spectra offer information about the electronic band structure and the chemical identity of the sample. Due to the pioneering work of Pines and Bohm in 1952¹²¹ and Ritchie in 1957,¹²² it has been discovered that, in addition, the low loss region of the spectra reveal the SP excitations in the material.

F. J. Garcia de Abajo derived in 1999 an analytical solution of the energy loss suffered by a fast electron passing near a nanoparticle when exciting SP resonances.³⁵ This energy loss can be derived from the induced field that is set up by the electron and depends on the geometry of the nanoparticle. The relation between the induced field and the energy loss ΔE of the electron is given by:

$$\Delta E = e \int dt \mathbf{v} \cdot \mathbf{E}_{\text{ind}}[\mathbf{r}_e(t), t] = \int_0^{\infty} \hbar \omega d\omega \Gamma_{\text{EELS}}(\omega) \quad (7.1)$$

with

$$\Gamma_{\text{EELS}}(\omega) = \frac{e}{\pi \hbar \omega} \int dt \text{Re}\{e^{-i\omega t} \mathbf{v} \cdot \mathbf{E}_{\text{ind}}[\mathbf{r}_e(t), \omega]\}. \quad (7.2)$$

$\Gamma_{\text{EELS}}(\omega)$ is the electron-loss probability, \mathbf{E}_{ind} is the induced electric field, v is the electron velocity, e is the electron charge and \hbar the Planck constant. Equation 7.1 shows that the loss probability depends only on the induced electric field component in the direction of the electron beam velocity, which is in the following denoted as

the z -component. This implicates that the EELS method does not offer valuable information on the strength of the field enhancement in the gap and at the nanowire ends. This high field enhancement, that is beneficial for SERS and SEIRS, is due to the electric field in the direction of the longitudinal nanowire axis, which is not monitored by STEM-EELS. However, the method offers crucial information on the z -component with resolution of few nanometres, and allows the determination of the resonance energies of multipole modes precisely.

The STEM-EELS measurements reported here have been carried out at the SESAM transmission electron microscope (TEM) (Zeiss, Oberkochen) at the Max Planck Institute for Intelligent Systems in Stuttgart. Here, in brief, the main features of this microscope that allow SP investigation of nanostructures using EELS are summarized. For more detailed information see for example Refs. 123,124.

A cold field emitter serves as the electron source. This electron source is characterized by a low energy spread (0.3-0.5 eV). The emission current is lower than in a lanthanum hexaboride (LaB_6) source, but the smaller emission angle leads to an increased brightness, which results in a high counting statistics but small beam spot and enables thus measurements with very high spatial resolution of few nanometres. Investigating the SP resonances of nanowires that are located at infrared frequencies necessitates an even better monochromated beam than achievable only with the field emission gun. This is ensured by a monochromator. Different types are available. In the SESAM an electrostatic omega filter leads to an energy resolution (width of the zero loss peak) of 0.1 eV at an emission current of several 100 pA. However, for the here reported measurements the width was slightly increased to about 0.12 eV to increase the electron probe current and thus the counting rates. In all spectra, the zero-loss peak was subtracted by fitting a power law function to the positive energy loss tail of this peak using the Gatan Software Digital Micrograph.

The investigated nanostructures were in all cases transferred onto a Si_3N_4 membrane of 30 nm thickness. The electron beam passed the sample at a distance of 10-20 nm to the nanowire surface. It is as well possible to excite the SP when the electron beam passes the nanowire, however in this case, many electrons are elastically scattered and do not enter the electron spectrometer, leading to low counting statistics. The energy loss probability at a given energy loss is found to decay exponentially with increasing distance to the nanowire surface.

Finally, the energy loss probability depends on the electric field induced at the specific resonance energy, but also on the electron velocity and thus the acceleration voltage in the TEM as visible in Equation 7.2. The relative intensity of low-order

modes compared to modes of higher order is increased with increasing acceleration voltage. In the here presented measurements the operation voltage was 200 kV.

Figure 7.1a shows schematically the experimental arrangement in the TEM. The electron beam passes the Si_3N_4 membrane at a certain distance to the nanowire surface and its energy loss is afterwards analysed in the spectrometer. The electron beam is scanned along the nanowire in the direction of the dashed line. In Figure 7.1b, the electron spectrometer is shown schematically. Magnetic lenses deflect the electrons depending on their remaining energy, forming a spectrum at the position of the dispersive plane.

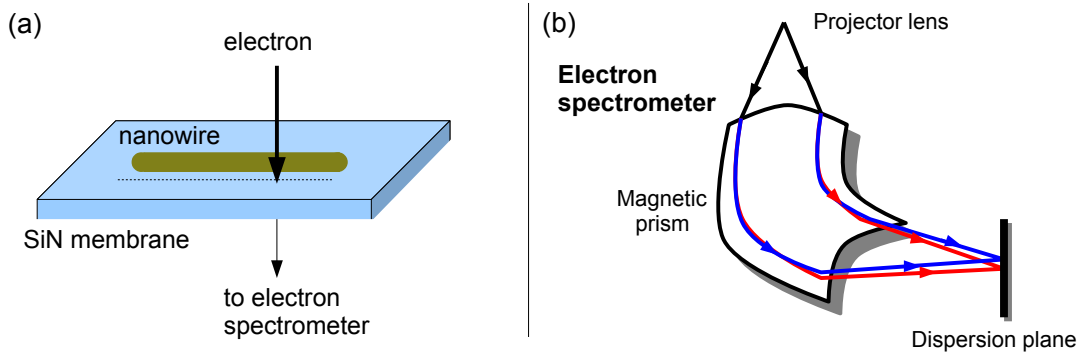


Figure 7.1: (a) Scheme of the set-up in a TEM for EELS measurements. (b) Energy filter in the TEM. An energy loss spectrum of electrons transmitted through the sample at specific positions is obtained at the dispersion plane, since electrons are deflected in the magnetic lenses depending on their remaining energy.

7.2 Finite integration simulation

Simulations of the electric fields, excited in the proximity of the nanowires by electromagnetic radiation, were performed using the commercially available program Computer Simulation Technology (CST) Microwave Studio¹. The program is based on the finite integration method solving numerically Maxwell's equations in their integral form. In the applied module, Maxwell's equations are solved in the frequency domain for an adaptively chosen frequency sample. The structure and the background material are composed of tetrahedral mesh cells. The mesh resolution is varied along the structures dependent on the structure curvature (see Figure 7.2). Further, an automatic mesh adaption routine refines the mesh by introducing new mesh points on the surface to reduce geometry errors. Perfect matched layers (pml) were used as boundary conditions. Pml are designed to almost totally absorb propagating electromagnetic waves, and thus avoid difficulties associated with reflection of waves at the simulation cell boundaries.

The electric field source is a dipole with impedance $10\text{ k}\Omega$ ($5\text{ k}\Omega$ in Section 9.3). The dipole is centered on the longitudinal axis of the nanostructure and is as well polarized in this direction. The distance from one nanostructure end is 10 nm (see Figure 7.2B). Excitation by the dipole enables the analysis of the resonance energies of both bright and dark modes. The dielectric function of Au is taken from Ref. 125.

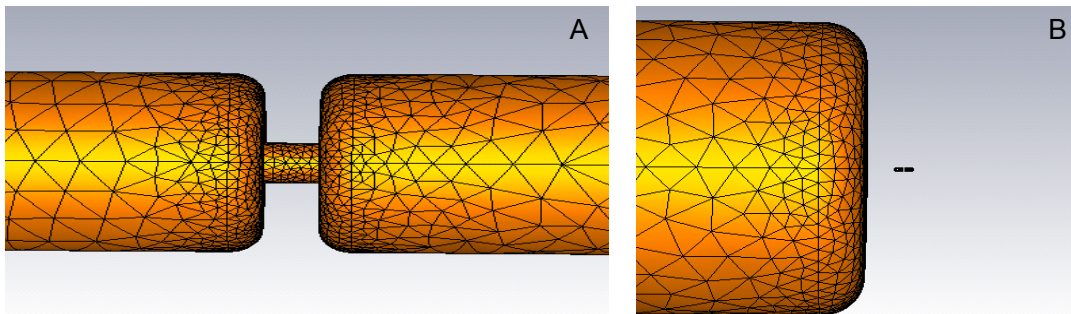


Figure 7.2: A: Structure composed of tetrahedral mesh cells for finite integration simulation with CST Microwave Studio. The number of mesh cells depends on the size and the curvature of the structure. B: Dipole located at 10 nm distance from a nanowire end, being the excitation source for the CST Microwave Studio calculations presented in this work.

¹CST Microwave Studio, www.cst.de

Chapter 8

Multipole surface plasmons in nanowires analysed by EELS-STEM

In this chapter, we present results on the investigation on the SP resonances of individual nanowires that were performed by means of EELS-STEM. The results are partly published in Ref. 48¹.

In Section 8.1, the study on pure Au nanowires with varying aspect ratio is displayed and the results are compared to finite element simulations using CST Microwave Studio. Au nanowires are theoretically and experimentally intensively investigated structures, and the analysis can thus be used to verify previously reported results on the influence of the nanowire dimensions and compare experiment and simulation. For Au wires with length in the μm -range, also multipole modes up to the order of five are included in this analysis.

Section 8.2 presents the near-field investigation of multipole modes of the AuAg nanostructures by EELS-STEM. In this section measurements on nanowires of smooth and porous contours will be also discussed. CST simulations were performed to interpret the experimental results, for which near-field studies are still scarce. The final Section 8.3 compares the dispersion relations of these structures that can exclusively be obtained from the EELS-STEM measurements.

¹Reproduced with permission. Copyright American Chemical Society 2011

8.1 Influence of nanowire dimensions

Figure 8.1a shows a high-resolution plasmonic energy loss map obtained by acquisition of 100 electron energy loss (EEL) spectra at equispaced positions along the long axis of a Au nanowire with length $L = 895 \pm 5$ nm and diameter $D = 95 \pm 5$ nm. The nanowire was deposited from an electrolyte containing 50 mM $\text{KAu}(\text{CN})_2$, applying a potential of -1.1 V. The spectra were acquired from top to bottom as indicated by the red arrow in the TEM image of the wire. The average distance of the scan line to the nanowire is ~ 10 nm. From left to right, the energy loss increases from 0.3 to 2.7 eV. The color scale indicates the number of counts, representing the probability for electron-SP inelastic scattering and results in a spatial representation of the SP modes resolved at different energy losses.

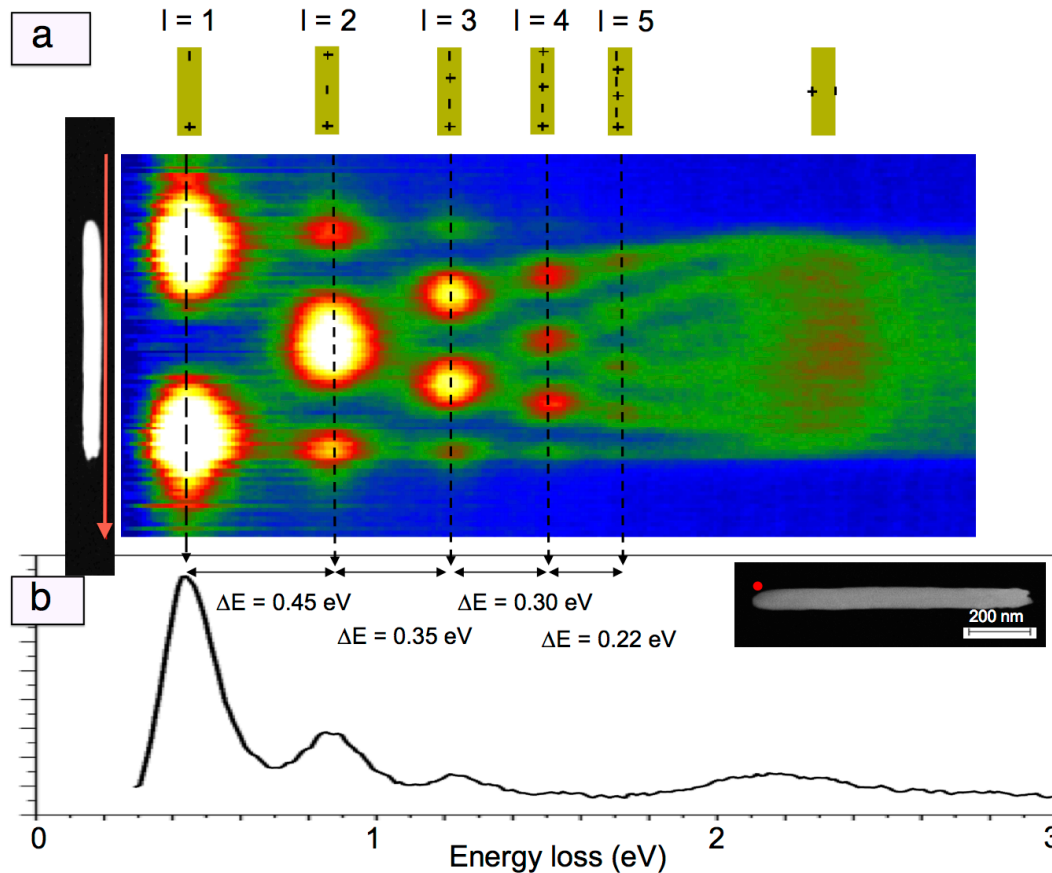


Figure 8.1: (a) High-resolution plasmonic field intensity map consisting of 100 EEL spectra measured along the long axis of a nanowire in the direction of the red arrow on the left. The energy interval, plotted from left to right, ranges from 0.3 to 2.7 eV. The color indicates the number of counts. (b) Electron energy loss spectrum (EELS) measured at one end of the single nanowire. The inset shows a TEM image of the single nanowire corresponding to the spectrum. The red dot marks the position of measurement.

As explained in Section 7.1, the intensity maxima in the map indicate positions of high electric field in the direction of the velocity of the electron beam (z -direction). The maxima are thus interpreted as standing wave patterns like in a Fabry-Pérot resonator (see Equation 6.5). In analogy to the Fabry-Pérot resonator, the resonance energies are assigned to different longitudinal multipole SP modes by counting the number of intensity maxima along the scan line at the specific energy. The multipole order of the mode is specified by the integer l , where $l = 1$ denotes the dipole mode, having two maxima, one at each nanowire end. In Figure 8.1, five multipole order longitudinal modes are distinguishable in this way. On top of Figure 8.1a the electric field distribution along the wire for these five modes is schematically represented. An additional mode is visible in the map, which is excitable when positioning the electron beam at any point along the scan line parallel to the long axis of the nanowire (red arrow), but decays rapidly beyond the wire ends. Its energy, centered at $E_T \sim 2.3$ eV is in reasonable agreement with previously reported energy values of the transversal SP resonance in Au nanorods, namely 2.4 and 2.5 eV.^{42,43} The small energy deviation can be explained by the different wire diameters, the aspect ratio, and the different substrates.¹²⁶

Figure 8.1b shows exemplarily a single spectrum of the mapping in Figure 8.1a, recorded at one side-end of the nanowire (red dot in inset). The spectrum reveals as energy loss peaks at least the first four SP modes at 0.43 ± 0.01 , 0.87 ± 0.01 , 1.22 ± 0.01 , and 1.51 ± 0.01 eV, also visualized in the mapping in Figure 8.1a. At the end of the nanowire the transversal peak at 2.3 eV is not excited. However, at this position the peak reveals a redshift to ~ 2.15 eV. This can be observed at both nanowire ends. A possible explanation for this is the excitation of different multipole transversal modes due to the shape of the wire ends.

Figures 8.1a and 8.1b evidence that with increasing l the intensity of the peaks decreases, as it was shown in previous publications for Ag nanowires.⁴⁷ Small intensity deviations between two maxima of the same multipole order at the two wire ends are assigned to varying nanowire end shapes and thus deviations in the distance between scanline and nanowire surface.

The energy difference ΔE , determined from Figure 8.1a and given in Figure 8.1b, specifies the distance between two consecutive longitudinal modes. Noticeably, with increasing energy loss, ΔE decreases from $\Delta E = 0.45 \pm 0.02$ eV for the difference between the $l = 1$ and 2 modes to $\Delta E = 0.22 \pm 0.03$ eV for the difference between the $l = 4$ and 5 modes.

This observation is displayed for different Au nanowires with varying aspect ratios

in Figure 8.2. The figure presents the SP energies of longitudinal modes for three nanowires. The energy is plotted versus the multipole order l . Only modes whose energies range in an interval between 0.4 and 2.0 eV are depicted, since this interval is experimentally accessible with small determination errors. The red dots correspond

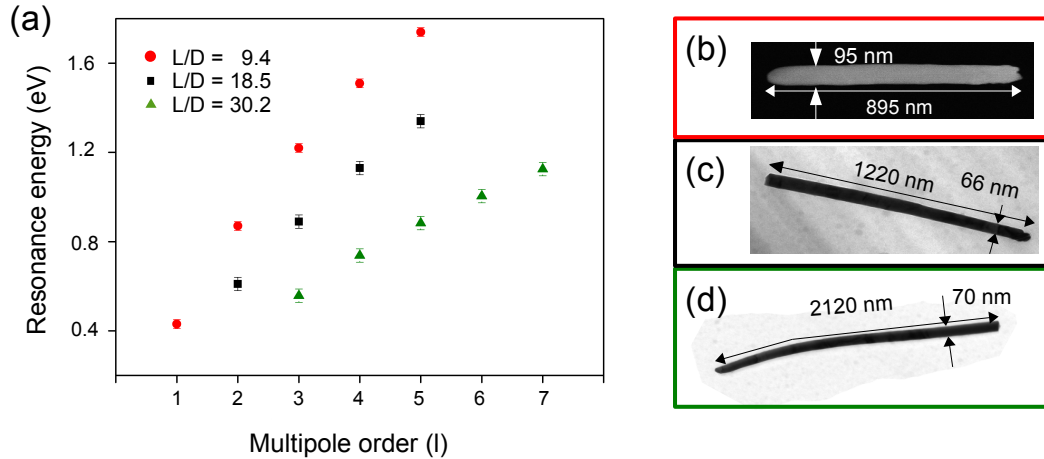


Figure 8.2: (a) Experimentally determined SP energies versus multipole order l for three gold nanowires with different aspect ratios, namely 9.4 (red circles), 18.5 (blue squares) and 30.2 (green triangles). TEM images of the three nanowires are depicted in (b), (c) and (d).

to the resonance energies of the wire with aspect ratio $AR = L/D = 9.4$ (shown in Figure 8.1), the black squares show the resonance energies of a Au nanowire with length $L_2 = 1220 \pm 10$ nm, diameter $D_2 = 66 \pm 10$ nm, and $AR = 18.5$, while the green triangles depict the resonance energies of the longest wire with $L_3 = 2120 \pm 10$ nm, $D_3 = 70 \pm 5$ nm, and $AR = 30.2$. These measurements evidence that the resonance energy of a fixed multipole order shifts to lower energies with increasing nanowire aspect ratio, as explained in Section 6.3. The investigated nanowires are elongated and thus retardation effects can not be neglected.^{126–129} This implies that not only the aspect ratio, but also the nanowire length determines the resonance energies. Since for the three wires the length increases with the aspect ratio, this does not result in a noticeable effect in Figure 8.2. For the wires having aspect ratios of 18.5 and 30.2, the $l = 1$ mode as well as the $l = 2$ mode of the longest wire are shifted to energies lower than 0.4 eV. They are thus not resolvable in the EEL spectra. Instead, with increasing aspect ratio, higher-order multipole modes shift into the energy range investigated here. For the nanowire with aspect ratio 30.2, SP modes up to $l = 7$ are measurable. These results support that EELS-STEM measurements are an excellent method to analyse the multipolar SP modes of elongated nanowires. For all three wires, a decrease in energy distance between two consecutive modes can be confirmed.

With increasing aspect ratio, the difference between two specific multipole modes decreases.

Figure 8.3 shows the resonance energies of Au nanowires with same dimensions as those measured in Figure 8.2 calculated via finite element simulations using CST Microwave Studio (large symbols). The colors of the symbols were chosen to be the same as for the wires with identical dimensions in Figure 8.2. In the simulation the nanowires were treated as cylindrical structures with hemispherical ends. They were located on top of a Si_3N_4 film ($\epsilon = 4, \mu = 1$) with thickness 30 nm. The assumed lateral dimensions of this thin film are $1200 \text{ nm} \times 2000 \text{ nm}$. The excitation was performed via a dipole. More details of the chosen simulation parameters are given in Section 7.2. The smaller symbols with error bars indicate for comparison the measured energies of the three wires that were already presented in Figure 8.2.

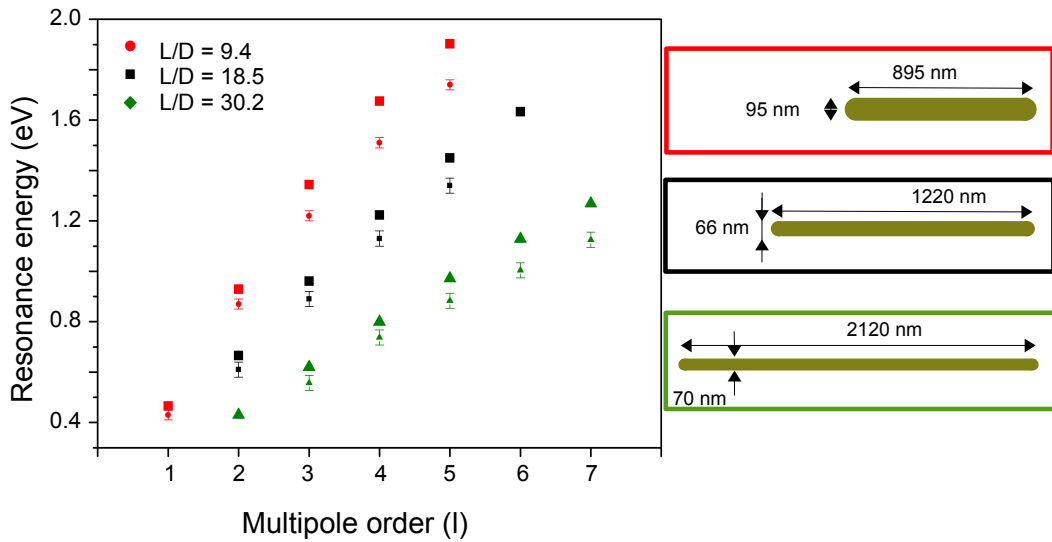


Figure 8.3: Calculated resonance energies (big symbols) using CST Microwave Studio for three gold nanowires with the same dimensions as the wires in Figure 8.2. In addition, the experimentally determined values for the three wires are plotted for comparison (smaller symbols with error bars).

Overall, Figure 8.3 reveals a good agreement between simulation and experiment. The calculated and measured energies show both the same trends: A decrease of the energy difference of consecutive modes with increasing order, and decreasing resonance energies with decreasing aspect ratio for all multipole orders. However, all calculated resonance energies are slightly shifted to the blue with respect to the measured ones. This agrees with results of other groups.^{46, 114} Remarkably, the authors used different synthesis techniques, namely electron beam lithography and seeded mediated growth,

and in Ref. 46 the discrete dipole approximation was applied for the calculations. It can thus be concluded that neither the specific simulation model nor the synthesis technique account exclusively for this deviation. The deviation, by trend, increases with multipole order and energy. We attribute these deviations to the morphological characteristics of the wires, as well as to a small frequency dependence of the dielectric function of Si_3N_4 , which was neglected in the simulation. As mentioned above, simulations considered an ideal wire with smooth surface and hemispherical ends. The TEM images in Figure 8.2b-d reveal however diversely shaped ends. It is well known that the shape of the nanowire ends influences its resonance energies.^{25,129} In addition, as discussed in Section 4.1.2 the nanowire surface exhibits a certain roughness. Few papers address so far the dependency of roughness on the resonance energies.¹³⁰⁻¹³³ The authors reported a redshift of the resonance energies with increased surface roughness. The influence of the surface morphology of a nanowire on its resonance energies will be discussed further in Section 8.2 for the example of a porous nanowire.

The specific curve shape in Figure 8.3 suggests that a simple relation exists between the resonance energies and the nanowire dimensions. An analytical formula, which would allow the determination of the resonance frequency without time consuming boundary element method or finite element calculations would be of great value. For perfect conductors, a direct proportionality $L = \text{const.} \times \lambda$ between length L and resonance wavelength λ exists. This relation does not hold for nanowires when approaching the optical frequency regime. Here penetration of light into the material is possible, leading to a shortened resonance wavelength λ and thus an increased resonance energy.¹³⁴

Khlebtsov et al. proposed a linear relationship between the resonance wavelength and the ratio between aspect ratio (AR) and multipole order l .²⁵ Since the resonance wavelength is inversely proportional to the resonance energy E , it is:

$$\frac{1}{E} = A_0 + A \frac{AR}{l}, \quad (8.1)$$

where A_0 and A are constants for fixed nanowire diameters.

Measurements of several multipole SP resonances of nanowires with varying aspect ratio, as presented here, establish the possibility to experimentally verify this model. In Figure 8.4a, $\frac{1}{E}$ is therefore plotted versus $\frac{AR}{l}$. In Figure 8.4b, the same plot is presented for the calculated values. The colors of the symbols were chosen to be the same as in Figure 8.2. The colored lines originate from linear regression analysis for the values of the three wires.

With exception of the dipolar mode, that was experimentally resolved only for the nanowire with the smallest aspect ratio, there is an excellent agreement between

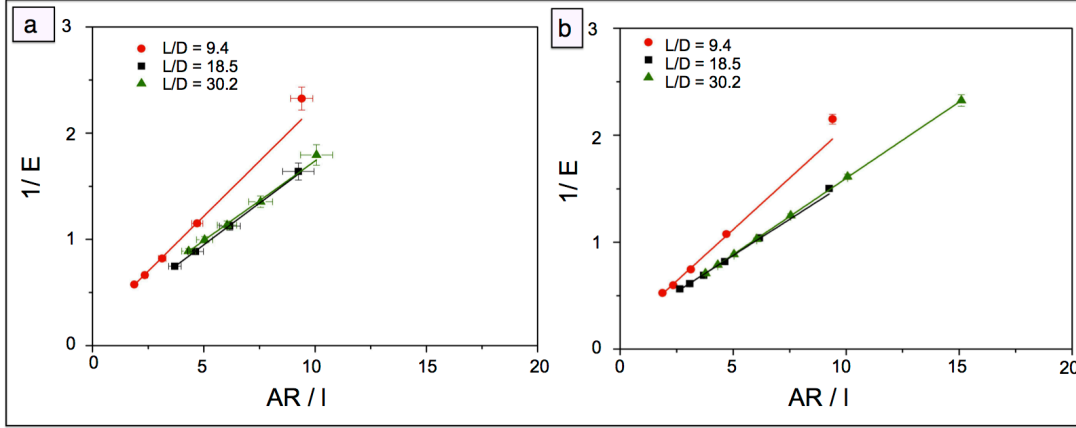


Figure 8.4: (a) Inverse of the measured resonance energies for three wires with aspect ratio 9.4 and diameter $D = 95 \pm 5$ nm (red dots), aspect ratio 18.5 and diameter $D = 66 \pm 5$ nm (black squares), and aspect ratio 30.2 and diameter $D = 70 \pm 5$ nm (green triangulars) plotted versus the ratio between aspect ratio AR and multipole order l . The colored lines are linear regression curves for the measured values. (b) Same as in (a) but here the calculated values are plotted.

the data points and the linear plot. For the two other wires, the dipole resonance energy was not resolvable, due to its proximity to the zero-loss peak. Khlebtsov et al. found also deviations from a perfectly linear curve for their calculated values especially for the dipole mode.²⁵ Better agreement between the linear equation and the data points was found for spheroids. Possible explanations for the deviation are the shape of the dielectric function, leading to different penetration depths into the material at different frequencies, and the nanowire end shape leading to different phase jumps of the electron wave upon reflection at the nanowire end. Further, for the two wires with very similar diameter ($D = 66$ nm (black squares) and $D = 70$ nm (green triangles)), slope and axis intercept are almost identical, confirming that A and A_0 in Equation 8.1 are constant for nanowires with same diameter, shape and material for multipole orders higher than 2. The constants A_0 and A are determined for the three nanowires from the linear regression as follows and can be used for the determination of multipole SP resonance energies of nanowires with these diameters. This linear relationship will be important for the analysis of the results of heterodimers in Section 9.2.

NW diameter	Experimental		Simulation	
	A_0	A	A_0	A
$D = 95$	0.18 ± 0.02	0.21 ± 0.01	0.15 ± 0.03	0.19 ± 0.01
$D = 70$	0.24 ± 0.03	0.150 ± 0.005	0.170 ± 0.003	0.1427 ± 0.0007
$D = 66$	0.16 ± 0.01	0.157 ± 0.003	0.198 ± 0.01	0.136 ± 0.004

8.2 Influence of composition and morphology

In this section the SP resonances of smooth and porous AuAg alloy nanowires are analysed and compared to the results on the resonances of the pure Au nanowires with similar dimensions.

In Figure 8.5, a high-resolution plasmonic energy loss map of a AuAg alloy nanowire, consisting of 50 EEL spectra is presented. The map has been measured along the length of the AuAg nanowire as indicated by the red arrow in the TEM image. The energy varies from left to right from 0.25 to 3.0 eV. The color scale indicates the number of counts. The AuAg wire has a length $L = 907 \pm 5$ nm and a diameter of $D = 107 \pm 5$ nm, the dimensions are thus very similar to the ones of the pure Au wire in Figure 8.1. The nanowire was deposited from an electrolyte containing 50 mM $\text{KAu}(\text{CN})_2$ and 20 mM $\text{KAg}(\text{CN})_2$ at $U = -1.1$ V. After dissolution of the polycarbonate membrane, the AuAg alloy nanowires were transferred to the Si_3N_4 substrate. The sample was then annealed at 300°C for 30 min as discussed in Section 4.2.3. The Au:Ag ratio in this nanowire is about 65:35 (see Section 4.1.1) estimated by EDX in SEM.

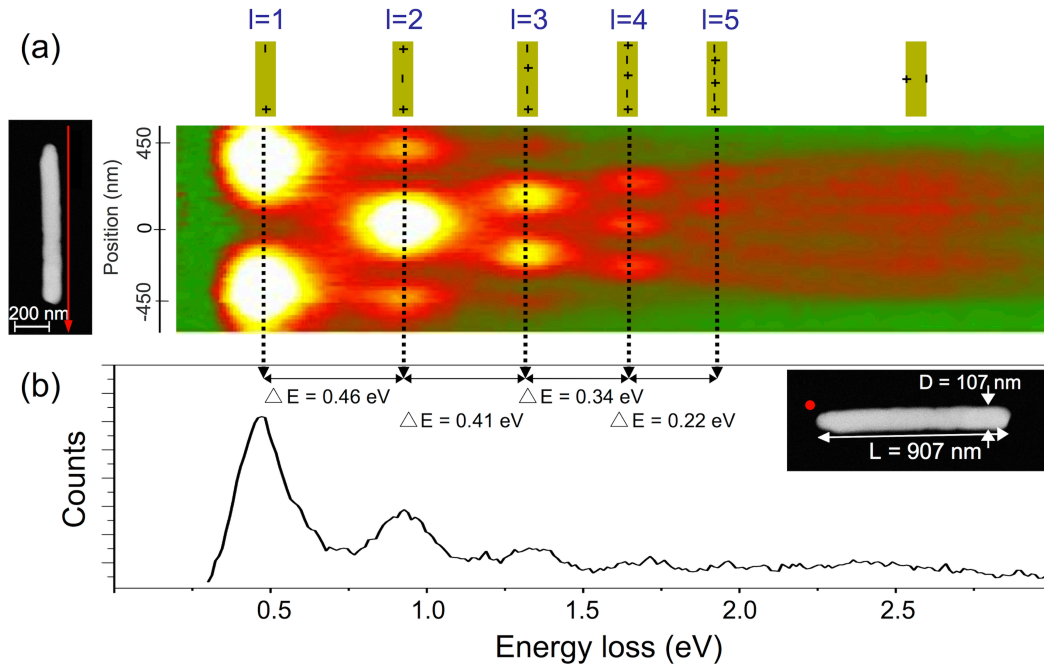


Figure 8.5: (a) High-resolution plasmonic energy loss map consisting of 50 EEL spectra measured in longitudinal direction of a AuAg nanowire with $L = 907 \pm 5$ nm and $D = 107 \pm 5$ nm. On top of the map the electric field distribution for the different SP modes is shown schematically. (b) One spectrum extracted from the map at the position of the red dot in the TEM image.

Similar to the findings for the pure Au wire (Figure 8.1), the map reveals five longitudinal modes and a transversal mode. The transversal mode is centered at ~ 2.6 eV, which is higher than the energy of the transversal mode of the pure Au wire ($E_T \sim 2.3$ eV). The slightly larger diameter of the AuAg alloy wire compared to the pure Au wire ($L = 895 \pm 5$ nm, $D = 95 \pm 5$ nm) and thus the decreased aspect ratio, would cause a slightly smaller resonance energy for the transversal mode when taking into account only the nanowire geometry.³¹ It is thus concluded that the blueshift of the transversal mode is most probably due to the Ag content. This is supported by previously reported results on AuAg nanoparticles, where it was found that the resonance energy shifts to the blue continuously with increasing Ag content. For 20 nm nanoparticles, Link et al. report a resonance wavelength shift from 520 nm (2.38 eV) for pure Au particles to 420 nm (2.95 eV) for Ag₇₃Au₂₇ nanoparticles.¹³⁵ For the longitudinal modes, it is not possible to judge from this figure how the Ag content influences the resonance energies. The energies for the different multipole modes are 0.47 ± 0.01 , 0.93 ± 0.01 , 1.34 ± 0.01 , and 1.68 ± 0.01 eV and slightly shifted to the blue with respect to the ones of the pure Au wire that has a slightly larger aspect ratio (Figure 8.1). This is what one expects also for two pure Au wires with different length and similar diameter. In addition, the decrease in intensity of the maxima in the map with increasing energy, and the decrease in energy difference between two consecutive modes is valid for the AuAg nanowire.

In addition to the smooth AuAg nanowires, also porous AuAg alloy nanowires were investigated. Figure 8.6 shows a TEM image of a porous nanowire. The nanowire was prepared with an electrolyte containing 50mM KAu(CN)₂ and 50mM KAg(CN)₂ at -1.1 V. After the deposition the nanowire was treated with nitric acid for 3 h to dissolve the Ag atoms. The nanowire has a length of 1000 ± 10 nm and a diameter of 90 ± 10 nm. The TEM image visualizes an inhomogeneous porosity along the wire. An EDX line scan (green arrow) was performed along this nanowire and allows the distinction of three different parts: A less porous part on the left of the image, where the Ag concentration is highest; a strongly porous part in the middle of the wire, with pore sizes up to ~ 20 nm and a lower Ag content; finally a small part on the right which is not porous, here the Ag concentration being lowest. This non-constant Ag concentration has to be considered during the SP analysis and is caused by the synthesis process. Probably, the Au-rich part is due to the sputtering process during the nanowire synthesis (*cf.* Section 3.2). To create a cathode for the electrodeposition a Au layer was sputtered on the backside of the polymer template. It is known that, during this process, sputtered Au enters the pores, resulting in a short Au

nanowire segment. The inhomogeneous porosity is assigned to the hydrophobicity of the substrate. A high porosity is related to an efficient dealloying process and thus a resulting small Ag content.

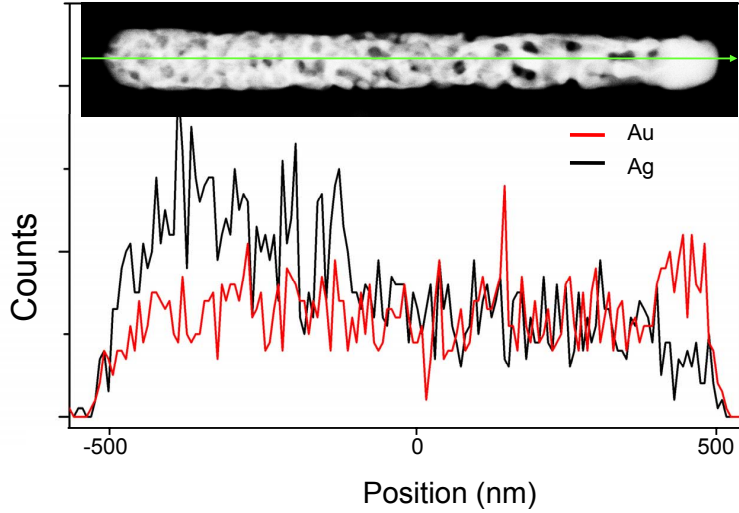


Figure 8.6: Top: TEM image of a 1000 ± 10 nm long porous AuAg nanowire. Bottom: EDX in SEM scan along this nanowire. The black line signifies the count numbers of the M_{α} -Peak of Au and red line the counts of the L_{α} -Peak of Ag.

Figure 8.7a shows the high-resolution plasmonic energy loss map, consisting of 100 EEL spectra, measured along this porous nanowire. As for the Au wire and the smooth AuAg alloy wire, each horizontal line corresponds to one spectrum and the color in the map indicates the number of counts. Figure 8.7b depicts one spectrum extracted from the map, its acquisition site being marked in the TEM image by the red dot. Similarly as for the Au and the AuAg nanowire, the map reveals four low energy modes that can be assigned to the longitudinal modes of multipole orders $l = 1$ to 4. Furthermore, the decrease in intensity with increasing energy, and the continuously decreasing energy difference between two consecutive modes can be confirmed also for the porous AuAg nanowire. Overall, the porosity of the nanowire seems to have a surprisingly small impact on these four low-order longitudinal SP modes. As for the pure Au and smooth AuAg alloy nanowires, these modes reveal in position and intensity almost mirror symmetry to the wire center.

On the other hand, for the modes at energies higher than 1.6 eV the symmetry is lost. The intensity maxima are shifted in energy depending of the position along the wire and it is difficult to assign them to a specific mode. Since both, the composition and the porosity vary along the nanowire, it is not possible from this investigation to discern their influence. Further investigation will be devoted to this in the future.

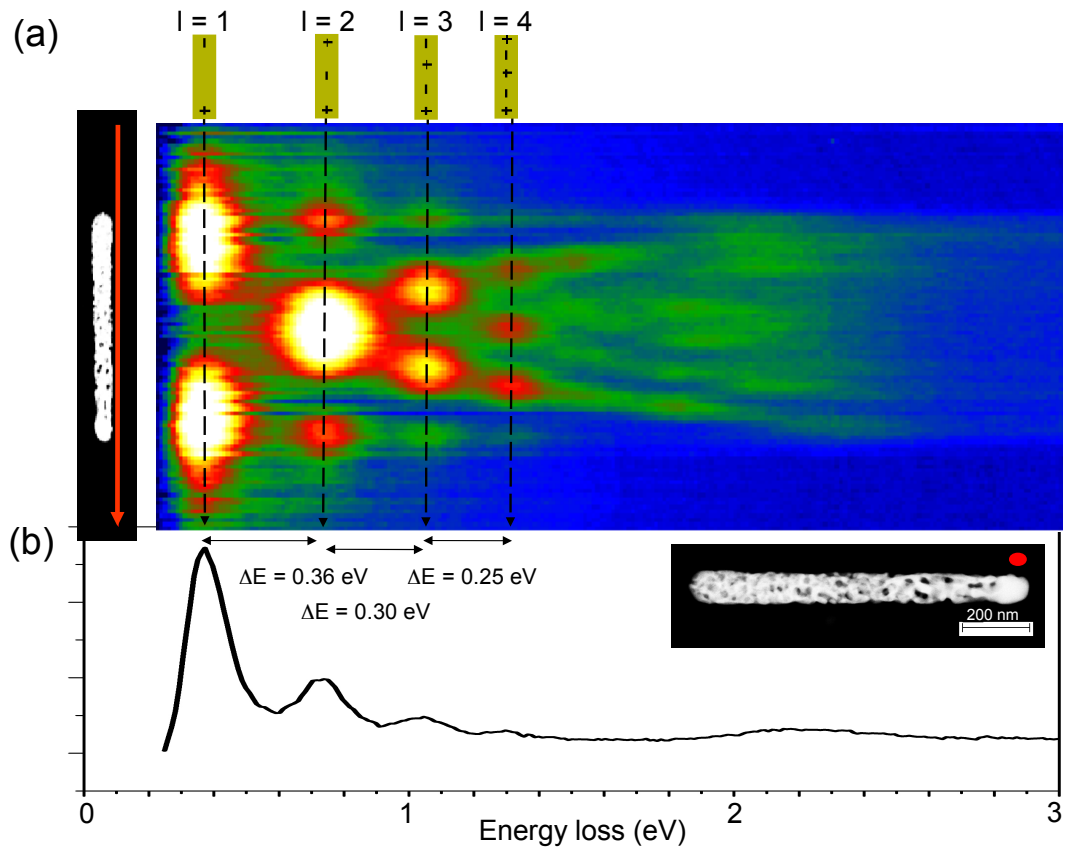


Figure 8.7: (a) High-resolution plasmonic field intensity map consisting of 100 EEL spectra measured along the long axis of a nanowire in the direction of the arrow on the left. The color indicates the number of counts. (b) Electron energy loss spectrum (EELS) measured at one end of the single nanowire. The inset shows a TEM image of the single nanowire corresponding to the spectrum. The red dot marks the position of measurement.

In contrast to the map of the single Au nanowire in Section 8.1 and the previously discussed smooth AuAg wire, a transversal mode is not clearly resolvable, although the scan is performed at a distance of only about 10 nm from the wire surface which is similar to the distance of the scan along the pure Au wire in Figure 8.1. It remains unclear, whether the porosity prevents the efficient excitation of the transversal mode or whether a transversal mode is excited and its energy shifts strongly with the position along the nanowire due to the varying porosity and Ag concentration. This second possibility seems probable, since at high energy the map reveals broad intensity maxima, resembling the ones of the transversal modes identified in the maps of the pure Au and the smooth AuAg alloy wire (*cf.* Figures 8.1 and 8.5). We assume thus that this second case is appropriate. The energy of this mode is from the map in Figure 8.7 determined to vary between 2 and 2.3 eV and depends on the position along the

wire. These energies are lower than the energy E_T of the transversal mode of the pure Au wire centered at 2.3 eV (*cf.* Figure 8.1). For the smooth AuAg alloy wire, an even higher energy $E_T = 2.6$ eV was found. Thus, most probably the porosity accounts for a shift to the red of the transversal mode compared to the one of a smooth wire with similar dimensions. These observations are in agreement with the observations reported in Ref. 85 where the transversal mode is as well observed to shift to the red with increasing porosity.

To further clarify the influence of the porosity and the Ag content on the low-order longitudinal modes, the resonance energies of the smooth AuAg alloy nanowire (light blue stars) are depicted in Figure 8.8a versus multipole order together with the values for the three pure Au nanowires (see Section 8.1, red dots, black squares and green triangles). The experimental energies are depicted by the small values with error bars, the corresponding simulation results are represented by the larger symbols of the same color. In the simulation all wires were treated as pure Au regardless whether they were Au or AuAg alloy wires. This assumption was made due to the lack of knowledge on the dielectric function of AuAg in the ratio 65:35 and on the distribution of Au and Ag atoms in the synthesized wire. In Section 2.3.3 it was mentioned that the dealloying of AuAg bulk material can lead to structures that are covered on the surface with pure Au, while the core of the material consists of AuAg. For the nanowires, we do not have results on the distribution of the Au and Ag atoms at the moment. From results of core-shell AuAg nanoparticles it is known that also this distribution of Au and Ag atoms influences the resonance energies.¹³⁶ The parameters defining the Si₃N₄ substrate are in Figure 8.8 the same as in Figure 8.3.

The simulated energies indicate in general that the resonance energies decrease with increasing aspect ratio. An exception are the $l = 1$ and 2 modes of the nanowire with $AR = 9.4$ and 8.5. The wire with aspect ratio $AR = 8.5$ is slightly longer than the one with $AR = 9.4$. Thus, retardation effects are not negligible^{126–129} and shift the $l = 1$ and 2 modes of the longer wire to lower energies than those of the shorter wire, although its aspect ratio is smaller.

Comparing theoretical and experimental results, we found that for the light blue data points the deviation between measurement and calculation is smallest. These data points correspond to the energies of the experimentally investigated AuAg alloy that was in the simulation treated as pure Au wire. In particular the good agreement of these resonance energies is remarkable, since for the three Au wires we found an increased deviation between calculation and measurement with increasing energy. The AuAg nanowire is the one with the smallest aspect ratio and thus the highest resonance

energies for the modes of multipole order $l = 3, 4$ and 5 . We conclude that the resonance energies of this wire are shifted to the blue compared to a pure Au wire with same dimensions. We assume that this blueshift is either due to the Ag content in the wire or to the annealing at 300°C for 30 min resulting in a rounding of the wire ends (See Section 4.2.3) and most probably a smoothing of the wire surface.

In Figure 8.8b, the resonance energies of the porous AuAg nanowire (Figure 8.7, blue squares with error bars) are shown together with the ones of two other porous AuAg nanowires with different aspect ratios (violet and orange values with error bars). The TEM images on the right of the figure depict the three wires. The colors of the frames of the boxes are the same as the colors of the corresponding data points. The larger symbols of the corresponding colors indicate again the calculated energies of three nanowires with the same lengths and diameters. In contrast to the experimental measured wires, in the simulation the wires were treated as smooth wires consisting only of Au atoms.

The deviations between calculated and experimental energies are larger for all values in Figure 8.8b than in Figure 8.8a. Exemplarily for the $l = 3$ mode, the energy differences between simulation and experiment are for these three wires $\Delta E = 0.18, 0.15,$ and 0.13 eV, while the differences for the Au wires in Figure 8.8a are only $\Delta E = 0.11, 0.07,$ and 0.06 eV. We assume thus that the big difference in Figure 8.8b between simulated and measured energies is caused by the porosity of the experimentally investigated wires that was not taken into account in the simulation. This leads to the conclusion that porosity results in a redshift of the resonance energies compared to those of unporous wires with identical dimensions. The Ag content, present in all the porous wires, would rather account for a blueshift of the experimental values, as discussed above.

This redshift of the resonance energies of porous wires compared to their smooth counterparts is in agreement with results reported in Ref. 85, where nanowires in solution are analysed using infrared-visible spectroscopy. The porosity is interpreted as an effective length increase of the nanowire, due to an increased surface area. Such a length increase results in a redshift of the resonance energies for the porous nanowire compared to a smooth Au wire with the same dimensions.

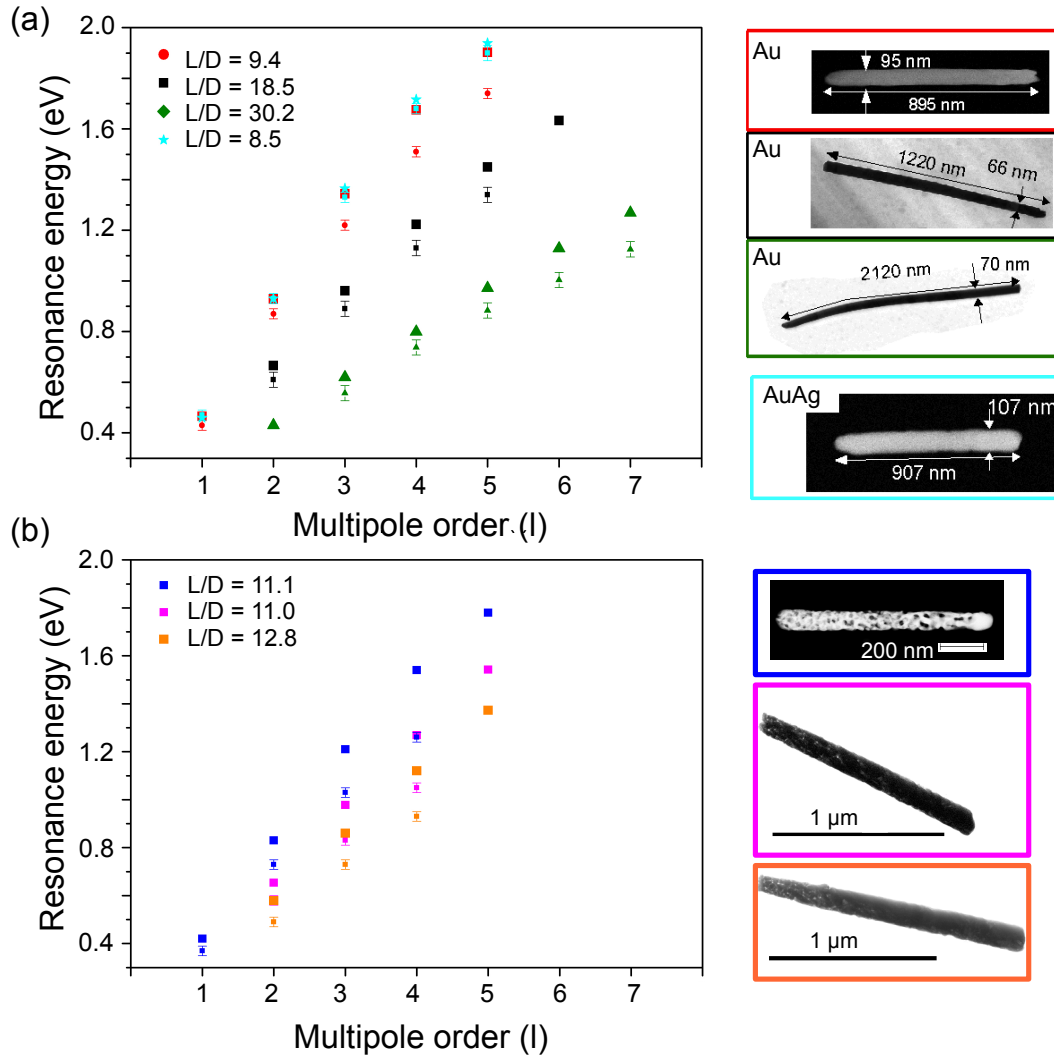


Figure 8.8: (a) Measured (small symbols with error bars) and calculated (large symbols) resonance energies of four nanowires with different aspect ratio (red $L/D = 9.4$, black $L/D = 18.5$, green $L/D = 30.2$ and light blue $L/D = 8.5$). While the wires corresponding to the red, black and green symbols were in simulation and experiment pure Au wires, the wire corresponding to the light blue values was in the experiment a AuAg wire. In the simulation the wire had the same dimensions as in the experiment but consisted only of Au. (b) Measured and calculated resonance energies of wires with aspect ratio 11.1 (blue squares), 11.0 (violet squares) and 12.8 (orange squares). In the experiment the wires were porous AuAg alloy wires, while in the simulation they were treated as smooth Au wires.

8.3 Dispersion relation of single nanowires

The energy loss probability as a function of the energy depicted in the maps in Figures 8.1, 8.5 and 8.7 is related to the electric field component in z -direction as explained in Section 7.1. Thus, in contrast to many other SP investigation methods, applying

EELS, information on the spatial distribution of the electric field z -component can be obtained.

For the pure Au nanowire (Figure 8.1), the AuAg alloy nanowire (Figure 8.5) and the porous AuAg nanowire (Figure 8.7) linescans (count number versus position) along the three wires at their resonance energy of the $l = 2$ (red line), 3 (green line), 4 (blue line), and 5 (black line) modes are extracted from the corresponding SP maps and shown in Figure 8.9. The $l = 5$ mode is only clearly resolvable in the map of the pure Au wire (see Figure 8.1). The count maxima in the linescans represent the positive and negative electric field maxima of the SP modes. The distance between two maxima is marked by black arrows, and is given by the numbers on top. The linescans of all the three different nanowires reveal for the $l = 3, 4$ modes (in the case of the pure Au wire also for the $l = 5$ mode) that the distance between two maxima close to the wire end is reduced, compared to the distance between two maxima in the center of the wire. This observation is in good agreement with results reported in Refs. 46 and 47 for silver nanowires with length 400 nm and diameter 15 nm, as well as length 700 nm and diameter 50 nm, respectively. Our results evidence that similar effects occur also in Au nanowires, AuAg alloy nanowires, and porous AuAg nanowires with lengths in the μm range and diameters approximately 100 nm. This distance reduction at the nanowire ends is explained by a phase shift $\delta\Phi$ occurring upon reflection of the wave at the wire ends (see Equation 6.5) that is illustrated schematically in Figure 8.9d. The two black sinusoidal curves depict the electron wave, and its phase shifted reflected wave. The blue curve shows the superposition of the two waves. In Ref. 46 it was shown that $\delta\Phi$ is energy dependent.

Thus, we determine the SP half wavelengths $\lambda_{sp}/2$ of the structures by measuring the distance between two maxima located in the middle of the nanowire. For the $l = 2$ mode, the half wavelength is measured by determining the distance between the two minima instead of the maxima, to eliminate the end effect.

In Section 8.1 the relation between the excitation energy of multipole order resonances and the aspect ratio for fixed diameters of the nanowires was investigated. This relation would be equivalent to the dispersion relation of the nanowires, if the length would be $L = \frac{\lambda_{SP}}{2}l$. However, we found that due to the $\delta\Phi \neq 0$, as visible in Figure 8.9, this relation is not valid. It is thus interesting to investigate the relation between the resonance energies and the SP wavelengths.

In Figure 8.10, the resonance energies of the three nanowires are plotted versus the wavenumber k of the different multipole modes from $l = 2$ to 5. The curve for light in vacuum is depicted by the orange line. The wavenumbers k are given by $k = 2\pi/\lambda_{SP}$.

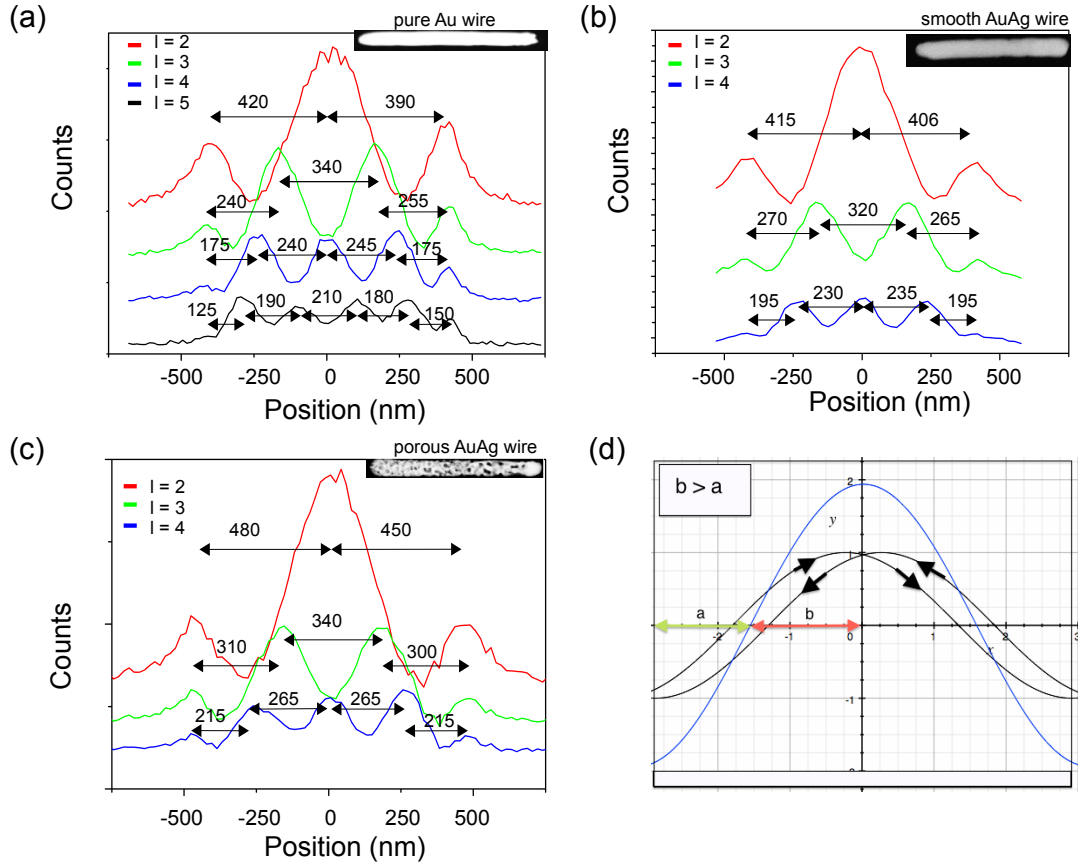


Figure 8.9: Count numbers versus position along (a) the Au nanowire, (b) the smooth AuAg nanowire and (c) the porous AuAg nanowire for the different multipole modes. For the pure Au wire, the modes $l = 2$ to 5 are shown, for the other two wires only $l = 2$ to 4 are depicted. All distances are given in nm. (d) The black curves show an incoming wave and its slightly phase shifted reflected wave. The blue line corresponds to the superposition of these two waves, illustrating that two different distances a and b between maxima in the middle of the nanowire and close to its end are created.

For the Au (red dots) and the AuAg (light blue squares), the determined data points follow almost identical curve shapes within their error bars. To minimize these errors and clarify the agreement of the two curves, the scanning should have been performed with smaller step width. The dispersion curves of the SP modes of a Au and a AuAg nanowire are given by the interpolation of the data points, respectively. Their slopes are the SP velocities. The good agreement between the dispersion curve of the Au wire and the AuAg wire that can be seen in Figure 8.10 is attributed to the similar dielectric functions of Au and Ag at low energies, the small Ag content in the wire of about 35%, and the similar dimensions of the two wires. It is visible that in all cases the velocity is smaller than that of light in vacuum. We furthermore

find that the curves follow the same trend as the dispersion curve of propagating SP polaritons in a plane metal-dielectric interface, which have a velocity close to the speed of light in vacuum for low wavenumbers and a decreased velocity for higher wavenumbers. This behaviour can be understood in analogy to the response of a mass on a spring to an oscillating external force. In the case of the SP resonance the mass is the electron mass responding to the field of the fast travelling electrons in the TEM and the restoring force originating from the ionic background. By comparing the resulting dispersion curves to previously reported dispersion curves, we find that the curves agree acceptably with the one reported for a Ag wire with diameter 47 ± 3 nm on a Si_3N_4 membrane in Ref. 47. In contrast, a dispersion curve revealing smaller velocities for SP in Ag wires is found in Ref. 46. Possible reasons for this are the much smaller diameters of the wires (13 - 15 nm) and the different substrate (TEM Cu grid with carbon layer).

Finally, for the porous nanowire, we obtain energies below the curve for the Au and AgAu nanowires. This can be explained by the increased surface compared to the smooth nanowires and thus an intrinsically larger wavelength and thus smaller wavenumber than measured from the linescans.

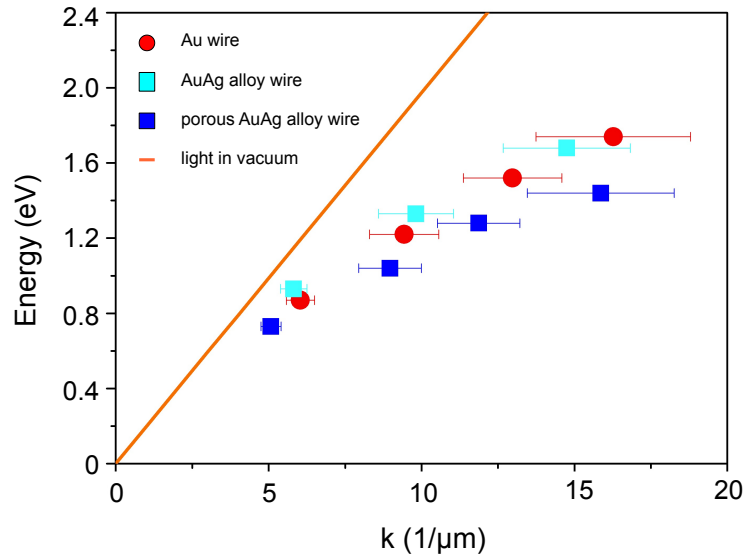


Figure 8.10: Resonance energies versus wavenumber for a pure Au nanowire (red dots), a smooth AuAg alloy nanowire (light blue squares), and a porous AuAg alloy nanowire (blue squares). The orange line corresponds to the curve of light in vacuum.

Chapter 9

Multipole surface plasmons in nanowire dimers analysed by EELS-STEM

Recently, structures consisting of several nanowires have attracted strong interest due to their potential for many applications as e.g. for sensorics and optical communication.^{137–139} In the following chapter, we present results on structures consisting of two nanowires with lengths between 500 and 1000 nm and diameters of about 100 nm, arranged in line.

In Section 9.1, structures consisting of two nanowires with very similar dimensions that are capacitively coupled by nanogaps as small as 8 nm are analysed. The structures are called symmetrical dimers or homodimers.¹¹⁷ Experimental results of such small gaps are rare in literature due to difficulties in the preparation process. In Section 9.2, we compare these results to those of unsymmetrical dimers, consisting of two wires with different dimensions. Section 9.3 presents the plasmonic properties of nanowires connected by small metallic bridges. The small junctions modify the plasmonic properties compared to those of capacitively coupled dimers since charge transfer between the wires becomes possible.

Using light microscopy techniques, it is not possible to distinguish between capacitively and conductively coupled nanowires. By EELS-STEM their properties, such as the resonance energies and the field distributions, are explored to analyse the influence of dimensions, connection size and gap size.

9.1 Capacitively coupled nanowire dimers

In the following section, STEM-EELS measurements are presented on dimers consisting of almost identical nanowires to investigate degeneracy of SP modes depending on the nanowire dimensions and the gap size. The experimental results are partly published in Ref. 48.

Figure 9.1a shows a high-resolution plasmonic field intensity map of a dimer of two AuAg nanowires separated by a gap of only ~ 8 nm. The dimer was prepared by electrodeposition of segmented $\text{Au}_{60}\text{Ag}_{40}/\text{Au}_{15}\text{Ag}_{85}/\text{Au}_{60}\text{Ag}_{40}$ nanowires, using a pulse sequence of three pulses (-1.1 V for 25 s, -0.5 V for 10 s, and -1.1 V for 25 s). After dissolution of the polycarbonate template, the nanowires were drop cast on a Si_3N_4 membrane and the Ag-rich segments were subsequently dissolved by treatment with nitric acid. The diameter of the dimer shown in Figure 9.1 is 112 ± 5 nm. The two wires have a length of 784 ± 5 nm and 808 ± 5 nm, respectively, resulting in a ratio $\beta = AR_1/AR_2 = 1.03 \pm 0.01$, where AR_1 and AR_2 are the aspect ratios of the wires. The intensity map is composed of two one-dimensional line scans. Each of them consists of 30 equidistantly spaced electron energy loss spectra measured along the long axis of one of the wires forming the dimer, as indicated by the red arrow. The two scan lines ensure an almost constant distance of the scan from the wire which is on average ~ 10 nm (see TEM image in Figure 3a). From left to right the energy loss varies from 0.25 to 3.0 eV. The colors indicate the number of counts and visualize the spatial distribution of the SP modes along the one-dimensional scan.

Figure 9.1b displays three spectra recorded at different positions of the dimer: the blue and green spectra were measured by placing the focused electron beam (few nanometres spot size) at the dimer ends, while the red spectrum was taken by placing the focused electron beam at the dimer gap. The corresponding colored dots in the TEM image of the inset specify the measurement positions of the respective spectra. The two spectra measured at the ends of the dimer (green and blue spectra) differ in intensity since they are not measured exactly at the same positions relative to the dimer ends (see TEM image in Figure 9.1b).

In Figure 9.1a, at least six low-energy modes of longitudinal character are visible that can be separated into three pairs, each pair having a smaller energy difference than the differences to neighbouring pairs. Each of these mode pairs is assigned to a bonding - antibonding pair of different multipole order $l = 1$ to 3. In the following, they are denoted as B_l - and AB_l -modes. The bonding mode corresponds to a charge distribution where charge carriers of opposite signs are accumulated at opposite gap ends. In contrast, the antibonding mode is excited when charge carriers of the same

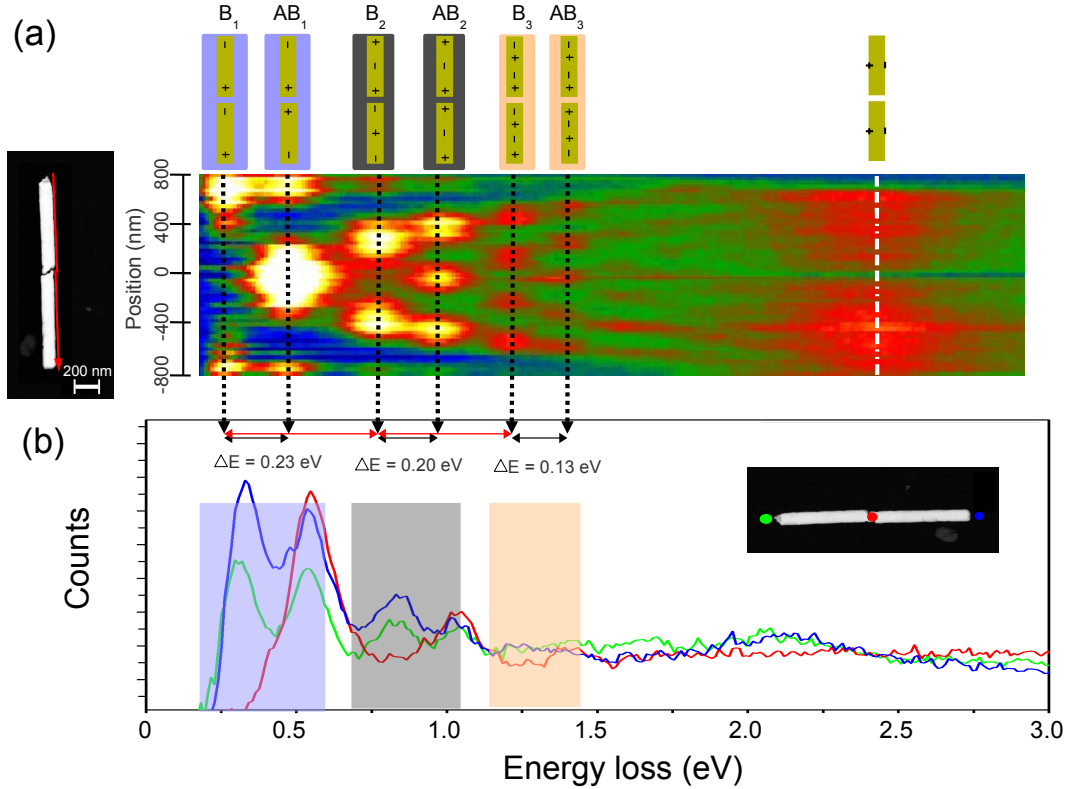


Figure 9.1: (a) Plasmonic field intensity map consisting of 60 electron energy loss spectra measured along a nanowire dimer (red arrow). The scan line has an average distance to the wire of ~ 10 nm. The wires are separated by a small gap of ~ 8 nm. The energy interval, plotted from left to right, ranges from 0.25 to 3.0 eV. The color represents the count number. The schematics on top represent the electric field distributions along the dimer. (b) Electron energy loss spectra measured at the two ends of the dimer (blue and green lines) and a spectrum measured in the dimer gap (red line). The colored dots in the TEM image inset specify the measurement positions for each spectra.

sign repel each other at the two gap sides. The attraction between negative and positive charge carriers at the two gap sides leads to a decrease in restoring force and thus to a shift in energy of the bonding mode to lower energies compared to the antibonding mode, as discussed in Section 6.4. The schematics on top represent the electric field distributions along the wire for each bonding and antibonding mode (purple for $l = 1$, grey for $l = 2$, and orange for $l = 3$). In Figure 9.1b, each mode pair is highlighted with the same color for further clarification. We observe splitting into bonding and antibonding modes not only for the dipole mode but also up to at least the third-order mode. The peaks corresponding to multipole orders higher than two at the two ends of the dimer are not visible in the spectra due to their low intensity but can be resolved at different color scaling. Figures 9.1a and 9.1b evidence that,

when the electron beam is positioned at the gap, only the antibonding modes are excited, whereas at the two ends of the dimer bonding and antibonding modes are excited. This is in agreement with observations published in Refs. 32 and 33.

In addition to the longitudinal modes, a mode centered at ~ 2.5 eV is discernible in Figure 9.1a. Noticeably, this mode is hardly excited when the electron beam is positioned close to the dimer gap. As for the single wire, it is efficiently excited along the wire, and decays rapidly beyond the two ends of the dimer. We assign this peak to a transverse mode of the dimer. The energy is similar to that of the transverse resonance of the single AuAg wire, and the mode is much broader compared to the longitudinal ones. It is known for the nanowires that several transversal modes are very close to each other in energy.³¹ Thus, besides increased interband damping with increasing energy, an overlap of several transverse modes due to a limited energy resolution, could be a possible reason for the broadening. As for the longitudinal modes, the transverse modes of a dimer split into bonding and antibonding modes³¹ leading to additional modes that could possibly further broaden the transverse peak of the dimer compared to the one of the single wire. In Figure 9.1b, the transversal mode at ~ 2.5 eV is not measurable in the two spectra at the dimer ends. Here, the mode is shifted to a lower energy centred at about 2.1 eV. This is in agreement to what we observed for the ends of the single nanowire (Figure 8.1).

The energy difference between two consecutive bonding modes (or two consecutive antibonding modes) decreases with increasing energy, as indicated by the red arrows in Figure 9.1b, from 0.50 ± 0.02 eV for the difference between the B₁- and B₂-modes to 0.45 ± 0.02 eV for the difference between the B₂- and B₃-modes. As mentioned above, each pair of a bonding and the corresponding antibonding mode appears to have a smaller energy difference compared to the difference to the next bonding-antibonding pair. The spectra in Figure 9.1a evidence that the energy difference between a pair of bonding and antibonding decreases with increasing multipole order from 0.23 ± 0.02 eV for $l = 1$ to 0.13 ± 0.02 eV for $l = 3$. This decrease with increasing multipole order confirms theoretical results of Willingham *et al.*³¹ and originates most probably from the lower induced electric fields for multipole orders compared to the dipolar mode and thus weaker interaction forces between the plasmons of the two individual wires.

The splitting into bonding and antibonding modes depends on the characteristics of the dimer. The two mappings in Figures 9.2a and 9.2b show exemplarily the splitting measured for two dimers with different aspect ratio and gap size. The dimer in Figure 9.2a consists of two wires with length 826 ± 5 nm and 764 ± 5 nm, respectively, diameter of 120 ± 5 nm, and gap size of ~ 7 nm. The spectra are measured at an average distance

from the wire of ~ 30 nm. In Figure 9.2b, the two wires have lengths of 958 ± 5 nm and 902 ± 5 nm, diameter of 100 ± 5 nm and a gap width of ~ 30 nm. The average distance of the scan line to the nanowire is ~ 15 nm. In both cases we do not consider the energy difference for the B_1 - and AB_1 -modes, to avoid errors originating from the proximity of the peaks to the zero-loss peak. The very small energy differences between bonding and antibonding modes for the third and fourth order in Figure 9.2b are measured by extracting appropriate spectra from the mapping. The center of the antibonding peak is measured from the spectra taken close to the gap where the bonding mode is not excited. Since the bonding and antibonding modes are not excited exactly at the same spatial position along the length of the nanowire as will be discussed in the following in more detail, the center of the bonding peak is measured at a position where the bonding mode is efficiently excited but not the antibonding mode. For the dimer in Figure 9.2a, having the smaller aspect ratio as well as the smaller gap size, the splitting of the higher-order modes is larger than for the dimer in Figure 9.2b, as expected from previously published simulations that showed that the splitting increases with decreasing gap size and decreasing aspect ratio.^{31,140} We plotted the energy splitting of the $l = 2$ modes as a function of gap size times aspect ratio for five different dimers in Figure 9.2c, confirming an increase in energy splitting with aspect ratio times gap size. Further investigations are necessary to discern the influence of aspect ratio and gap size separately. The aspect ratio of the dimer AR was calculated as L_d/D where L_d is the average length of both wires. In Refs. 34 and 141, an additional dependency of the energy splittings on $\beta = AR_1/AR_2$ was reported. We neglect this influence here since for all dimers considered in Figure 9.2c β ranges in a small interval between 1.03 and 1.12. The influence of β on the resonance energies will be analysed in the following Section 9.2 for higher β up to 1.62.

Figure 9.2d shows the linescans (count numbers versus position) for the dimers in Figures 9.2b (black line) and 9.1a (red line) at the center energy of the transversal plasmon resonance. These linescans are also depicted in Figures 9.2b and 9.1a by white dashed lines. As already mentioned, the transversal plasmon resonance is in both cases efficiently excited along the wires but is hardly excited close to the gap. Figure 9.2b reveals strong intensity fluctuations of this mode. We think that these fluctuations are related to the fact that the decay length into the dielectric perpendicular to the long wire axis is very short. For the single nanowire, we measured a decay length of about 20 nm, the decay length being defined as the distance at which the amplitude is reduced by a factor of e^{-1} . Thus, small diameter fluctuations of the wires together with small distance variations between wire surface and electron beam (average ~ 10 nm

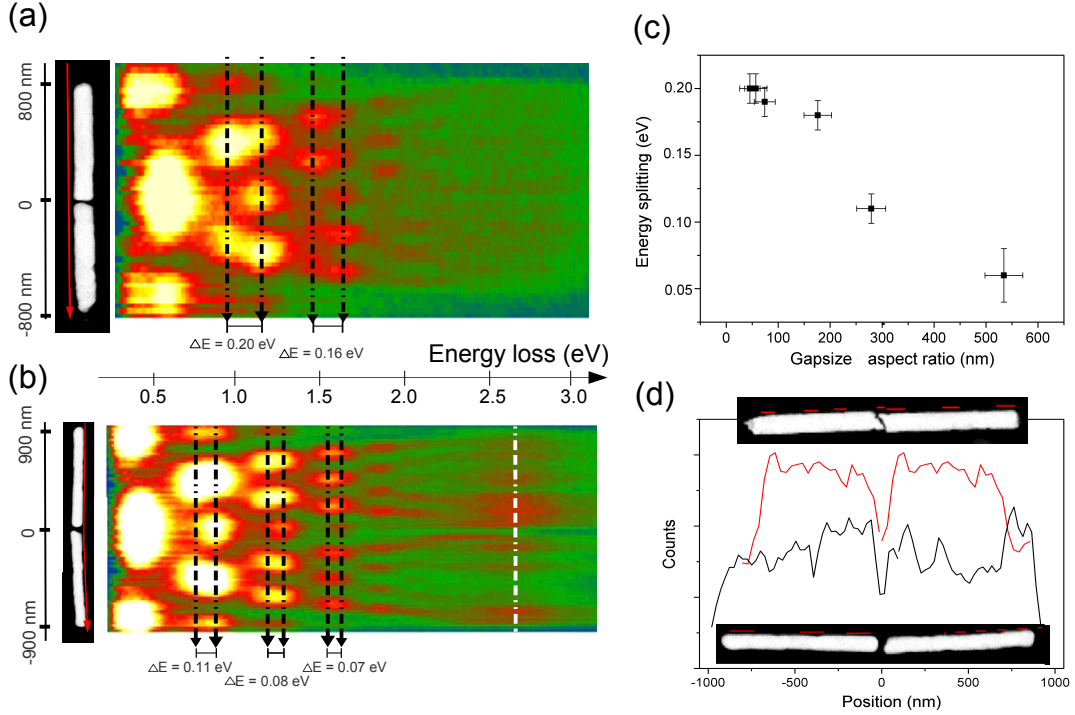


Figure 9.2: Plasmonic field intensity maps of two dimers with gap size ~ 7 nm and aspect ratio 6.5 (a), and (b) gap size 30 nm and aspect ratio 9.3. In (a) the distance between wire and scan line is on average ~ 30 nm, in (b) it is only ~ 15 nm. (c) Energy difference versus gap size of the $l = 2$ bonding and antibonding modes multiplied by the dimer aspect ratio for six different dimers. (d) Count number versus position along the dimers in Figures 9.2b and 9.1a at the center energy of the transversal mode (line scan marked by white dashed lines in these figures). The black line corresponds to Figure 9.2b and the red line to Figure 9.1a.

for scan line in Figure 9.1a and ~ 15 nm for scan line in Figure 9.2b) can account for the intensity fluctuations of this mode along the scan line. For the dimer in Figure 9.2a, we cannot distinguish the transversal plasmon resonance from the background since in this case the plasmonic field maps were measured at an increased distance of about 30 nm from the wire.

As for the single nanowire, we investigated the electron loss probability along the nanowire by extracting line scans from the map at the resonance energies of the modes. Figure 9.3 shows the linescans for the B_2^- - (black line) and AB_2^- -modes (red line), as well as the B_3^- - (blue line) and AB_3^- -modes (light blue line). The yellow highlighted area indicates the position of the two wires. A discontinuity in the profiles at the position of the gap is visible for all bonding and antibonding modes. This results from slightly different line scan distances from the gap, caused by a very small shift between the two line scans (one along each of the nanowires forming the dimer). Measuring two line

scans assured a constant distance to the wire surface along each of the dimer wires. In contrast to the single wire, we observed in the case of the dimer that the maxima are not arranged symmetrically to the middle of the wire. For the B_2 - and B_3 -modes, a shift of all maxima along the wire toward the gap was observed, whereas for the antibonding modes, the maxima shift toward the dimer ends. We attribute the shift between bonding and antibonding modes to the attraction of negative and positive charges at the opposite gap ends for bonding modes and to repelling of charges of equal sign for antibonding modes. In addition, we measure for the B_3 - and AB_3 -modes a shorter distance between the two maxima at the end of the wire than between the two maxima in the middle of the nanowire. This is in analogy to the observation for the single nanowire. Whether this can be understood in the framework of phase shifts at the wire ends as for the single wire remains up to now unclear. Due to the two slightly different lengths of the wires forming a dimer, one would expect slightly different wavelengths, which cannot be quantified with the present accuracy.

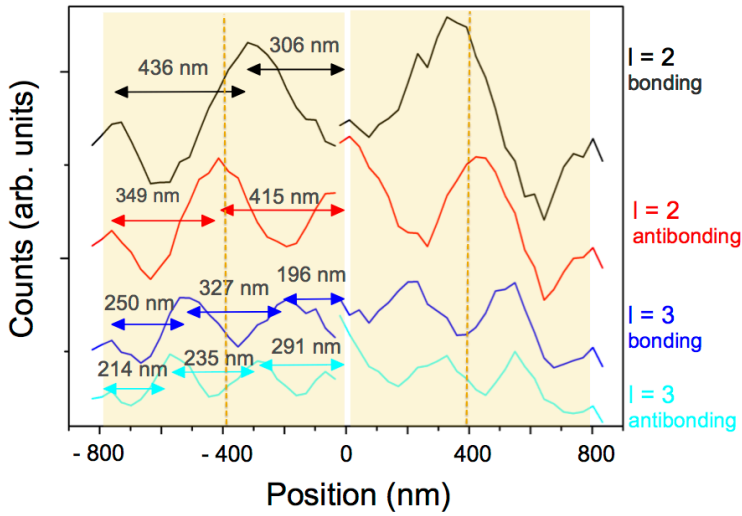


Figure 9.3: Line scans extracted from Figure 9.1 at the resonance energies of the $l = 2$ bonding mode (black line), $l = 2$ antibonding mode (red line), $l = 3$ bonding (blue line) and $l = 3$ antibonding mode (light blue line).

These results are compared to CST Microwave Studio simulations, to examine the experimental results and further investigate the influence of the gap size. Figure 9.4 shows the calculated electric field z -component for the B_2 - and AB_2 - modes, and the B_3 and AB_3 modes for two nanowire dimers. The excitation is performed via a small dipole as in the previous chapter and the parameters are given in Section 7.2. In the simulation the Si_3N_4 substrate is neglected, to keep simulation time at a reasonable limit. This causes additional shifts between resonance energies from measurement and

calculation. The nanowires have the same dimensions as the wires in Figure 9.3. The two-dimensional plots show a plane shifted by 10 nm in z -direction compared to the center plane of the structure, the color indicating the field strength. The gap width for the dimer on the left is 8 nm, while for the dimer on the right it is 16 nm. A small asymmetry to the structure center, that is found in the field distributions, is attributed to the two different lengths of the nanowires (784 nm and 808 nm) and the fact that the dipole is located at one nanowire end. The shifts of the electric field maxima with respect to the wire center are identified for the nanowire on the right. This wire is the slightly longer wire (808 nm).

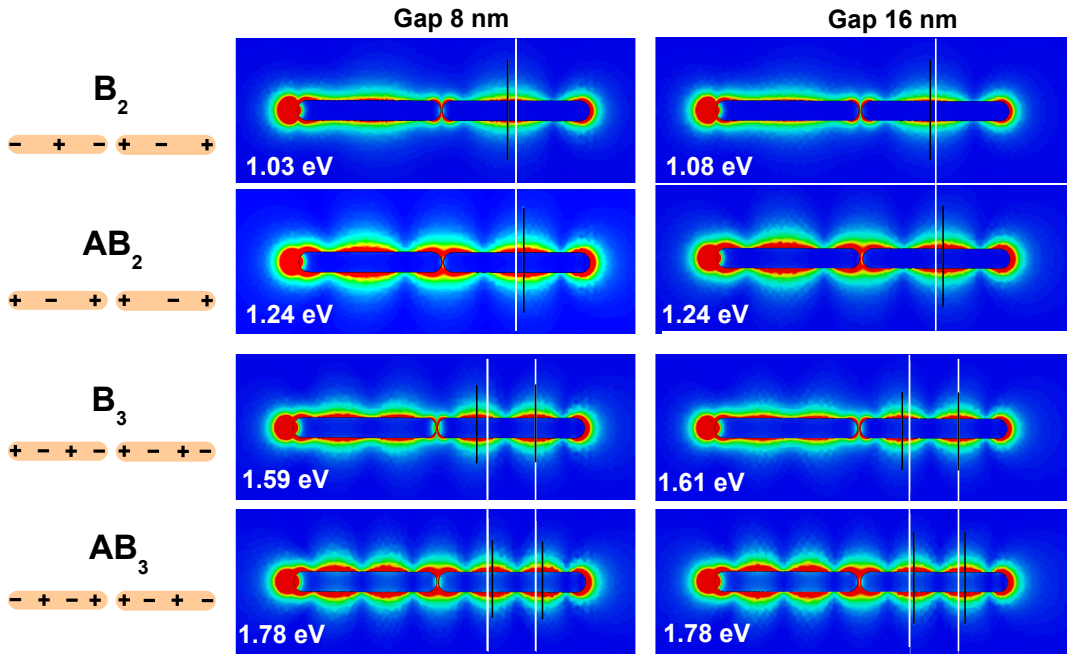


Figure 9.4: Amplitude of the electric field for two different dimers for the bonding and antibonding $l = 2$ and $l = 3$ modes. The images on the left show the field distribution for a dimer with gap size 8 nm, while on the right the width is increased to 16 nm. The dimensions of the nanowires are the ones of the dimer in Figure 9.1. The color indicates the field strength. The white lines mark for the $l = 2$ modes the center of the nanowire, while for the $l = 3$ modes they separate the nanowire into three parts of equal length. The black lines indicate the center positions of the electric field maxima.

For the B_2 and AB_2 modes, the center of the wire is marked with a white line, while for the B_3 and AB_3 modes the white lines separate the nanowire length into three equal sections. The center positions of the field maxima along the wire are marked by black lines. The simulation confirms for both wires that the maxima of the bonding modes are shifted in the direction of the gap, while the maxima of the

antibonding modes are shifted in opposite direction. This is in good agreement with the experimental results in Figure 9.3. Furthermore, one can see that the shifts of the bonding mode maxima are larger for the 8 nm gap than for the 16 nm gap. For the B_3 -mode, this is only the case for the maximum closer to the gap, while the second maximum is for both gap sizes excited exactly at the position of the white line. However, for the antibonding mode the shift in the direction of the dimer ends is independent of the gap size. This can be understood from Figure 9.5, where the field distributions at the gap are depicted in (a) for the B_2 -mode and in (b) for the AB_2 -mode. The arrows indicate the direction of the field, while the color marks the field strength. In the case of the B_2 -mode a high electric field is excited in the gap. In contrast, in the case of the AB_2 -mode the field inside the gap is low. Similar results are found for the bonding and antibonding modes of other multipole order (not shown in the figure). It is thus concluded that for the bonding modes the shift of the electric field maxima depends on the gap size, which is attributed to the localized field in the gap. For the antibonding mode, where the maxima are shifted in the opposite direction, the spatial shifts are independent of the gap size, since the electric field in the gap is low.

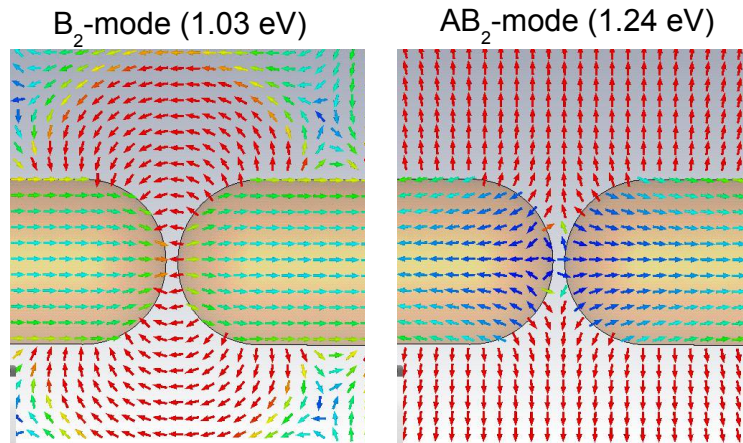


Figure 9.5: Electric field at the gap for the dimer with gap size 8 nm for the (a) B_2 - and (b) AB_2 -modes. The arrows indicate the direction of the field, and the color the field strength.

9.2 Capacitively coupled nanowire heterodimers

In Section 4.2, concerning the synthesis of the dimers, it was shown that by electrodeposition of $\text{Au}_{60}\text{Ag}_{40}/\text{Au}_{15}\text{Ag}_{85}/\text{Au}_{60}\text{Ag}_{40}$ nanowires and subsequent dissolution of the middle Ag segment, we can create dimers consisting of AuAg nanowires having same length or different lengths. We refer to them as symmetric and unsymmetric dimers, respectively. In the following, we analyse how the relative length ratio of the two nanowires forming the dimer influences the plasmonic properties of the structures. In the hybridisation model, unsymmetric dimers are also called heterodimers.¹¹⁷

At first, we present simulation results of heterodimers with very similar dimensions as synthesized, and secondly we compare the simulation results to EELS-STEM measurements.

Figure 9.6 shows three spectra calculated using CST Microwave Studio. As in the previous Section the excitation is simulated with a dipole using the parameters specified in Section 7.2. The spectra are calculated for a distance of 1 nm from the opposite end of the nanostructure and are normalized to the strength of the field if no nanostructure is present. The green line corresponds to a spectrum of a single nanowire with length $L_1 = 1036$ nm (green spectrum) and the blue line to a wire with length $L_2 = 656$ nm. Both wires have a diameter of $D = 76$ nm and hemispherical ends, as visible in the schemes on the right of the spectra. In addition, the red line in Figure 9.6 depicts a spectrum of a nanowire heterodimer. In this case, the dipole is located at a distance of 10 nm from the end of the longer wire. The nanowire lengths and their diameters are the ones of the two single wires (green and blue spectra), resulting in a ratio $\beta = AR_1/AR_2 = 1.58$, and thus much higher than for the wires discussed in Section 9.1, where β ranges between 1.03 and 1.12. The gap separating the two wires has a width of 12 nm. The blue and green vertical lines in Figure 9.6 indicate the multipole resonance energies of the two single wires, their field distributions are shown schematically on top of the corresponding peaks. The colors of the lines adopt the colors of the corresponding spectra. For the shorter wire, three longitudinal modes are resolvable. Their energies are $E_{l=1} = 0.65 \pm 0.01$ eV, $E_{l=2} = 1.30 \pm 0.01$ eV and $E_{l=3} = 1.82 \pm 0.01$ eV. To obtain the calculated spectra, the field was calculated for an suitably chosen sample of 300 energy values. The errors are defined as the energy difference between two consecutive energies of this sample. The notation of the previous sections is adopted, where the multipole order of the SP resonances is given by l , starting with $l = 1$ for the dipole mode. For the longer wire, four modes are clearly resolvable. Their energies $E_{l=1} = 0.44 \pm 0.01$ eV, $E_{l=2} = 0.87 \pm 0.01$ eV, $E_{l=3} = 1.29 \pm 0.01$ eV and $E_{l=4} = 1.64 \pm 0.01$ eV are for all multipole resonances

shifted to the red compared to the ones of the shorter wire.

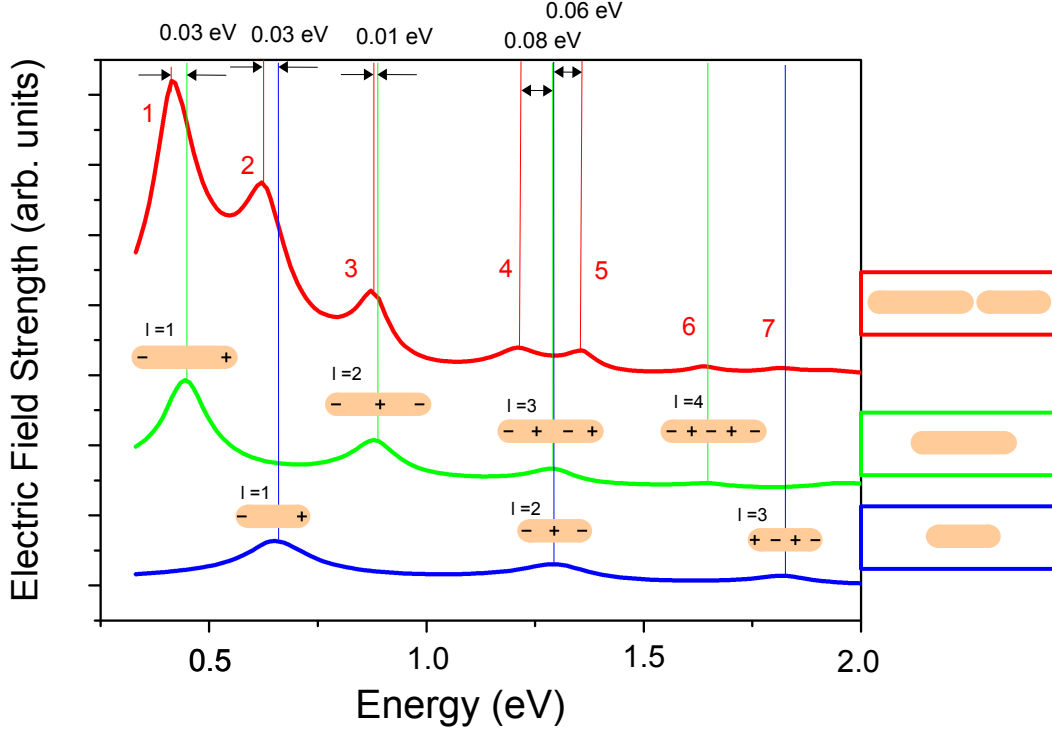


Figure 9.6: Calculated electric field strength of two single nanowires with lengths $L_1 = 1036$ nm (green spectrum) and $L_2 = 656$ nm (blue spectrum) as well as a spectrum of a nanowire dimer formed by two wires having the lengths L_1 and L_2 (red line). The diameter for all wires is $D = 76$ nm and the gap of the dimer amounts to 12 nm. The colored vertical lines mark the peak positions.

In the red spectrum seven peaks are present. These peaks are enumerated by the red numbers. Their energies are compared to the ones of the two single nanowires: The first and the third peak in the red spectrum are slightly shifted to the red compared to the $l = 1$ and 2 peaks in the spectrum of the longer wire. The second peak is very slightly shifted to the red compared to the $l = 1$ peak of the shorter wire. The sixth and the seventh peak in the spectrum are at almost identical energies compared to the $l = 4$ mode of the longer wire and the $l = 3$ mode of the shorter wire, respectively. Finally, the $l = 3$ mode of the long wire and the $l = 2$ mode of the short wire are excited at almost identical energies. The fourth and the fifth peak in the dimer spectrum are slightly shifted to the red and to the blue, respectively, with respect to this energy.

To study these resonances in more detail, two-dimensional plots of the z -component of the electric field amplitudes are shown in Figure 9.7a-g. The excitation energies

are chosen to be the peak energies in the red spectrum (Figure 9.6). For each of the images, the color specifies the electric field strength and the images are independently scaled to obtain the best visibility. The plane is shifted by 15 nm in z -direction to the center plane of the structure. The dipole is located on the left.

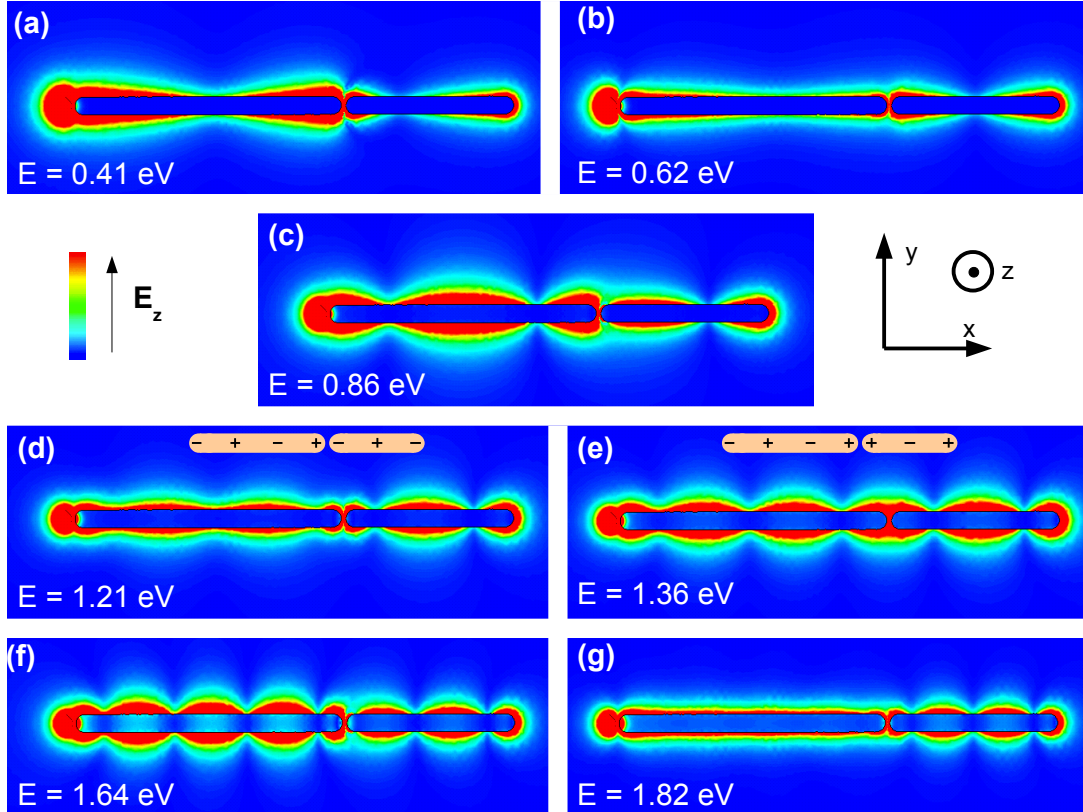


Figure 9.7: Calculated z -component of the electric field amplitude at the energies of the peaks in the dimer spectrum in Figure 9.6. The plane is shifted by 15 nm in z -direction to the center plane of the structure. The dipole is located on the left.

The three modes in Figures 9.7a,b and c reveal high field maxima only along one of the wires and much lower field maxima along the second. It is concluded that for these three modes the resonance condition between nanowire length and excitation energy is only fulfilled for one of the wires. The mode at $E = 0.41$ eV is thus assigned to the dipole mode in the longer wire, but is slightly shifted to the red compared to its intrinsic $l = 1$ resonance (compare red and green spectra in Figure 9.6). This is due to the attraction of negative and respectively positive charges located at opposite gap ends. The mode at $E = 0.62$ eV in Figure 9.7b reveals two intense maxima at the ends of the shorter wire. It is thus dominated by the excitation of the dipole resonance of this wire. As for the first mode, the energy is slightly shifted to the red compared to the intrinsic dipole energy of this wire. Following up this sequence, the mode at

$E = 0.86$ eV (Figure 9.7c) is assigned to the $l = 2$ mode of the longer wire. The redshift of this mode compared to the one of the single wire is less pronounced than for the $l = 1$ modes. This is explained by the decreasing electric field strength with increasing multipole order and thus decreasing interaction forces. In accordance to the observations made above, the sixth (Figure 9.7f) and the seventh modes (Figure 9.7g) are assigned to the $l = 4$ mode of the long wire and the $l = 3$ mode of the shorter wire, respectively.

In contrast to the other modes, at the energies 1.21 eV (Figure 9.7d) and 1.36 eV (Figure 9.7e) almost equally intense field maxima are visible along both wires. For both modes, four electric field maxima are located along the longer wire and three maxima along the shorter one. At 1.21 eV the field distribution is the one of a bonding mode, where positive and negative charge maxima are located at opposite gap ends. At 1.36 eV the charge distribution is the one of an antibonding mode. It is thus concluded, that since the $l = 3$ mode of the long wire and the $l = 2$ mode of the shorter wire are excited at almost identical energies (see blue and green spectra in Figure 9.6), they couple efficiently to each other, resulting in the splitting in a mode pair, consisting of a bonding and an antibonding mode. This is in analogy to what was found for the homodimers in Section 9.1, however in this case, hybridisation of multipole modes of different orders is found.

EELS-STEM measurements were performed to experimentally examine coupling between modes of different multipole order in heterodimers. Figure 9.8 depicts an EELS map of a nanowire dimer with similar dimensions as in the simulation, being $L_1 = 1036 \pm 10$ nm and $L_2 = 656 \pm 10$ nm. The diameter of both nanowires is $D = 76 \pm 5$ nm and the two nanowires are separated by a gap of about 12 nm. The nanowire was prepared using the identical synthesis parameters as for the wires in Section 9.1. After the dissolution of the middle segment, it was annealed at 300 °C for 30 min. The high-resolution plasmonic map consists of two scans, one along each of the two nanowires at a distance of ~ 15 nm. As visible in the map, the scan along the longer nanowire was not performed along the whole wire. The small bending of this wire at its end results in a very big distance of the scan line from the nanowire surface. At this distance the SP resonances are not resolvable.

In Figure 9.8b, three single spectra are shown exemplarily, the colored dots in the TEM image mark the positions of measurement. The colors of the dots adapt the colors of the corresponding spectra. Figure 9.7b demonstrates that the two spectra measured at the two ends of the dimer (blue and green curve) reveal peaks at different energies. In contrast, for the symmetrical dimer in Figure 9.1, one can see that the

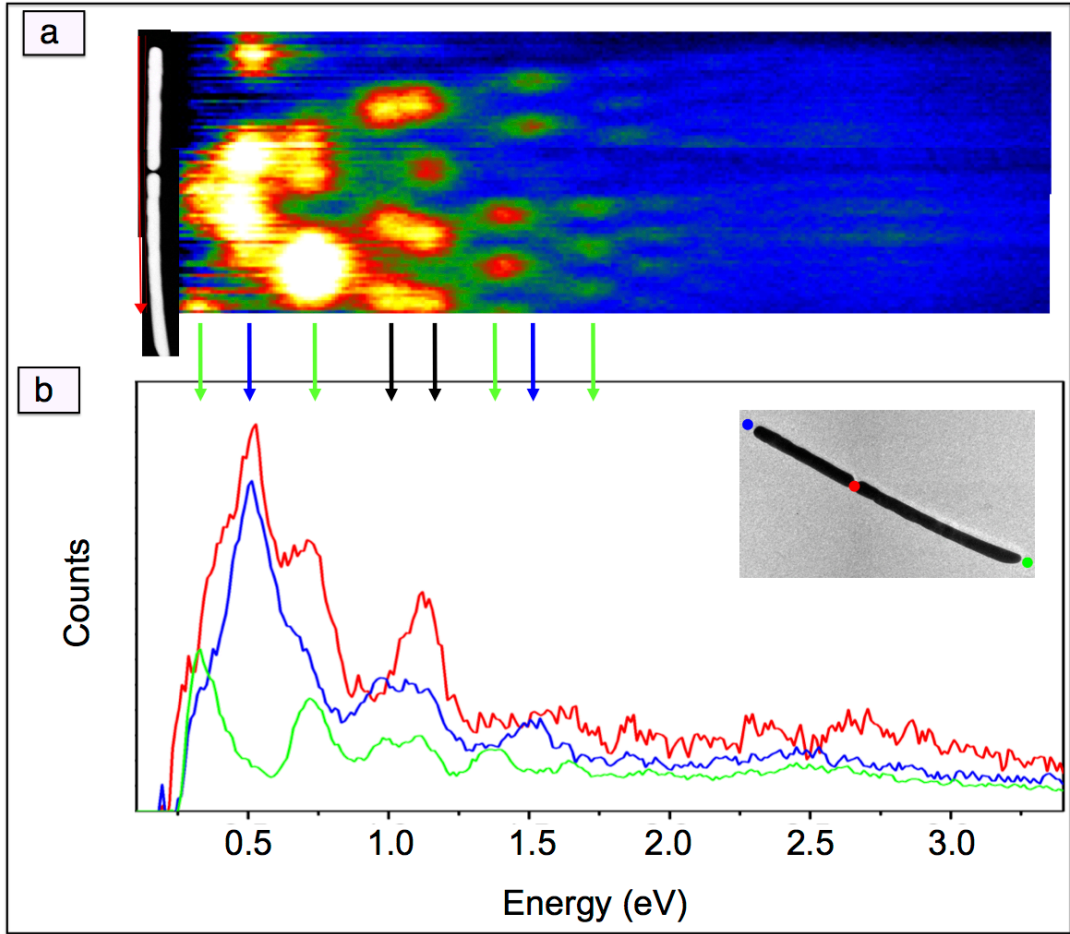


Figure 9.8: (a) Plasmonic intensity map of a nanowire heterodimer. The two wires have lengths $L_1 = 1036 \pm 10$ nm and $L_2 = 656 \pm 10$ nm, and diameter $D = 76 \pm 5$ nm, the gap width is ~ 12 nm. The map consists of 102 EEL spectra measured along the length of the red arrow in the TEM image on the left. The energy varies from left to right from 0.25 to 3.7 eV. The color indicates the number of counts. (b) Three spectra extracted from the intensity map in (a). The red curve shows a spectrum measured at the gap, the green spectrum is measured at the longer-wire end and the blue spectrum at the shorter-wire end. The three colored dots in the TEM image on the right mark the measurement positions.

two spectra measured at the two ends of the symmetrical dimer exhibit peaks at the same energies and have similar relative intensities.

The green spectrum in Figure 9.8b reveals two low energy modes at 0.33 ± 0.02 eV and 0.72 ± 0.02 eV, that are only weakly pronounced in the blue spectrum at the shorter wire end. They are assigned to two modes dominated by the intrinsic $l = 1$ and 2 modes of the longer nanowire. The most intense peak in the blue spectrum measured at the shorter wire end is resolvable at $E = 0.51 \pm 0.02$ eV. The map reveals at this energy two intense maxima, one in the middle of the structure and the other

one at the end of the short wire. From the map it is not possible to conclude if a maximum is excited at the longer wire end at this energy, however, the green spectrum reveals no peak at this energy. This mode is thus assigned to a mode dominated by the $l = 1$ dipole mode of the short wire. At the position of the gap (red spectrum) a broad peak, that consists of these three peaks, is visible.

Furthermore, at the energies $E = 0.98 \pm 0.02$ and 1.13 ± 0.02 eV two peaks are identifiable in both, the blue and green spectra. Along the nanowire they have the same number of maxima and very similar intensity. However, at the position of the gap only the higher energy peak is excitable. These observations are clear indications for degeneracy, and thus splitting into bonding and antibonding modes, for the $l = 2$ mode of the shorter wire and the $l = 3$ mode of the longer wire as observed in the simulation. We know that the bonding mode is not excitable when positioning the electron beam at the gap, while the antibonding mode is (*cf.* Section 9.1). Additionally, we find that the bonding mode maxima are shifted toward the nanogap, while the antibonding mode maxima are shifted slightly in opposite direction. This is in agreement to what was found for the symmetrical dimers in Section 9.1.

Indications for the mode coupling between the $l = 3$ mode of the long wire and the $l = 2$ mode of the short wire are found in simulation and experiment, although the resonance energies in simulation and experiment do not agree due to the previously discussed reasons (see Section 8). The ratio $\beta = 1.58 \pm 0.03$ of the dimer discussed here is deviating only slightly from the ratio $l_3/l_2 = 1.5$. In Section 8.1, a linear scaling law between the inverse of the resonance energy and the ratio of aspect ratio and multipole order was found. It was furthermore discussed that for nanowires with same diameter the identical scaling law can be applied. Thus, for two wires with same diameter and equivalent resonance energies for two different multipole orders l_a and l_b this proportionality results in:

$$\frac{AR_a}{l_a} = \frac{AR_b}{l_b} \quad (9.1)$$

$$\Rightarrow \beta = \frac{AR_a}{AR_b} = \frac{l_a}{l_b}. \quad (9.2)$$

AR_a and AR_b are the aspect ratios of the two nanowires. This yields that for a dimer with $\beta = 1.5$, the $l_a = 3$ and $l_b = 2$ modes are excited at the same energy and thus support mode coupling. The splitting into a bonding-antibonding mode pair for the dimer investigated here with $\beta = 1.58 \pm 0.03$ can be explained by the small deviations found for the linear relationship, the uncertainties in the wire dimensions, and the bending of the wire leading possibly to further shifts of the resonance energy.

This relationship is verified by two EELS maps of two more heterodimers in Figure

9.9. In (a), the dimer is formed by two wires with diameter $D = 100 \pm 10$ nm, and lengths $L_1 = 935 \pm 10$ nm and $L_2 = 573 \pm 10$ nm. The asymmetric gap has at its narrowest position a width of ~ 28 nm. The dimer in (b) has a diameter of $D = 110 \pm 10$ nm. The lengths of the two wires are $L_1 = 830 \pm 10$ nm and $L_2 = 645 \pm 10$ nm, the gap width is ~ 16 nm. In both cases the scans are performed at a distance of about 20 nm from the wire surface. In Figure 9.9a, a similar mode sequence as in Figure 9.8 is visible. The first three modes marked by black lines can be assigned to the $l = 1$ and 2 modes of the long wire, and to the $l = 1$ mode of the shorter wire. For these three modes, intensity maxima at both dimer ends are depicted. However, the first and third peaks are more intense along the longer wire end, while the second peak is more intense along the shorter wire. This is in good agreement with the simulation results (see Figure 9.7). Further, the $l = 3$ mode of the long wire and $l = 2$ mode of the short wire couple, resulting in the characteristic mode splitting into bonding and antibonding modes, which can be discerned by the missing peak at the position of the gap for the bonding mode. We notice that for this dimer exactly the identical multipole orders couple as in Figure 9.8. The two wires in Figure 9.9a have each very different aspect ratios than the ones in Figure 9.8. However, the ratio β between their aspect ratios is for this dimer $\beta = 1.63 \pm 0.03$ and is thus close to the one of the dimer presented above.

In contrast to Figure 9.8, in Figure 9.9a the bonding maxima are more intense along the long wire, while for the antibonding mode the maxima are more intense along the shorter wire. This can be explained with the help of the simulation: For the two individual nanowires, forming the dimer, the resonance energies were determined. While the simulation, in the case of the dimer in Figure 9.8, reveals that the $l = 3$ mode of the long wire and the $l = 2$ mode of the short wire are excited at the same energies within their error bars, in this case (Figure 9.9a), the energy difference between these two modes is 0.05 ± 0.02 eV. The intrinsic $l = 3$ mode of the longer wire is thus closer to the bonding mode, while the $l = 2$ mode of the shorter wire is closer to the antibonding mode, which accounts for the differences in intensity of the maxima. This result is accordant to previously published calculation results. Slaughter et al. theoretically investigated the dipole modes of heterodimers with β ranging from 1.0 to 1.5.¹⁴¹ They find for the heterodimers a more dominant dipolar bonding mode in the longer wire, and a more dominant antibonding mode in the shorter wire. In their case, coupling of modes of identical multipole order was investigated. Here, similar results for the coupling of different multipole modes are presented.

Figure 9.9b depicts a scan along a dimer with $\beta = 1.29 \pm 0.03$. This value is

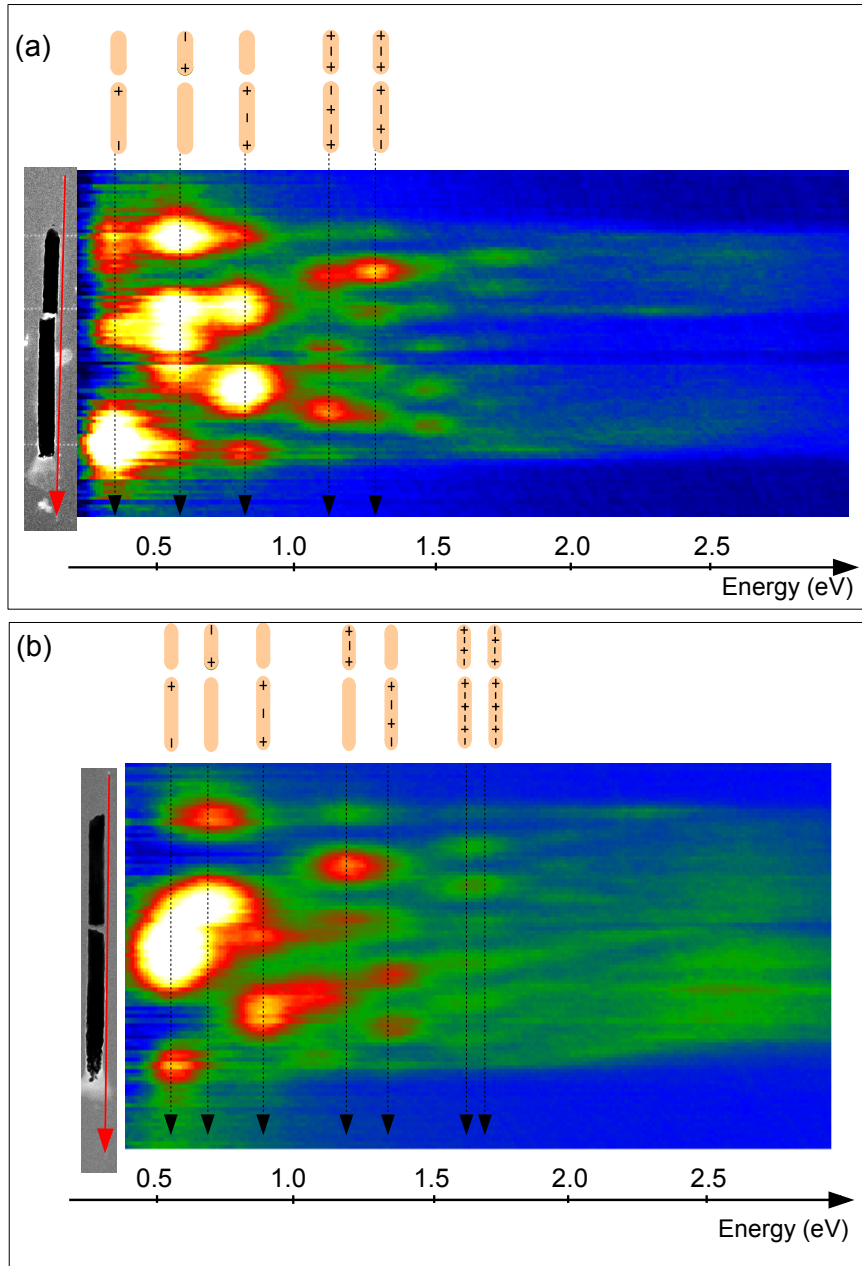


Figure 9.9: (a) EELS scan consisting of 100 spectra along a nanowire heterodimer with $D = 100 \pm 10$ nm and $L_1 = 935 \pm 10$ nm and $L_2 = 573 \pm 10$ nm and gap size of ~ 28 nm. (b) Scan consisting of 100 spectra along a heterodimer with $D = 110 \pm 10$ nm. The length of the two wires are $L_1 = 830 \pm 10$ nm and $L_2 = 645 \pm 10$ nm, the gap has a width of ~ 16 nm.

smaller than β of the two above discussed dimers. It is however in the range of the heterodimers discussed in Ref. 141, supporting coupling of dipole modes of the two wires. In our case, splitting into bonding and antibonding modes is not resolvable for the two dipole modes. A possible explanation for this is the higher aspect ratios of the

wires discussed here. In this case the resonances are narrower, which most probably results in mode degeneracy only for smaller energy differences. It is $l_4/l_3 = 1.33$, which is close to β of this dimer, resulting in the coupling of the $l = 4$ and $l = 3$ mode of the two wires. Since the peak intensities as well as the interaction forces decrease with multipole order, this is only very weakly resolvable in Figure 9.9b. However, an indication for the degeneracy, being the missing peak at the position of the gap at the bonding mode is visible.

9.3 Conductively coupled nanowire dimers

As discussed in Section 4.2.2 conductively coupled nanowires can be synthesized by sequential deposition of $\text{Au}_{60}\text{Ag}_{40}/\text{Au}_{15}\text{Ag}_{85}/\text{Au}_{60}\text{Ag}_{40}$ segments and incomplete dissolution of the Ag segment. In this section, we present experimental and theoretical results on the plasmonic properties of conductively coupled nanowire dimers, discussing in particular the interesting and systematic variation of the SP resonances when the nanostructure varies from a continuous wire to two nanowire dimers coupled by junctions of decreasing size to finally uncoupled nanowires separated by a nm-sized gap.

As in the previous section, the analysis is started with simulation results of conductively coupled nanowire dimers, with similar dimensions as the synthesized structures. Secondly, the EELS-STEM measurements of their SP resonance energies are presented.

Figure 9.10 shows simulations of the electric field strength (CST Microwave Studio) of four different Au nanostructures: a continuous wire with length 1145 nm and diameter 90 nm (black line), and three nanowire dimers, each consisting of two wires with length 563 nm and diameter 90 nm. The dimers are either separated by a 19 nm gap (red line), or conductively coupled via a cylindrical Au junction with length $l_c = 19$ nm and diameter $d_c = 40$ nm (blue line) or 20 nm (green line). The resonances are excited by a dipole, located at a distance of 10 nm from one end of the structure. The spectra show the absolute value of the electric field strength measured at a distance of 1 nm from the opposite end of the structures. The simulation parameters are specified in Section 7.2. The impedance of the dipole is in this case $5 \text{ k}\Omega$.

In contrast to the structures in the previous sections, in this section, the structures are modelled having planar ends with slightly rounded edges, to obtain the best agreement between the simulated and the experimentally investigated wires.

The four spectra are shifted vertically for clarity. The surface charge distributions of the different SP resonances are depicted schematically for a continuous wire (top)

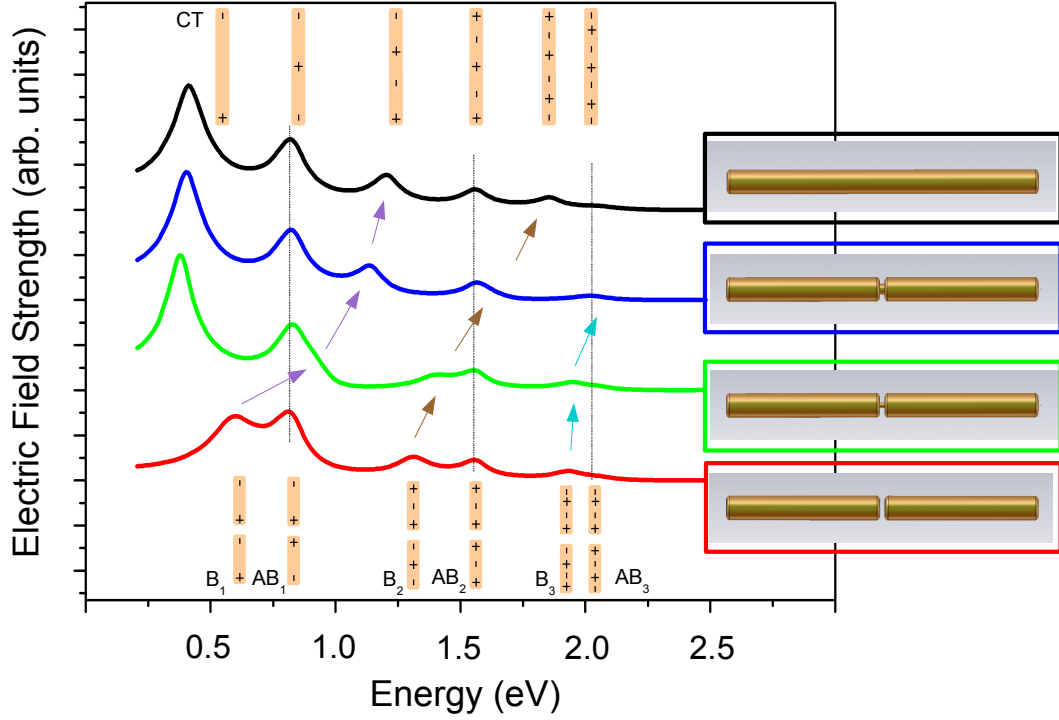


Figure 9.10: Absolute value of the electric field strength versus excitation energy for four different structures: a continuous wire with length 1145 nm (black line), a conductively coupled dimer with connection of length 19 nm, and diameter 40 nm (blue line), a second conductively coupled dimer with same connection length, but decreased connection diameter 20 nm (green line) and a capacitively coupled dimer with gap 19 nm (red line).

and for the capacitively coupled dimer (bottom). These charge distributions were obtained from calculations of the electric field at the corresponding SP resonance energies. Exemplarily, Figures 9.11 a-f display two-dimensional plots of the electric field z -component for the dimer with a junction of 20 nm diameter (green line in Figure 9.10). In addition, in Figure 9.10, schemes of the structures are depicted to the right of each spectrum. Figure 9.10 demonstrates that for all four structures resonances are excited at 0.82 ± 0.02 , 1.55 ± 0.02 and 2.03 ± 0.02 eV (vertical dashed lines). At these energies, the resonances of all four structures have a symmetric field distribution with respect to the center of the wire. In the case of the capacitively coupled dimer, we have identified these resonances in Section 9.1 as antibonding modes (red spectrum). However, in the case of the single nanowire (black spectrum), these modes were assigned to the dark modes with multipole order $l = 2, 4$, and 6 . Our results demonstrate that the energies of these modes deviate by only less than 0.04 eV for different junction sizes, and that the symmetry is maintained for all four structures.

Figure 9.10 reveals for the dimer three further resonances, known as the bonding modes of different multipole order. Modes with the same number of electric field maxima and similar field distribution as for the bonding modes are found as well in the spectra of the two connected wires and the continuous wire. They are, in the case of the continuous wire, assigned to the bright modes $l = 3$ and 5. We identify a clear blueshift of these resonances with increasing connection size, which is indicated by the arrows in Figure 9.10. The blueshift is explained by the decreasing coupling strength between the modes of the two individual wires with increasing junction size. Calculations for two conductively connected gold nanoshells revealed the blueshift of the dipolar bonding mode with increasing conductance and junction size.^{142,143} Here, the blueshift is demonstrated additionally for higher modes up to third order. Our analysis shows that resonances with similar asymmetric field distribution and the identical number of maxima are expected for all structures, and that the resonance energy shifts to the blue with increasing junction size. In the case of the lowest multipole order, the shift to the blue of the resonance energy is even bigger than 0.6 eV.

Comparing spectra of the dimer with the gap (Figure 9.10, red line) and the conductively coupled dimer ($d_j = 20$ nm, green line), it becomes evident that the shift to the blue of the bonding modes when introducing a conductive junction is different for the first and second order resonances. In Ref. 142 the authors reported that the shift of the B_1 -mode to higher energies occurs, when the conductivity of the junction equals a certain threshold that allows the charges at the junctions to neutralize faster than the oscillation period of the corresponding SP mode. This implies that the conductivity threshold of the junction increases with the SP frequency. Thus, for a given junction (*e.g.* $d_c = 20$ nm, green line), the shift in energy for the bonding modes depends on the mode order (*i.e.* on the mode frequency), the blueshift being the largest for the B_1 -mode, and decreases with mode order. In addition, the bigger the junction size, the higher is its conductivity, and thus the larger should be the shift for a given resonance energy. Interestingly, this shift of the resonances results in a mode rearrangement depending on the junction diameter. See for example the green spectrum, where the AB_1 -mode is lower in energy than the B_1 -mode, while in contrast the AB_2 -mode is higher than the B_2 -mode.

The resonance of lowest energy in the spectrum of the continuous wire is the charge transfer (CT) mode. In Section 8.1 it has been named the dipole mode of a single wire. This mode is as well visible in the two spectra of the connected wires. It possesses a net charge in each of the two connected wires. Therefore, it can only be excited for

the dimers if charge transfer between the two wires is possible.^{119,142,144} Thus, the CT-mode does not exist for the capacitively coupled dimer system (red line). For the two connected dimers, the CT-mode reveals a weak blueshift with increasing junction width (from 0.38 ± 0.01 to 0.40 ± 0.01 eV). For the continuous wire, the corresponding CT-mode is further shifted to the blue (0.41 ± 0.01 eV). This shift is assigned to the increased conductivity of the junction.

Figure 9.11 shows the calculated two-dimensional plots of the electric field z -component for the nanowire dimer with the junction diameter $d_j = 20$ nm at the energies (a) 0.38, (b) 0.83, (c) 0.91, (d) 1.40, (e) 1.55 and (f) 1.95 eV. The color depicts the z -component of the electric field at each position and is for each image arbitrarily scaled to optimize visualization of the maxima. The plane is shifted in z -direction by 8 nm to the centre plane of the structure. The dipole is located on the right of the structures. It is responsible for the high electric field (indicated by the red color) at this position. The electric field distributions are assigned to the SP modes resolved in Figure 9.10. For the antibonding modes at 0.83 and 1.55 eV, a broad maximum is visible at the structure center, while the three bonding modes (0.91, 1.40, and 1.95 eV) reveal two distinct maxima, one at each side of the nanowire ends close to the connection. The CT-mode at 0.38 eV does not have a maximum at the nanowire center.

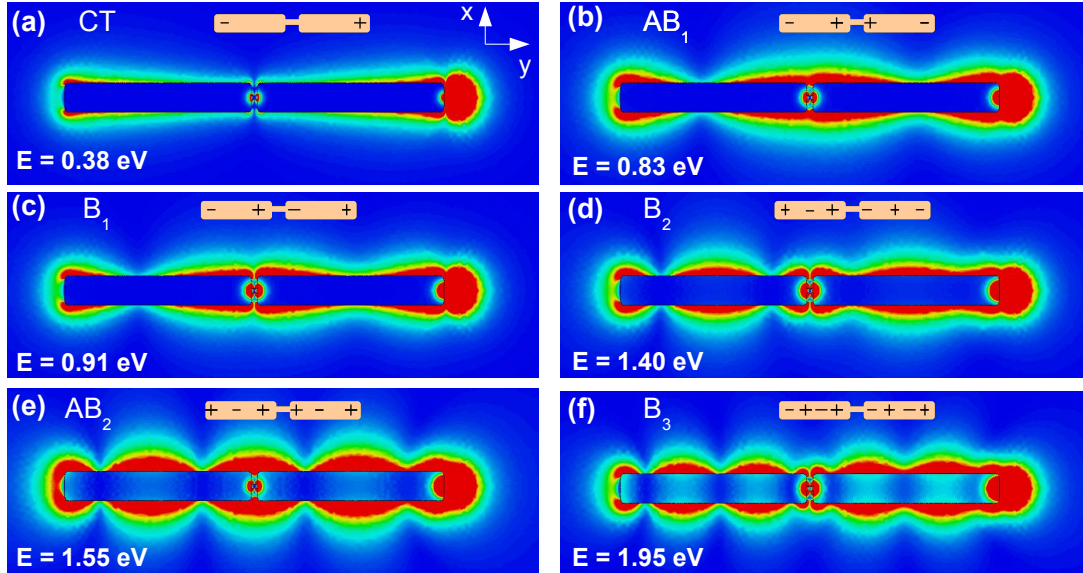


Figure 9.11: Electric field component in the direction perpendicular to the depicted plane (z -direction) in proximity to nanowire dimer with small connection of diameter 20 nm. The depicted plane is shifted by 8 nm in z -direction. Red and blue color indicate high and low electric field, respectively. The excitation dipole is located to the right of the structures and is responsible for the high electric field (indicated by the red color) at this position.

As clearly visible in Figure 9.10, the energies of the antibonding resonances of the nanowire dimer structure do not shift significantly when adding conductive junctions of various sizes. Figure 9.12 shows the calculated two-dimensional plots of the electric field for the AB₂-mode of the dimer with thin connection (Figure 9.12a) together with the AB₂-mode of the continuous wire (Figure 9.12b). For comparison, the field distributions for the B₂-mode of the conductively connected dimer (1.40 eV) and the continuous wire (1.86 eV) are shown in Figures 9.12c and 9.12d. These figures depict the center plane of the structure and the arrows indicate the direction of the electric field. The colors of the arrows indicate the strength of the electric field and are for each image independently scaled to obtain the best visibility. The details on the right show the region of the gap with higher resolution. In Section 9.1 it was already demonstrated that for the antibonding modes of capacitively coupled dimers the field in the gap is low, while for the bonding modes it is high. Here, we obtain a similar result for the bonding and antibonding modes of the conductively coupled wires. Furthermore, it is shown that for the AB₂-mode the field distribution is almost identical to the one of the continuous wire (Figure 9.12b) independent of the junction size. This is also observed for the AB₁- and AB₃-modes (not shown in the figure). In contrast, for the B₂-mode at 1.40 eV the high electric field in the gap (Figure 9.12c) leads to a spatial shift of the electric field maxima in the direction of the structure center, compared to the position of the maxima of this mode for the continuous wire (Figure 9.12d). In Section 9.1 it was already demonstrated that these shifts depend on the gap size. Here, it is furthermore found that they also depend for the conductively coupled dimers on the junction size. The energy shifts of the bonding modes with connection size are thus attributed to the varying spatial field distributions. The antibonding modes, that have almost identical field distributions, are little shifted in energy. It is concluded that the junction only influences SP resonances, if a field is concentrated at the gap.

Similar conductively coupled nanowire dimers as simulated with CST could be synthesized by electrodeposition of Au₆₀Ag₄₀/Au₁₅Ag₈₅/Au₆₀Ag₄₀ nanowires and dissolving the middle segment (*cf.* Section 4.2.2). As presented in Section 4.2.2, not all middle segments are completely dissolved and EELS-STEM measurements were performed on these conductively connected nanowires to confirm the simulation results.

The TEM image in Figure 9.13a shows a conductively coupled nanowire dimer with total length 1145 ± 10 nm and diameter of 90 ± 10 nm. Unfortunately, the exact dimension and morphology of the junction can not be determined from the TEM image. On the right side of the TEM image, a SP-EELS map is shown. The map consists of 100 spectra measured along the wire axis, at approximately 15 nm distance

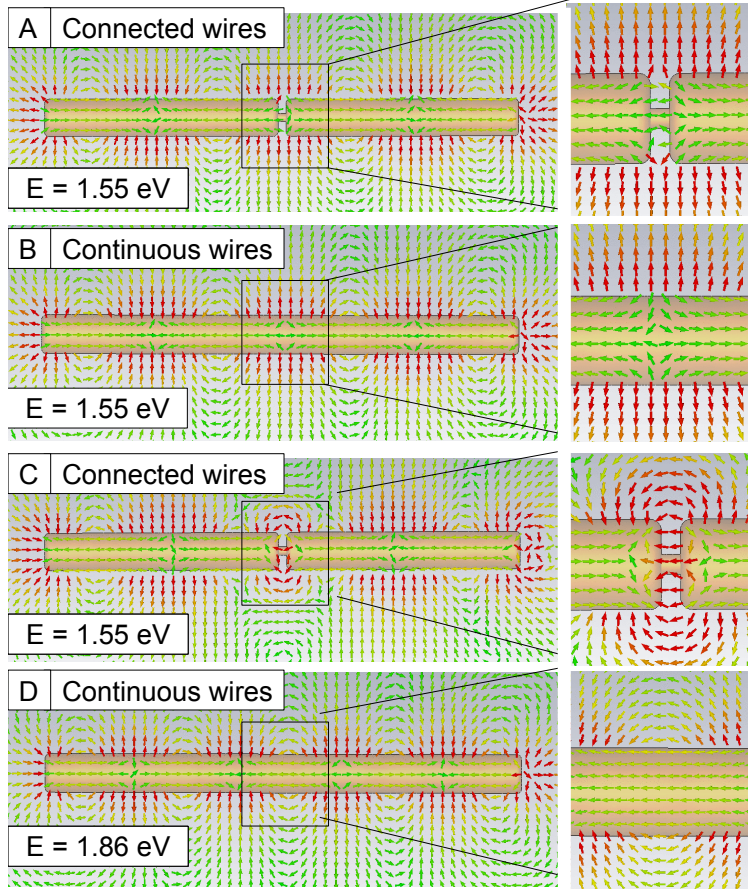


Figure 9.12: Calculated electric field for the AB_2 -mode of dimer with thin connection (a) and $l = 4$ -mode of continuous wire (b), together with the electric field corresponding to the B_2 mode of connected dimer (c) and $l = 5$ -mode of continuous wire (d). The direction of the arrows and the color depict the direction of the field and its strength. The image details displays the center region with higher resolution.

from the nanowire surface (red arrow). Each horizontal line corresponds to one EEL spectrum measured at a specific position along the nanowire axis. From left to right, the energy loss varies from 0.25 to 3.0 eV, and the color in the map indicates the number of counts. Figure 9.13b shows two exemplary spectra extracted from the map at two different positions, close to the junction (red line), and close to one of the dimer edges (green line). The positions are indicated by the respective red and green dots in the TEM image on the right.

We can resolve in the map seven different longitudinal SP modes that we attribute to the SP modes identified in the simulations. Their corresponding electric field distributions are represented schematically on top of the map.

The CT-plasmon is located at an energy of 0.33 ± 0.02 eV and reveals the two

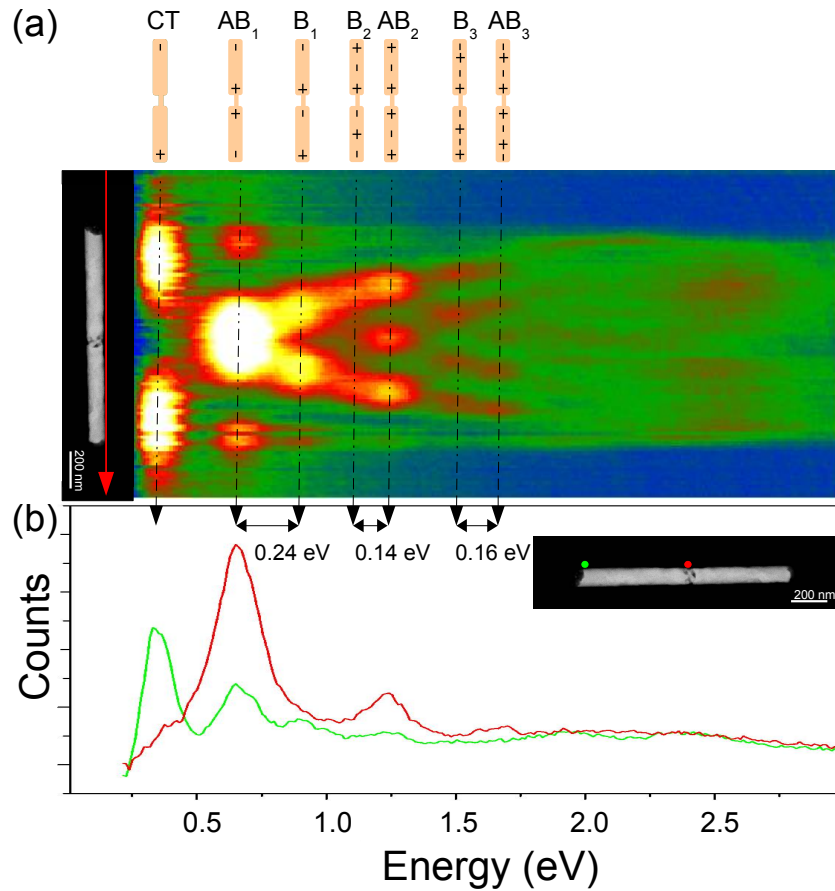


Figure 9.13: (a) Plasmonic EELS map of a nanowire dimer. The wires are connected by a conductive junction. The map consists of 100 EEL spectra that are measured along the red arrow in the TEM image on the left. The energy varies from left to right from 0.25 to 3.0 eV. The color indicates the number of counts. (b) Two spectra extracted from the intensity map in (a). The red curve shows a spectrum extracted from the middle of the map, while the green curve represents a spectrum extracted from one end of the structure (see red and green dots in the TEM image).

characteristic intensity maxima at the two ends of the structure. The next two low-energy peaks can be attributed to the AB_1 - and B_1 -modes. In this case, the B_1 -mode has a higher energy than the AB_1 -mode. In contrast, the B_2 - and B_3 -modes are lower in energy than the AB_2 - and AB_3 -modes, respectively. These experimental results are in very good agreement with the simulations presented for nanowire dimers. It is important to notice that for the B_2 - and B_3 -modes, using EELS in a TEM, the maxima in the middle of the structure are not excited. This is due to the fact that the electron beam cannot excite an antisymmetric mode when placing the beam very close to the center of the structure (see Section 9.1). For the B_1 -mode, the two maxima

are not excited exactly at the center of the structure either. However, we can resolve these two maxima slightly away from the dimer centre. We attribute this to the fact that for the low-order modes the maxima extend over a broader space than the ones of the high-order modes (see Figure 9.13).

Comparing the energy difference of the B₂- and AB₂- mode pair to that of the B₃- and AB₃-mode pairs, we observe that it is larger for the second pair, which again agrees well with the simulation results. This is in contrast to the dimers with small gaps, where decreasing energy differences between bonding and antibonding pairs with increasing multipole order have been measured (*cf.* Section 9.1).

Figure 9.14a shows the spectra of two conductively coupled nanowire dimers with similar aspect ratio, being $L/D = 13.1$, but different junction diameters. The dimensions of the two dimers are $L = 1145 \pm 10$ nm and $D = 90 \pm 10$ nm (Figure 4a, blue line) and $L = 1490 \pm 10$ nm, $D = 115 \pm 10$ nm and $d_j = 30$ nm (green line), respectively. In contrast to all other wires presented here, this second dimer (green line) was annealed at 300° C for half an hour. It was found that this procedure reduces the Ag content very slightly by about 5%.

For both structures, their antibonding modes are excited at very similar energies, marked with dashed black lines on the spectra. For the blue spectrum, the AB₃-mode is not resolvable, however, its energy could be measured in Figure 9.13 and is additionally marked in the blue curve. The small deviations for the antibonding modes of the structures can be attributed to small deviations in aspect ratio, Ag content, and shape of the wires.²⁵ In contrast to these modes, the energies of the CT- and B₁-modes deviate much stronger, supporting the finding that the size of the junction does only weakly influence the antibonding mode energies, while the CT-mode and the bonding modes depend clearly on its size. As expected, in the two spectra the CT-mode and the B₁-mode of the structure with smaller junction have lower energies.

Figure 9.14b shows the spectra of two conductively coupled nanowire dimers with different aspect ratio. For one dimer, it is $AR = 20 \pm 3$, $L = 1510 \pm 10$ nm, $D = 75 \pm 10$ nm, and $d_j = 15$ nm (red line). For the second dimer (same as in Figure 9.14a (green line)), $AR = 13.1$, $L = 1490 \pm 10$ nm, $D = 115 \pm 10$ nm and $d_j = 30$ nm (green line). TEM images of the wires are depicted on top of the spectra and the colored dots mark the measurement positions. The energies of all resolvable longitudinal modes in the red spectrum are shifted to the red compared to the resonance energies in the green spectrum due to the larger aspect ratio of this wire. The energy difference between the B₁- and AB₁-modes is in this case bigger than the one in the spectrum of the wire with smaller aspect ratio, although its junction is slightly smaller. This is due

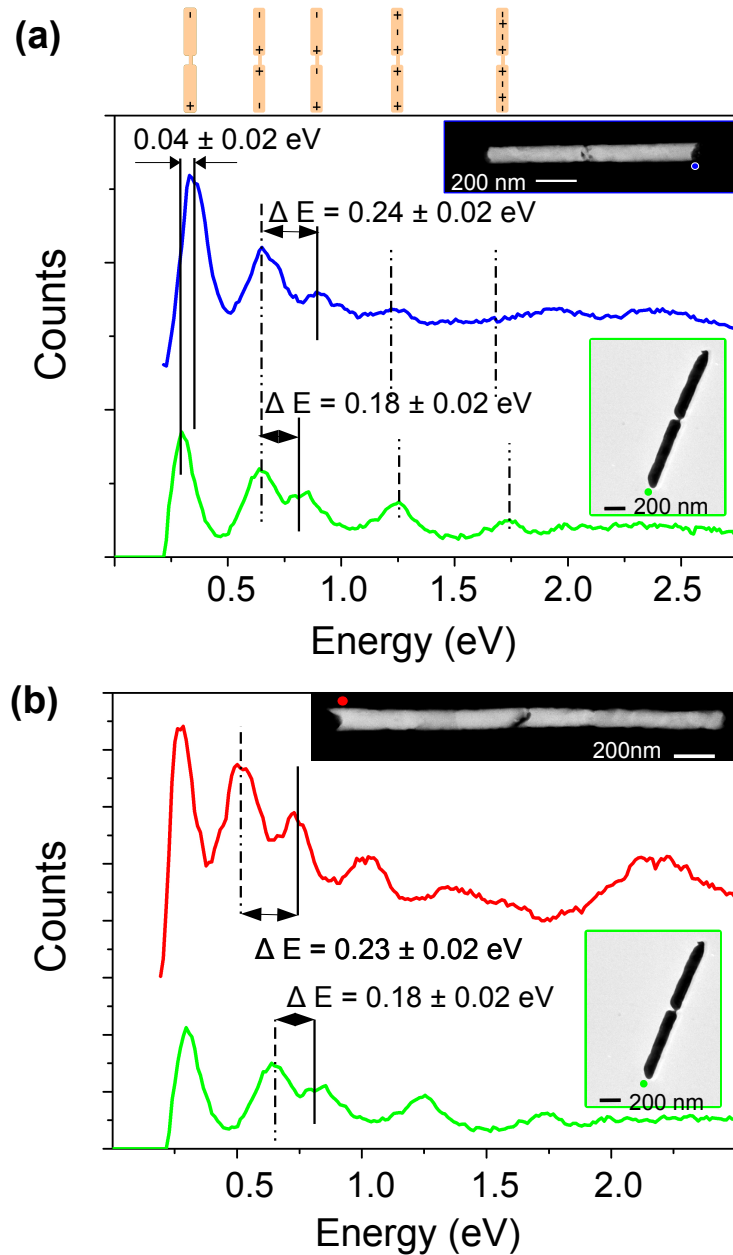


Figure 9.14: Spectra of conductively coupled nanowire dimers with small junctions. (a) The blue line corresponds to a spectrum of the nanostructure in Figure 9.13, the green line represents the spectrum of a nanowire dimer with a junction of thickness 20 nm. Both wires have similar aspect ratio L/D of 13 ± 1 . (b) The red spectrum corresponds to a coupled dimer with $AR = 20 \pm 1$ and a junction diameter of ~ 15 nm. The green line depicts the same spectrum as in (a). All spectra are measured at the positions of the colored dots in the TEM images.

to a decreased conductivity threshold with decreased resonance energy, as discussed above. Remarkably, a broad peak, centred at an energy of about 2.2 eV, is resolved

in the spectrum of the dimer with larger aspect ratio. This peak is not visible in the spectrum of the dimer with smaller aspect ratio. It is most probably due to a transversal mode of the structure. The fact that the transversal mode is only visible in the red spectrum can be understood from the different excitation positions indicated by the colored dots in the TEM images, indicating that the transversal modes can be excited parallel to the nanowire (red dot), but not along the continuation of the axis beyond the wire (green dot).

After the Ag dissolution process, conductive junctions were found at different positions with respect to the nanowire axis. The conductive junctions in Figure 9.14b are for example not centered. We have simulated the influence of the relative position of the conductive junction on the SP resonances. Figure 9.15 shows two spectra that were calculated for a dimer coupled conductively by a junction with $l_j = 19$ nm and $d_j = 20$ nm, placed either at the center (black line) or at the side (red line) between the two identical wires. The length and diameter of the complete structures are $L = 1145$ nm and $D = 90$ nm. The antibonding modes are excited at the same energies in both spectra. The low electric field at the position of the gap for the antibonding mode results in similar field distributions for both structures independent of the connection position. However, the resonance energies of the bonding modes differ slightly, being excited at higher energies for the structure connected in the middle. This demonstrates that not only the size, but additionally also the positioning of such a junction determines the bonding mode resonance energies.

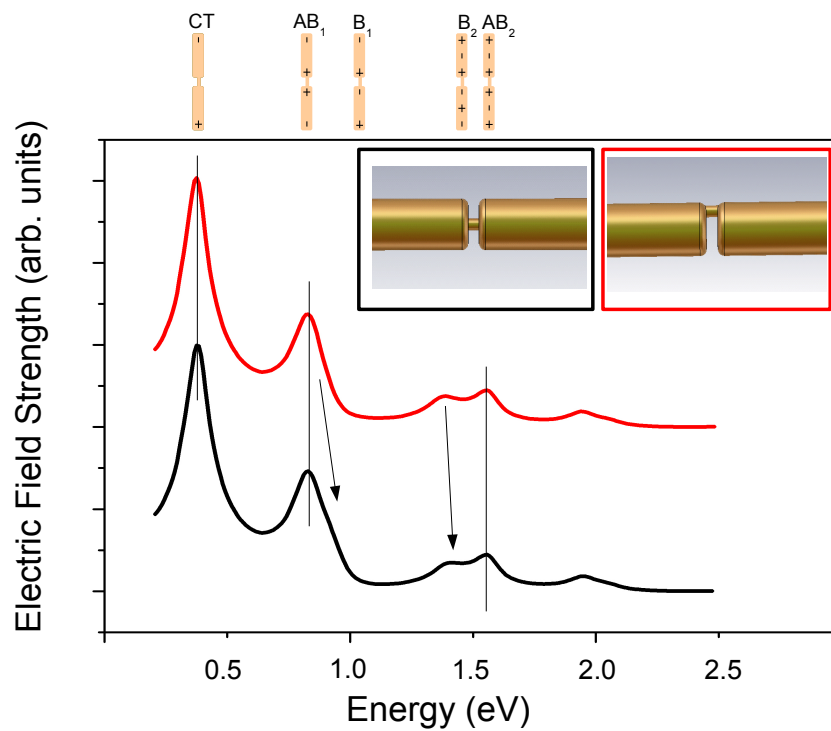


Figure 9.15: Calculated spectra of two nanostructures each consisting of conductively coupled nanowires with the same aspect ratio. The junction has in both cases the same diameter $d_j = 20$ nm and length $l_j = 19$ nm. The black spectrum corresponds to a structure where the junction is located exactly in the middle of the structure while the red spectrum corresponds to a structure with junction shifted to the edge of the gap. The insets display the geometrical arrangement schematically.

Chapter 10

Conclusions and Outlook

Multipole surface plasmons in single nanowires

We have presented investigations by EELS-STEM of the SP resonances of Au and smooth and porous AuAg nanowires, that constitute an excellent complement to light microscopy measurements. EELS-STEM measurements feature a unique spatial resolution of few nanometres, a high energy resolution (120 meV), as well as the possibility to excite bright and dark modes. The experimental results are confirmed by finite element simulations using CST Microwave Studio.

While other SP methods mostly analyse the dipole resonance, we have investigated multipole resonances up to fifth order, including both bright and dark modes. Dark modes can be excited only with difficulty by light microscopy due to the missing net dipole moment of these modes. Information on the dark resonance energies of a structure is important for their application as a platform for light guiding mechanisms without radiative losses.^{14,15}

Our results show that the multipole SP modes decrease in resonance energy with increasing nanowire length and decreasing nanowire diameter. Comparison between calculations with CST Microwave Studio and experimental results reveals only small deviations in the resonance energies. We attribute these deviations to surface roughness, the shape of the wire ends, and the frequency dependence of the dielectric function of Si₃N₄. However, all general relations found for the experimentally determined resonance energies are confirmed by the simulation. We conclude thus that the simulation is a very helpful tool to investigate SP resonances although a small blueshift of the calculated resonances is found compared to the measured ones.

Furthermore, our results reveal that for multipole modes of orders higher than two a linear relationship between $1/E$ and AR/l can be assumed, where axis intercept

and slope are constant for constant nanowire diameters. This relation is useful for applications since resonance energies of multipole modes can be easily calculated if resonance energies of a nanowire with identical diameter are known.

EELS-STEM measurements on pure Au wires and annealed AuAg wires together with the corresponding CST calculations show that the longitudinal resonance energies of an annealed AuAg wire are shifted to the blue compared to the ones of a non-annealed, pure Au with same length and diameter. However, it remains unclear if this redshift is explained by the Ag content or by a smoothening and rounding of the nanowire ends caused by the annealing of the wires. The blueshift of the transversal mode is higher than the one of the longitudinal modes. This is explained by the Ag content in agreement with previously reported results on nanoparticles.¹³⁵ Our analysis shows the great potential of the EELS-STEM measurements to explore the influence of parameters such as surface roughness and end shape. However, the broad range of parameters that may influence the resonance energies render the analysis very difficult. Further measurements are necessary to investigate the distribution of Au and Ag atoms in the nanowires, and to discern the influence of Ag content and annealing of a wire.

The comparison between the measurements and the simulation reveals that the SP resonances of porous AuAg wires shift to the red compared to their smooth Au counterparts for $l = 1$ to 4. We interpret this redshift as an effective length increase of the wire due to the increased surface area.

Finally, we determined from the EELS-STEM analysis the dispersion relation for a pure Au nanowire, a smooth AuAg alloy nanowire and a porous AuAg alloy nanowire. For the Au and the smooth AuAg wire with similar diameter we found very similar curves, having a similar shape as the dispersion relation for plasmons propagating on a planar interface. The curve obtained for the porous nanowire reveals a shift to lower energies, which we again assign to the increased surface area that was not taken into account in the analysis.

Multipole surface plasmons in nanowire dimers

Additionally, we presented results of EELS-STEM measurements of the multipole SP resonances of capacitively and conductively coupled nanowire dimers that were synthesized by electrodeposition of segmented Au-rich/Ag-rich/Au-rich segments and subsequent etching of the Ag-rich segment. The high spatial resolution of EELS-STEM is used to discern the influence of gap size, connection size, and dimer symmetry on

the plasmonic properties of the nanostructures.

Capacitive coupling of SP modes in nanowire dimers is characterized by mode degeneracy, resulting in a splitting into a bonding and an antibonding mode. The high energy resolution, achieved by EELS-STEM, allowed us to resolve this in the measurements for the first time for multipole orders up to three in several dimers. We studied the energy difference between bonding and antibonding modes for capacitively coupled nanowire dimers with various geometries and gap sizes. For each of the dimers, a decreasing energy difference between bonding and antibonding pairs is resolvable with increasing multipole order. Furthermore, we found for the spatial field distribution along the nanowire dimers that maxima of bonding modes shift in the direction of the gap, while maxima of antibonding modes shift in opposite direction. The comparison of our experimental results to CST microwave simulations revealed that a high field is concentrated in the gap only for bonding modes, resulting in the gap size dependent spatial shift of the maxima.

Beside the capacitively coupled nanowire homodimers, we also synthesized heterodimers and characterized them as well by TEM-EELS. The results are compared to CST simulations. For very asymmetric dimers (β between 1.33 and 1.62), we found that the modes of different multipole order split into bonding and antibonding mode pairs.

This observation reveals the potential of the heterodimers for applications: Coupling of plasmon modes of differing multipolar order can result in a Fano resonance.^{145–147} Such a Fano resonance is promising for sensorics as it will be discussed in the Outlook.

Finally, our synthesis method reveals also the potential to create conductively coupled nanowire dimers. Such structures are obtained if the dissolution of the Ag-rich part is not complete and small metallic bridges connect the nanowires. We investigated the plasmonic properties of these conductively coupled nanowire dimers. Our results show that the bonding modes of the dimers shift to the blue with increasing connection size. The mode shifts continuously with connection diameter between the bonding mode of the capacitively coupled dimer and a bright mode of a single nanowire with similar dimensions. The bright mode of the single wire has the identical number of field maxima compared to the bonding mode, however we found that the spatial position of the field maxima along the structure varies. Performing simulations we found that the maxima are shifted in the direction of the gap with decreasing connection size. We attribute this shift to the high electric field excited at the position of the gap. In contrast, the antibonding modes of the dimers are almost independent of the connection size. In their case, the resonance energy and the position of the field

maxima is only very weakly influenced by the connection.

Outlook

From the results presented in this work, it is clear that single metallic nanowires and nanowire dimers synthesized by pulsed electrodeposition and subsequent etching of the Ag-rich segments possess a high potential for applications. The results demonstrated that the SP resonance frequency can be tuned by controlling various nanowire parameters, namely dimensions, composition, surface roughness, porosity, and gap size. In the future, the potential will be explored to apply single nanowires and nanowires dimers synthesized and studied in this work for surface enhanced infrared spectroscopy (SEIRS) and for surface enhanced Raman spectroscopy (SERS) will be explored.

For SEIRS, the SP resonance of the dipole mode of the single nanowires or the dipolar bonding mode of the dimers have to be precisely tuned to the infrared absorption wavelength of the molecule under investigation. Recently, SEIRS measurements on single nanowires have been reported.^{4,5} As probe molecule served octadecanethiol (ODT). A monolayer of ODT was adsorbed on the surface of the wires and the corresponding infrared spectra were measured. Enhancement factors of five orders of magnitude were found for single Au nanowires. This has proven that SEIRS on Au nanowires is an efficient method for lowering the detection limit of IR vibration spectroscopy.

In the future, it is planned to apply Au nanowires and AuAg alloy nanowire dimers of this work for continuative measurements, to further increase the enhancement factor and explore the sensitivity of the enhancement to the different nanowire parameters. The good agreement between the experimental and the simulation results especially for the dipole mode that is presented here qualifies calculations with CST Microwave Studio as a suitable method to estimate the required nanowire dimensions to obtain a specific resonance wavelength, being in agreement with the infrared absorption wavelength of ODT. After the SEIRS measurements, the nanostructures would be monitored in the SEM and the infrared spectroscopy results would be compared to those of the EELS-STEM measurements to investigate the influence of nanowire end shape, gap size, and surface morphology on the enhancement factors. First tests have shown that using the Si_3N_4 membranes or lithographically marked diamond substrates, it is possible to relocate the identical nanostructures using the different analysis methods.

In a second approach, the nanostructures would be applied as substrate for SERS. For this experiment, the SP resonance wavelength has to be adjusted to the Raman

laser wavelength. Thus, also tailoring of the nanowire parameters is required. In contrast to the SEIRS measurements, Raman lasers work usually with ultraviolet, visible or nearinfrared wavelengths. It is thus crucial to investigate the enhancement factors for SERS not only of the dipole mode but also for the multipole modes depending on the different nanowire parameters.

As mentioned in the conclusion sections, especially the nanowire heterodimer are interesting platforms for sensorics since coupling of a multipolar modes of differing order can result in the generation of a Fano resonance, especially if one of the modes is a narrow dark mode and the other one a broad bright mode. Such a resonance can be characterized by a very narrow width. It has been shown previously for a core shell particle that the Fano line shape is modified and the resonance shifts very sensitively with changes of the permittivity of a dielectric material filling the cavity.¹⁴⁵ These SP resonance-based sensors can be of tremendous interest for biosensing and medical applications. An example is their use for diagnosis of Alzheimer's disease. It has been shown for triangular nanoparticles that this SP resonance shifts significantly in the presence of a biomarker that is associated with Alzheimer's disease.¹⁴⁸ First results show that these shifts are concentration dependent and allow the detection of the biomarker at low concentrations.

The large electric field strength excited in the gap region of a dimer and the potential to excite a Fano resonance characterize the nanowire heterodimers investigated here as promising to further enhance the detection sensitivity to such biomarkers. This would be a crucial step for the development of a biosensor for early detection of Alzheimer's disease.

Bibliography

- [1] M. Moskovits, “Surface-enhanced Raman spectroscopy: A brief retrospective”, *J. Raman Spec.* **36**, pp. 485–496 (2005).
- [2] K. Kneipp, Y. Wang, H. Kneipp, L. T. Perelman, I. Itzkan, R. R. Dasari, and M. S. Feld, “Single molecule detection using surface-enhanced Raman scattering (SERS)”, *Phys. Rev. Lett.* **78**, pp. 1667–1670 (1997).
- [3] S. Nie, “Probing single molecules and single nanoparticles by surface-enhanced Raman scattering”, *Science* **275**, pp. 1102–1106 (1997).
- [4] F. Neubrech, T. Kolb, R. Lovrincic, G. Fahsold, A. Pucci, J. Aizpurua, T. W. Cornelius, M. E. Toimil-Molaes, R. Neumann, and S. Karim, “Resonances of individual metal nanowires in the infrared”, *Appl. Phys. Lett.* **89**, pp. 253104 (2006).
- [5] F. Neubrech, A. Pucci, T. W. Cornelius, S. Karim, A. García-Etxarri, and J. Aizpurua, “Resonant plasmonic and vibrational coupling in a tailored nanoantenna for infrared detection”, *Appl. Phys. Lett.* **101**, pp. 157403 (2008).
- [6] N. Liu, M. L. Tang, M. Hentschel, H. Giessen, and A. P. Alivisatos, “Nanoantenna-enhanced gas sensing in a single tailored nanofocus”, *Nature Mater.* **10**, pp. 631–636 (2011).
- [7] J. N. Anker, W. P. Hall, O. Lyandres, N. C. Shah, J. Zhao, and R. P. Van Duyne, “Biosensing with plasmonic nanosensors”, *Nature Mater.* **7**, pp. 442–453 (2008).
- [8] Z. Fan, M. Shelton, A. K. Singh, D. Senapati, S. A. Khan, and P. C. Ray, “Multifunctional plasmonic shell–magnetic core nanoparticles for targeted diagnostics, isolation, and photothermal destruction of tumor cells”, *ACS Nano* **6**, pp. 1065–1073 (2012).
- [9] D. A. Schultz, “Plasmon resonant particles for biological detection”, *Curr. Opin. Biotechnol.* **14**, pp. 13–22 (2003).

- [10] M. J. Crow, K. Seekell, J. H. Ostrander, and A. Wax, “Monitoring of receptor dimerization using plasmonic coupling of gold nanoparticles”, *ACS Nano* **5**, pp. 8532–8540 (2011).
- [11] Y. A. Akimov, W. S. Koh, and K. Ostrikov, “Enhancement of optical absorption in thin-film solar cells through the excitation of higher-order nanoparticle plasmon modes”, *Opt. Express* **17**, pp. 10195–10205 (2009).
- [12] K. R. Catchpole and A. Polman, “Plasmonic solar cells”, *Opt. Express* **16**, pp. 21793–21800 (2008).
- [13] H. A. Atwater and A. Polman, “Plasmonics for improved photovoltaic devices”, *Nature Mater.* **9**, pp. 205–213 (2010).
- [14] M. L. Brongersma, J. W. Hartman, and H. A. Atwater, “Electromagnetic energy transfer and switching in nanoparticle chain arrays below the diffraction limit”, *Phys. Rev. B* **62**, pp. 356–359 (2000).
- [15] S. A. Maier, P. G. Kik, H. A. Atwater, S. Meltzer, E. Harel, B. E. Koel, and A. A. G. Requicha, “Local detection of electromagnetic energy transport below the diffraction limit in metal nanoparticle plasmon waveguides”, *Nature Mater.* **2**, pp. 229–232 (2003).
- [16] C. E. Talley, J. B. Jackson, C. Oubre, N. K. Grady, C. W. Hollars, S. M. Lane, T. R. Huser, P. Nordlander, and N. J. Halas, “Surface-enhanced Raman scattering from individual Au nanoparticles and nanoparticle dimer substrates”, *Nano Lett.* **5**, pp. 1569–1574 (2005).
- [17] S. Li, M. L. Pedano, S.-H. Chang, C. A. Mirkin, and G. C. Schatz, “Gap structure effects on surface-enhanced Raman scattering intensities for gold gapped rods”, *Nano Lett.* **10**, pp. 1722–1727 (2010).
- [18] N. Féridj, J. Aubard, G. Lévi, J. R. Krenn, A. Hohenau, G. Schider, A. Leitner, and F. R. Aussenegg, “Optimized surface-enhanced Raman scattering on gold nanoparticle arrays”, *Appl. Phys. Lett.* **82**, pp. 3095–3097 (2003).
- [19] N. Féridj, J. Aubard, G. Lévi, J. R. Krenn, M. Salerno, G. Schider, B. Lamprecht, A. Leitner, and F. R. Aussenegg, “Controlling the optical response of regular arrays of gold particles for surface-enhanced Raman scattering”, *Phys. Rev. B* **65**, pp. 075419 (2002).

- [20] L. Billot, M. Lamy de la Chapelle, A. Grimault, A. Vial, D. Barchiesi, J. Bijeon, P. Adam, and P. Royer, “Surface enhanced Raman scattering on gold nanowire arrays: Evidence of strong multipolar surface plasmon resonance enhancement”, *Chem. Phys. Lett.* **422**, pp. 303–307 (2006).
- [21] G. Laurent, N. Félidj, J. Aubard, G. Lévi, J. Krenn, A. Hohenau, G. Schider, A. Leitner, and F. Aussenegg, “Evidence of multipolar excitations in surface enhanced Raman scattering”, *Phys. Rev. B* **71**, pp. 045430 (2005).
- [22] X. Li, W. Xu, J. Zhang, H. Jia, B. Yang, B. Zhao, B. Li, and Y. Ozaki, “Self-assembled metal colloid films: Two approaches for preparing new SERS active substrates”, *Langmuir* **20**, pp. 1298–1304 (2004).
- [23] L. Polavarapu and Q.-H. Xu, “Water-soluble conjugated polymer-induced self-assembly of gold nanoparticles and its application to SERS”, *Langmuir* **24**, pp. 10608–10611 (2008).
- [24] E. Hao, S. Li, R. C. Bailey, S. Zou, G. C. Schatz, and J. T. Hupp, “Optical properties of metal nanoshells”, *J. Phys. Chem. B* **108**, pp. 1224–1229 (2004).
- [25] B. N. Khlebtsov and N. G. Khlebtsov, “Multipole plasmons in metal nanorods: Scaling properties and dependence on particle size, shape, orientation, and dielectric environment”, *J. Phys. Chem. C* **111**, pp. 11516–11527 (2007).
- [26] E. R. Encina and E. A. Coronado, “Resonance conditions for multipole plasmon excitations in noble metal nanorods”, *J. Phys. Chem. C* **111**, pp. 16796–16801 (2007).
- [27] G. W. Bryant, F. J. García de Abajo, and J. Aizpurua, “Mapping the plasmon resonances of metallic nanoantennas”, *Nano Lett.* **8**, pp. 631–636 (2008).
- [28] M. Liu, T.-W. Lee, S. Gray, P. Guyot-Sionnest, and M. Pelton, “Excitation of dark plasmons in metal nanoparticles by a localized emitter”, *Phys. Rev. Lett.* **102**, pp. 107401 (2009).
- [29] E. Prodan, C. Radloff, N. J. Halas, and P. Nordlander, “A hybridization model for the plasmon response of complex nanostructures”, *Science* **302**, pp. 419–422 (2003).
- [30] J. Aizpurua, G. W. Bryant, L. J. Richter, F. J. García de Abajo, B. K. Kelley, and T. Mallouk, “Optical properties of coupled metallic nanorods for field-enhanced spectroscopy”, *Phys. Rev. B* **71**, pp. 235420 (2005).

- [31] B. Willingham, D. W. Brandl, and P. Nordlander, “Plasmon hybridization in nanorod dimers”, *Appl. Phys. B* **93**, pp. 209–216 (2008).
- [32] A. L. Koh, K. Bao, I. Khan, W. E. Smith, G. Kothleitner, P. Nordlander, S. A. Maier, and D. W. McComb, “Electron energy-loss spectroscopy of surface plasmons in silver nanoparticles and dimers: Influence of beam damage and mapping of dark modes”, *ACS Nano* **3**, pp. 3015–3022 (2009).
- [33] M. W. Chu, V. Myroshnychenko, C. H. Chen, J. P. Deng, C. Y. Mou, and F. J. García de Abajo, “Probing bright and dark surface-plasmon modes in individual and coupled noble metal nanoparticles using an electron beam”, *Nano Lett.* **9**, pp. 399–404 (2008).
- [34] C. P. Huang, X. G. Yin, L. B. Kong, and Y. Y. Zhu, “Interactions of nanorod particles in the strong coupling regime”, *Phys. Chem. C* **114**, pp. 21123–21131 (2010).
- [35] F. J. García de Abajo, “Relativistic energy loss and induced photon emission in the interaction of a dielectric sphere with an external electron beam”, *Phys. Rev. B* **59**, pp. 3095 (1999).
- [36] F. J. García de Abajo and M. Kociak, “Probing the photonic local density of states with electron energy loss spectroscopy”, *Phys. Rev. Lett.* **100**, pp. 106804 (2008).
- [37] N. Yamamoto, K. Araya, and F. J. García de Abajo, “Photon emission from silver particles induced by a high-energy electron beam”, *Phys. Rev. B* **64**, pp. 205419 (2001).
- [38] E. J. R. Vesseur, R. De Waele, M. Kuttge, and A. Polman, “Direct observation of plasmonic modes in Au nanowires using high-resolution cathodoluminescence spectroscopy”, *Nano Lett.* **7**, pp. 2843–2846 (2007).
- [39] R. Gómez-Medina, N. Yamamoto, M. Nakano, and F. J. García de Abajo, “Mapping plasmons in nanoantennas via cathodoluminescence”, *New J. Phys.* **10**, pp. 105009 (2008).
- [40] E. S. Barnard, T. Coenen, E. J. R. Vesseur, A. Polman, and M. L. Brongersma, “Imaging the hidden modes of ultrathin plasmonic strip antennas by cathodoluminescence”, *Nano Lett.* **11**, pp. 4265–4269 (2011).

- [41] J. Nelayah, M. Kociak, O. Stéphan, F. J. García de Abajo, M. Tencé, L. Henrard, D. Taverna, I. Pastoriza-Santos, L. M. Liz-Marzán, and C. Colliex, “Mapping surface plasmons on a single metallic nanoparticle”, *Nature Phys.* **3**, pp. 348–353 (2007).
- [42] M. Bosman, V. J. Keast, M. Watanabe, A. I. Maarroof, and M. B. Cortie, “Mapping surface plasmons at the nanometre scale with an electron beam”, *Nanotechnology* **18**, pp. 165505 (2007).
- [43] M. N’Gom, J. Ringnalda, J. F. Mansfield, A. Agarwal, N. Kotov, N. J. Zaluzec, and T. B. Norris, “Single particle plasmon spectroscopy of silver nanowires and gold nanorods.”, *Nano Lett.* **8**, pp. 3200–3204 (2008).
- [44] B. Schaffer, U. Hohenester, A. Trügler, and F. Hofer, “High-resolution surface plasmon imaging of gold nanoparticles by energy-filtered transmission electron microscopy”, *Phys. Rev. B* **79**, pp. 041401 (2009).
- [45] M. N’Gom, S. Li, G. Schatz, R. Erni, A. Agarwal, N. Kotov, and T. Norris, “Electron-beam mapping of plasmon resonances in electromagnetically interacting gold nanorods”, *Phys. Rev. B* **80**, pp. 113411 (2009).
- [46] D. Rossouw, M. Couillard, J. Vickery, E. Kumacheva, and G. A. Botton, “Multipolar plasmonic resonances in silver nanowire antennas imaged with a sub-nanometer electron probe”, *Nano Lett.* **11**, pp. 1499–1504 (2011).
- [47] O. Nicoletti, M. Wubs, N. A. Mortensen, W. Sigle, P. A. van Aken, and P. A. Midgley, “Surface plasmon modes of a single silver nanorod: An electron energy loss study”, *Opt. Express* **19**, pp. 15371 (2011).
- [48] I. Alber, W. Sigle, S. Müller, R. Neumann, O. Picht, M. Rauber, P. A. van Aken, and M. E. Toimil-Molaes, “Visualization of multipolar longitudinal and transversal surface plasmon modes in nanowire dimers”, *ACS Nano* **5**, pp. 9845–9853 (2011).
- [49] T. Blom, K. Welch, M. Strømme, E. Coronel, and K. Leifer, “Fabrication and characterization of highly reproducible, high resistance nanogaps made by focused ion beam milling”, *Nanotechnology* **18**, pp. 285301 (2007).
- [50] H. Duan, H. Hu, K. Kumar, Z. Shen, and J. K. W. Yang, “The direct and reliable patterning of plasmonic nanostructures with sub-10-nm gaps”, *ACS Nano* **5**, pp. 7593–7600 (2011).

- [51] K. D. Osberg, A. L. Schmucker, A. J. Senesi, and C. A. Mirkin, “One-dimensional nanorod arrays: Independent control of composition, length, and interparticle spacing with nanometer precision”, *Nano Lett.* **11**, pp. 820–824 (2011).
- [52] L. Qin, S. Park, L. Huang, and C. A. Mirkin, “On-wire lithography”, *Science* **309**, pp. 113–115 (2005).
- [53] M. E. Toimil-Molares, V. Buschmann, D. Dobrev, R. Neumann, R. Scholz, I. U. Schuchert, and J. Vetter, “Single-crystalline copper nanowires produced by electrochemical deposition in polymeric ion track membranes”, *Adv. Mater* **13**, pp. 62–65 (2001).
- [54] M. E. Toimil-Molares, J. Brötz, V. Buschmann, D. Dobrev, R. Neumann, R. Scholz, I. U. Schuchert, C. Trautmann, and J. Vetter, “Etched heavy ion tracks in polycarbonate as template for copper nanowires”, *Nucl. Inst. Meth. Phys. Res. B* **185**, pp. 192–197 (2001).
- [55] S. Karim, M. E. Toimil-Molares, F. Maurer, G. Mieke, W. Ensinger, J. Liu, T. W. Cornelius, and R. Neumann, “Synthesis of gold nanowires with controlled crystallographic characteristics”, *Appl. Phys. A* **84**, pp. 403–407 (2006).
- [56] S. Müller, C. Schötz, O. Picht, W. Sigle, P. Kopold, M. Rauber, I. Alber, R. Neumann, and M. E. Toimil-Molares, “Electrochemical synthesis of $\text{Bi}_{1-x}\text{Sb}_x$ nanowires with simultaneous control on size, composition, and surface roughness”, *Cryst. Growth Des.* **12**, pp. 615–621 (2012).
- [57] I. Enculescu, M. Sima, M. Enculescu, M. Enache, L. Ion, S. Antohe, and R. Neumann, “Deposition and properties of CdTe nanowires prepared by template replication”, *Phys. Status Solidi B* **244**, pp. 1607–1611 (2007).
- [58] O. Picht, S. Müller, I. Alber, M. Rauber, J. Lensch-Falk, D. L. Medlin, R. Neumann, and M. E. Toimil-Molares, “Tuning the geometrical and crystallographic characteristics of Bi_2Te_3 nanowires by electrodeposition in ion-track membranes”, *J. Phys. Chem. C* **116**, pp. 5367–5375 (2012).
- [59] D. Dobrev, J. Vetter, N. Angert, and R. Neumann, “Periodic reverse current electrodeposition of gold in an ultrasonic field using ion-track membranes as templates: Growth of gold single-crystals”, *Electrochim. Acta* **45**, pp. 3117 – 3125 (2000).

- [60] D. Dobrev, J. Vetter, R. Neumann, and N. Angert, “Conical etching and electrochemical metal replication of heavy-ion tracks in polymer foils”, *J. Vac. Sci. Technol. B* **19**, pp. 1385 (2001).
- [61] T. W. Cornelius, J. Brötz, N. Chtanko, D. Dobrev, G. Miehe, R. Neumann, and M. E. Toimil-Molares, “Controlled fabrication of poly- and single-crystalline bismuth nanowires”, *Nanotechnology* **16**, pp. 246 (2005).
- [62] J. Liu, J. L. Duan, M. E. Toimil-Molares, S. Karim, T. W. Cornelius, D. Dobrev, H. J. Yao, Y. M. Sun, M. D. Hou, D. Mo, Z. D. Wang, and R. Neumann, “Electrochemical fabrication of single-crystalline and polycrystalline Au nanowires: The influence of deposition parameters”, *Nanotechnology* **17**, pp. 1922 (2006).
- [63] J. Duan, J. Liu, D. Mo, H. Yao, K. Maaz, Y. Chen, Y. Sun, M. Hou, X. Qu, L. Zhang, and Y. Chen, “Controlled crystallinity and crystallographic orientation of Cu nanowires fabricated in ion-track templates”, *Nanotechnology* **21**, pp. 365605 (2010).
- [64] I. Alber, J. Krieg, C. Müller, M.E. Toimil-Molares, C. Trautmann, P. Serbun, A. Navitski, and G. Müller, “Freestanding copper nanocones for field emission by ion-track technology and electrodeposition”, *Techn. Digest of the 24th Int. Vacuum Nanoelectronics Conf. Wuppertal* **IEEE Cat. No. CFP11VAC-PRT**, pp. 9106–107 (2011).
- [65] C. Trautmann, S. Bouffard, and R. Spohr, “Etching threshold for ion tracks in polyimide”, *Nucl. Inst. Meth. B Phys. Res.* **116**, pp. 429–433 (1996).
- [66] Z. Siwy, P. Apel, D. Dobrev, R. Neumann, R. Spohr, C. Trautmann, and K. O. Voss, “Ion transport through asymmetric nanopores prepared by ion track etching”, *Nucl. Inst. Meth. Phys. Res. B* **208**, pp. 143–148 (2003).
- [67] P. Y. Apel, Y. E. Korchev, Z. Siwy, R. Spohr, and M. Yoshida, “Diode-like single-ion track membrane prepared by electro-stopping”, *Nucl. Instr. Meth. B* **184**, pp. 337–346 (2001).
- [68] N. Chtanko, M. E. Toimil-Molares, T. Cornelius, D. Dobrev, and R. Neumann, “Etched single-ion-track templates for single nanowire synthesis”, *J. Phys. Chem. B* **108**, pp. 9950–9954 (2004).
- [69] R. Spohr, “Status of ion track technology—prospects of single tracks”, *Radiat. Meas.* **40**, pp. 191–202 (2005).

- [70] B. E. Fischer and S. Metzger, “Single-ion micromechanics”, *MRS Bulletin - Materials Research Society* **25**, pp. 39–42 (2000).
- [71] J. F. Ziegler, M. D. Ziegler, and J. P. Biersack, “Srim—the stopping and range of ions in matter (2010)”, *Nucl. Instr. Meth. B* **268**, pp. 1818–1823 (2010).
- [72] M. C. Clochard, T. L. Wade, J. E. Wegrowe, and E. Balanzat, “Influence of asymmetric etching on ion track shapes in polycarbonate”, *Nucl. Instr. Meth. B* **265**, pp. 325–329 (2007).
- [73] H. Mukaibo, L.P. Horne, D. Park, and C. R. Martin, “Controlling the length of conical pores etched in ion-tracked poly(ethylene terephthalate) membranes”, *Small* **5**, pp. 2474–2479 (2009).
- [74] G. Pepy, P. Boesecke, A. Kuklin, E. Manceau, B. Schiedt, Z. Siwy, M. Toulemonde, and C. Trautmann, “Cylindrical nanochannels in ion-track polycarbonate membranes studied by small-angle X-ray scattering”, *J. Appl. Crystallogr.* **40**, pp. s388–s392 (2007).
- [75] H. B. Lück, “Mechanism of particle track etching in polymeric nuclear track detectors”, *Nucl. Instr. Meth. Phys. Res.* **202**, pp. 497–501 (1982).
- [76] R. L. Fleischer, P. B. Price, and R. M. Walker, *Nuclear tracks in solids: principles and applications.*, Univ of California Press (1975).
- [77] C. Ji, G. Oskam, Y. Ding, J. D. Erlebacher, A. J. Wagner, and P. C. Searson, “Deposition of $\text{Au}_x\text{Ag}_{1-x}/\text{Au}_y\text{Ag}_{1-y}$ multilayers and multisegment nanowires”, *J. Electrochem. Soc.* **150**, pp. C523–C528 (2003).
- [78] C. J. Dotzler, B. Ingham, B. N. Illy, K. Wallwork, M. P. Ryan, and M. F. Toney, “In situ observation of strain development and porosity evolution in nanoporous gold foils”, *Adv. Funct. Mater.* **21**, pp. 3938–3946 (2011).
- [79] T. Fujita, L. H. Qian, K. Inoke, J. Erlebacher, and M. W. Chen, “Three-dimensional morphology of nanoporous gold”, *Appl. Phys. Lett.* **92**, pp. 251902 (2008).
- [80] L. Y. Chen, J. S. Yu, T. Fujita, and M. W. Chen, “Nanoporous Copper with tunable nanoporosity for SERS applications”, *Adv. Funct. Mater.* **19**, pp. 1221–1226 (2009).

- [81] Z. Zhang, Y. Wang, Z. Qi, W. Zhang, J. Qin, and J. Frenzel, “Generalized fabrication of nanoporous metals (Au, Pd, Pt, Ag, and Cu) through chemical dealloying”, *J. Phys. Chem. C* **113**, pp. 12629–12636 (2009).
- [82] Z. Liu and P. C. Searson, “Single nanoporous gold nanowire sensors”, *J. Phys. Chem. B* **110**, pp. 4318–4322 (2006).
- [83] A. Wittstock, V. Zielasek, J. Biener, C. M. Friend, and M. Bäumer, “Nanoporous gold catalysts for selective gas-phase oxidative coupling of methanol at low temperature”, *Science* **327**, pp. 319–322 (2010).
- [84] L. H. Qian, X. Q. Yan, T. Fujita, A. Inoue, and M. W. Chen, “Surface enhanced Raman scattering of nanoporous gold: Smaller pore sizes stronger enhancements”, *Appl. Phys. Lett.* **90**, pp. 153120 (2007).
- [85] H. M. Bok, K. L. Shuford, S. Kim, S. K. Kim, and S. Park, “Multiple surface plasmon modes for a colloidal solution of nanoporous gold nanorods and their comparison to smooth gold nanorods”, *Nano Lett.* **8**, pp. 2265–2270 (2008).
- [86] J. Erlebacher, M. J. Aziz, A. Karma, N. Dimitrov, and K. Sieradzki, “Evolution of nanoporosity in dealloying”, *Nature* **410**, pp. 450–453 (2001).
- [87] J. Erlebacher and R. Seshadri, “Hard materials with tunable porosity”, *MRS Bulletin - Materials Research Society* **34**, pp. 561–568 (2009).
- [88] C. Ji and P. C. Searson, “Fabrication of nanoporous gold nanowires”, *Appl. Phys. Lett.* **81**, pp. 4437 (2002).
- [89] C. Ji and P. C. Searson, “Synthesis and characterization of nanoporous gold nanowires”, *J. Phys. Chem. B* **3**, pp. 4494–4499 (2003).
- [90] G. D. Sulka, A. Brzózka, and L. Liu, “Fabrication of diameter-modulated and ultrathin porous nanowires in anodic aluminum oxide templates”, *Electrochim. Acta* **56**, pp. 4972–4979 (2011).
- [91] R. Laocharoensuk, S. Sattayasamitsathit, J. Burdick, P. Kanatharana, P. Thavarungkul, and J. Wang, “Shape-tailored porous gold nanowires: From nano barbells to nano step-cones”, *ACS Nano* **1**, pp. 403–408 (2007).
- [92] M. H. Devoret and R. J. Schoelkopf, “Amplifying quantum signals with the single-electron transistor”, *Nature* **406**, pp. 1039–1046 (2000).

- [93] H. Xu, J. Aizpurua, M. Kall, and P. Apell, “Electromagnetic contributions to single-molecule sensitivity in surface-enhanced Raman scattering”, *Phys. Rev. E* **62**, pp. 4318–4324 (2000).
- [94] L. Qin, S. Zou, C. Xue, A. Atkinson, G. C. Schatz, and C. A. Mirkin, “Designing, fabricating, and imaging Raman hot spots.”, *Proc. Nat. Acad. Sci. USA* **103**, pp. 13300–13303 (2006).
- [95] N. V. Hoang, S. Kumar, and G. H. Kim, “Growth of segmented gold nanorods with nanogaps by the electrochemical wet etching technique for single-electron transistor applications.”, *Nanotechnology* **20**, pp. 125607 (2009).
- [96] X. Gu, L. Xu, F. Tian, and Y. Ding, “Au – Ag alloy nanoporous nanotubes”, *Nano Res.* **2**, pp. 386–393 (2009).
- [97] N. L. Netzer, C. Qiu, Y. Zhang, C. Lin, L. Zhang, H. Fong, and C. Jiang, “Gold-silver bimetallic porous nanowires for surface-enhanced Raman scattering.”, *Chem. Comm.* **47**, pp. 9606–9608 (2011).
- [98] M. E. Toimil-Molaes, A. G. Balogh, T. W. Cornelius, R. Neumann, and C. Trautmann, “Fragmentation of nanowires driven by Rayleigh instability”, *Appl. Phys. Lett.* **85**, pp. 5337 (2004).
- [99] S. Karim, M. E. Toimil-Molaes, A. G. Balogh, W. Ensinger, T. W. Cornelius, E. U. Khan, and R. Neumann, “Morphological evolution of au nanowires controlled by Rayleigh instability”, *Nanotechnology* **17**, pp. 5954–5959 (2006).
- [100] J. D. Jackson, *Classical electrodynamics*, John Wiley and sons (1965).
- [101] L. Novotny and B. Hecht, *Principles of nano-optics*, Cambridge Univ Press (2006).
- [102] P. B. Johnson and R. W. Christy, “Optical constants of the noble metals”, *Phys. Rev. B* **6**, pp. 4370 (1972).
- [103] P. Pyykkö and J. P. Desclaux, “Relativity and the periodic system of elements”, *Acc. Chem. Res.* **12**, pp. 276–281 (1979).
- [104] J. A. Scholl, A. L. Koh, and J. A. Dionne, “Quantum plasmon resonances of individual metallic nanoparticles”, *Nature* **483**, pp. 421–427 (2012).
- [105] F. J. García de Abajo, “Microscopy: Plasmons go quantum”, *Nature* **483**, pp. 417–418 (2012).

- [106] G. Mie, “Beiträge zur Optik trüber Medien, speziell kolloidaler Metallösungen”, *Ann. Phys.* **330**, pp. 377–445 (1908).
- [107] R. Gans, “Über die Form ultramikroskopischer Silberpartikel”, *Ann. Phys.* **352**, pp. 270–284 (1915).
- [108] A. Pucci, F. Neubrech, J. Aizpurua, T. Cornelius, and M. Lamy de la Chapelle, “Electromagnetic nanowire resonances for field-enhanced spectroscopy”, *Book Chapter in One-Dimensional Nanostructures*, pp. 175–215 (2008).
- [109] V. Giannini, A. I. Fernández-Domínguez, S. C. Heck, and S. A. Maier, “Plasmonic nanoantennas: Fundamentals and their use in controlling the radiative properties of nanoemitters”, *Chem. Rev.* **111**, pp. 3888–912 (2011).
- [110] P. Biagioni, J. S. Huang, and B. Hecht, “Nanoantennas for visible and infrared radiation”, *Rep. Prog. Phys.* **75**, pp. 024402 (2012).
- [111] F. J. García de Abajo and A. Howie, “Relativistic electron energy loss and electron-induced photon emission in inhomogeneous dielectrics”, *Phys. Rev. Lett.* **80**, pp. 5180–5183 (1998).
- [112] F. J. García de Abajo and A. Howie, “Retarded field calculation of electron energy loss in inhomogeneous dielectrics”, *Phys. Rev. B* **65**, pp. 115418 (2002).
- [113] J. Zuloaga and P. Nordlander, “On the energy shift between near-field and far-field peak intensities in localized plasmon systems”, *Nano Lett.* **11**, pp. 1280–1283 (2011).
- [114] J. Dormüller, R. Vogelgesang, R. T. Weitz, C. Rockstuhl, C. Etrich, T. Pertsch, F. Lederer, and K. Kern, “Fabry-Perot resonances in one-dimensional plasmonic nanostructures”, *Nano Lett.* **9**, pp. 2372–2377 (2009).
- [115] J. Dorfmueller, R. Vogelgesang, W. Khunsin, C. Rockstuhl, C. Etrich, and K. Kern, “Plasmonic nanowire antennas: Experiment, simulation, and theory”, *Nano Lett.* **10**, pp. 3596–603 (2010).
- [116] P. Nordlander and E. Prodan, “Plasmon hybridization in nanoparticles near metallic surfaces”, *Nano Lett.* **4**, pp. 2209–2213 (2004).
- [117] P. Nordlander, C. Oubre, E. Prodan, K. Li, and M. I. Stockman, “Plasmon hybridization in nanoparticle dimers”, *Nano Lett.* **4**, pp. 899–903 (2004).

- [118] J. Zuloaga, E. Prodan, and P. Nordlander, “Quantum description of the plasmon resonances of a nanoparticle dimer”, *Nano Lett.* **9**, pp. 887–891 (2009).
- [119] J. B. Lassiter, J. Aizpurua, L. I. Hernandez, D. W. Brandl, I. Romero, S. Lal, J. H. Hafner, P. Nordlander, and N. J. Halas, “Close encounters between two nanoshells”, *Nano Lett.* **8**, pp. 1212–1218 (2008).
- [120] I. Romero, J. Aizpurua, G. W. Bryant, and F. J. García de Abajo, “Plasmons in nearly touching metallic nanoparticles: singular response in the limit of touching dimers”, *Opt. Express* **14**, pp. 9988–9999 (2006).
- [121] D. Pines and D. Bohm, “A collective description of electron interactions: II. Collective vs individual particle aspects of the interactions”, *Phys. Rev.* **85**, pp. 338 (1952).
- [122] R. H. Ritchie, “Plasma losses by fast electrons in thin films”, *Phys. Rev.* **106**, pp. 874 (1957).
- [123] W. Sigle, “Analytical transmission electron microscopy”, *Ann. Rev. Mater. Res.* **35**, pp. 239–314 (2005).
- [124] C. T. Koch, W. Sigle, R. Höschel, M. Rühle, E. Essers, G. Benner, and M. Matijevic, “SESAM: Exploring the frontiers of electron microscopy”, *Microsc. Microanal.* **12**, pp. 506–514 (2006).
- [125] M. A. Ordal, L. L. Long, R. J. Bell, Alexander R. W., and M. R. Query, “Optical properties of the metals Al, Co, Cu, Au, Fe, Pb, Ni, Pd, Pt, Ag, Ti, and W in the infrared and far infrared”, *Appl. Opt.* **22**, pp. 1099–1119 (1983).
- [126] S. Link, M. B. Mohamed, and M. A. El-Sayed, “Simulation of the optical absorption spectra of gold nanorods as a function of their aspect ratio and the effect of the medium dielectric constant”, *J. Phys. Chem. B* **103**, pp. 3073–3077 (1999).
- [127] E. S. Kooij and B. Poelsema, “Shape and size effects in the optical properties of metallic nanorods”, *Phys. Chem. Chem. Phys.* **8**, pp. 3349–3357 (2006).
- [128] A. Brioude, X. C. Jiang, and M. P. Pileni, “Optical properties of gold nanorods: DDA simulations supported by experiments”, *J. Phys. Chem. B* **109**, pp. 13138–13142 (2005).

- [129] K. S. Lee and M. A. El-Sayed, “Dependence of the enhanced optical scattering efficiency relative to that of absorption for gold metal nanorods on aspect ratio, size, end-cap shape, and medium refractive index”, *J. Phys. Chem. B* **109**, pp. 20331–20338 (2005).
- [130] A. Trügler, J.-C. Tinguely, J. Krenn, A. Hohenau, and U. Hohenester, “Influence of surface roughness on the optical properties of plasmonic nanoparticles”, *Phys. Rev. B* **83**, pp. 1–4 (2011).
- [131] H. Wang, G. P. Goodrich, F. Tam, C. Oubre, P. Nordlander, and N. J. Halas, “Controlled texturing modifies the surface topography and plasmonic properties of Au nanoshells”, *J. Phys. Chem. B* **109**, pp. 11083–11087 (2005).
- [132] J. Rodríguez-Fernández, A. M. Funston, J. Pérez-Juste, R. A. Álvarez-Puebla, L. M. Liz-Marzán, and P. Mulvaney, “The effect of surface roughness on the plasmonic response of individual sub-micron gold spheres”, *Phys. Chem. Chem. Phys.* **11**, pp. 5909–5914 (2009).
- [133] H. Wang, K. Fu, R.a. Drezek, and N.J. Halas, “Light scattering from spherical plasmonic nanoantennas: Effects of nanoscale roughness”, *Appl. Phys. B* **84**, pp. 191–195 (2006).
- [134] L. Novotny, “Effective wavelength scaling for optical antennas”, *Phys. Rev. Lett.* **98**, pp. 266802 (2007).
- [135] S. Link, Z. L. Wang, and M. A. El-Sayed, “Alloy formation of gold-silver nanoparticles and the dependence of the plasmon absorption on their composition”, *J. Phys. Chem. B* **103**, pp. 3529–3533 (1999).
- [136] J. Sinzig, U. Radtke, M. Quinten, and U. Kreibig, “Binary clusters: Homogeneous alloys and nucleus-shell structures”, *Z. Phys. D* **26**, pp. 242–245 (1993).
- [137] A. Artar, A. A. Yanik, and H. Altug, “Directional double Fano resonances in plasmonic hetero-oligomers”, *Nano Lett.* **11**, pp. 3694–3700 (2011).
- [138] A. I. Denisyuk, G. Adamo, K. F. MacDonald, J. Edgar, M. D. Arnold, V. Myroshnychenko, M. J. Ford, F. J. García de Abajo, and N. I. Zheludev, “Transmitting hertzian optical nanoantenna with free-electron feed”, *Nano Lett* **10**, pp. 3250–3252 (2010).

- [139] N. Large, M. Abb, J. Aizpurua, and O. L. Muskens, “Photoconductively loaded plasmonic nanoantenna as building block for ultracompact optical switches”, *Nano Lett.* **10**, pp. 1741–1746 (2010).
- [140] E. R. Encina and E. A. Coronado, “Plasmon coupling in silver nanosphere pairs”, *J. Phys. Chem. C* **114**, pp. 3918–3923 (2010).
- [141] L. S. Slaughter, Y. Wu, B. A. Willingham, P. Nordlander, and S. Link, “Effects of symmetry breaking and conductive contact on the plasmon coupling in gold nanorod dimers”, *ACS Nano* **4**, pp. 4657–4666 (2010).
- [142] O. Pérez-González, N. Zabala, A. G. Borisov, N. J. Halas, P. Nordlander, and J. Aizpurua, “Optical spectroscopy of conductive junctions in plasmonic cavities”, *Nano Lett.* **10**, pp. 3090–3095 (2010).
- [143] O. Pérez-González, N. Zabala, and J. Aizpurua, “Optical characterization of charge transfer and bonding dimer plasmons in linked interparticle gaps”, *New J. Phys.* **13**, pp. 083013 (2011).
- [144] M. Schnell, A. Garcia-Etxarri, A. J. Huber, K. Crozier, J. Aizpurua, and R. Hillenbrand, “Controlling the near-field oscillations of loaded plasmonic nanoantennas”, *Nat. Photonics* **3**, pp. 287–291 (2009).
- [145] F. Hao, Y. Sonnefraud, P. V. Dorpe, S. A. Maier, N. J. Halas, and P. Nordlander, “Symmetry breaking in plasmonic nanocavities: subradiant LSPR sensing and a tunable Fano resonance”, *Nano Lett.* **8**, pp. 3983–3988 (2008).
- [146] B. Gallinet and O. J. F. Martin, “Influence of electromagnetic interactions on the line shape of plasmonic Fano resonances”, *ACS Nano* **5**, pp. 8999–9008 (2011).
- [147] P. Alonso-Gonzalez, M. Schnell, P. Sarriugarte, H. Sobhani, C. Wu, N. Arju, A. Khanikaev, F. Golmar, P. Albella, L. Arzubia, F. Casanova, L. E. Hueso, P. Nordlander, G. Shvets, and R. Hillenbrand, “Real-space mapping of Fano interference in plasmonic metamolecules”, *Nano Lett.* **11**, pp. 3922–3926 (2011).
- [148] A. J. Haes, L. Chang, W. L. Klein, and R. P. Van Duyne, “Detection of a biomarker for alzheimer’s disease from synthetic and clinical samples using a nanoscale optical biosensor”, *J. Am. Chem. Soc.* **127**, pp. 2264–2271 (2005).

Abbreviations

AB _{<i>l</i>} -mode	antibonding mode of multipole order <i>l</i>
Ag	silver
Au	gold
B _{<i>l</i>} -mode	bonding mode of multipole order <i>l</i>
BEM	boundary element method
BS mode	backscattering mode
Cu	copper
CT	charge transfer
DDA	discrete dipole approximation
EELS	electron energy loss spectroscopy
EDX	energy dispersive x-ray spectroscopy
FESEM	field emission scanning electron microscope
HRSEM	high-resolution scanning electron microscope
LaB ₆	lanthanum hexaboride
PET	polyethyleneterephthalat
SE mode	secondary electron mode
SEM	scanning electron microscope
SERS	surface enhanced Raman spectroscopy
SEIRS	surface enhanced infrared spectroscopy
Si	silicon
Si ₃ N ₄	silicon nitride
SNOM	near-field scanning optical microscopy
SP	surface plasmon
STEM	scanning transmission electron microscopy
TEM	transmission electron microscope

Danksagung

An dieser Stelle möchte ich mich ganz herzlich bei allen bedanken, die einen großen Anteil zum Gelingen dieser Arbeit beigetragen haben. Insbesondere gilt mein Dank

- Prof. Dr. R. Neumann für die Möglichkeit zur Promotion auf dem spannenden Gebiet der Nanotechnologie, das stetige Interesse am Fortgang meiner Arbeit, die gute Betreuung und die Möglichkeit zu vielen Konferenzteilnahmen.
- Prof. Dr. A. Pucci für die Übernahme des Zweitgutachtes, sowie für die Einladung zu Seminarvorträgen in ihrer Arbeitsgruppe am Kirchhoff-Institut für Physik in Heidelberg.
- Dr. M. E. Toimil Molares für die Hilfe und Unterstützung während meiner gesamten Promotionszeit, das Korrigieren dieser Arbeit sowie die sehr hilfreichen wissenschaftlichen Diskussion; außerdem für die sehr angenehme Atmosphäre bei gemeinsamen Dienstreisen und Experimenten.
- Prof. Dr. C. Trautmann für die Einführung in die Ionen-Bestrahlungsexperimente, sowie die vielen wissenschaftlichen Ratschläge während meiner Promotionszeit.
- Dr. W. Sigle und Prof. Dr. P. A. van Aken vom MPI für Intelligente Systems Stuttgart für die sehr spannenden EELS Messungen an den Nanodrähten, die einen großen Teil dieser Arbeit ausmachen, sowie für die interessanten wissenschaftlichen Diskussionen zu den Ergebnissen der EELS Messungen und die Möglichkeit zu mehreren Aufenthalten am MPI zur Auswertung der Daten.
- Dr. F. Neubrech für die interessanten und hilfreichen Diskussionen zu Thema der Oberflächenplasmonen.
- Dr. M. Rauber, Dr. S. Müller, Dr. O. Picht für die Einführung in die Herstellung der Nanodrähte und in die Rasterelektronenmikroskopie und die gute Zusammenarbeit.
- Dr. F. Demming-Janssen von der Firma CST Microwave Studio für die hilfreichen Tipps zu den Finite Element Simulationen.
- B. Merk, Dr. B. Schuster, Dr. K.O. Voss und T. Seidl für die sehr freundschaftlich gemeinsam verbrachte Zeit und die Aufmunterung während Probenvorbereitungen und Experimenten.

- der gesamten Abteilung Materialforschung der GSI für die angenehme Arbeitsatmosphäre und die gute Zusammenarbeit.

Ganz besonders möchte ich mich bei meinen Eltern, Anne und vor allem Sebastian für die permanente Unterstützung, die Ermutigung und ihr Verständnis bedanken.